DYNAMICS AND TOPOLOGY OF NONLINEAR AND APERIODIC METASTRUCTURES

A Dissertation
Presented to
The Academic Faculty

By

Yiwei Xia

In Partial Fulfillment
of the Requirements for the Degree
Doctor of Philosophy in the
School of Georgia W. Woodruff School of Mechanical Engineering

Georgia Institute of Technology

December 2020

DYNAMICS AND TOPOLOGY OF NONLINEAR AND APERIODIC METASTRUCTURES

Approved by:

Dr. Alper Erturk, Committee Chair
School of Mechanical Engineering
Georgia Institute of Technology

Dr. Alper Erturk, Advisor
School of Mechanical Engineering
Georgia Institute of Technology

Dr. Massimo Ruzzene, Co-Advisor
School of Mechanical Engineering
University of Colorado, Boulder

Dr. Julien Meaud
School of Mechanical Engineering
Georgia Institute of Technology

Dr. Martin Maldovan
School of Chemical and Biomolecular Engineering
School of Physics
Georgia Institute of Technology

Dr. Andrea Alù
Advanced Science Research Center
City University of New York

Date Approved: November 2, 2020

ACKNOWLEDGEMENTS

First and foremost, my greatest gratitude goes to my advisors, Dr. Massimo Ruzzene and Dr. Alper Erturk. They encouraged and challenged me to explore various stimulating research topics and to strive for high-quality work. Furthermore, they provided me with numerous opportunities to present my work in conferences and workshops. Without their wholehearted support and advise, this work would not have been possible. Additional gratitude goes to my committee members, Dr. Julien Meaud, Dr. Martin Maldovan and Dr. Andrea Alù. I really appreciate the investment of their time for reviewing my work, providing their expert views and guidance.

I would also like to thank all the colleagues and friends, who have been a constant source of support and encouragement during my graduate school years.

Last but not least, I would like to thank my parents for their unconditional love and support over these years.

This work was supported by the Air Force Office of Scientific Research through grant FA9550-15-1-0397, National Science Foundation through Emerging Frontiers in Research and Innovation (EFRI) program grant No. 1741685 and Army Research Office through grant W911NF-18-1-0036.

TABLE OF CONTENTS

LIST OF TABLES

LIST OF FIGURES

SUMMARY

Metamaterials and metastructures (i.e. metamaterial-based finite structures with specified boundary conditions) enable various properties that are not found in ordinary materials and structures. For example, locally resonant (LR) elastic/acoustic metastructures exhibit bandgaps at wavelengths much longer than the lattice size, enabling low-frequency vibration/noise attenuation. Most investigations in this domain have considered nominally identical linear resonators that are periodically attached to the structure. In these cases, the LR bandgap depends on the natural frequency of the resonators, and the bandwidth is limited by the added inertia and the electromechanical coupling in mechanical and electromechanical metastructures, respectively. In this work, the LR metastructure concept is expanded in two directions: one is including nonlinearity, specifically considering bistable attachments; the other one is including aperiodicity, namely by considering the resonators in quasiperiodic arrangements. First, numerical and experimental results show the amplitude-dependent enhancement of the attenuation bandwidth in LR metastructures via bistable attachments, and demonstrate that the vibration attenuation band offered by nonlinear interwell oscillations is substantially wider than the linear LR bandgap. Next, the dynamic behavior and topological properties of LR mechanical metastructures hosting quasiperiodic distributions of resonators are investigated. It is shown both numerically and experimentally that quasiperiodic placement of resonators introduces additional bandgaps that are topologically non-trivial and host protected edge-localized modes. The findings suggest the application of quasiperiodic resonators as an effective way to achieve attenuation over multiple frequency bands and to control vibration localization at desired frequencies. In analogy with mechanical LR metastructures with quasiperiodic arrangements of resonators, electromechanical LR metastructures with quasiperiodic resonant shunt circuits are explored. Topologically non-trivial bandgaps and associated edge-localized modes are observed experimentally in an electromechanical metastructure by leveraging digitally pro-

grammable synthetic impedance circuits. Additional studies investigate the transitions of localized mode through slow phase modulation, with experimental observation of temporal topological pumping in an electromechanical structure under stiffness modulation via variable negative capacitance circuits.

CHAPTER 1
INTRODUCTION

1.1 Overview

Vibration is undesirable in many fields, primarily engineered systems. Key components or sensitive equipment often must be isolated from excessive vibration. Traditional vibration control techniques, such as using dynamic vibration absorbers and tuned mass dampers, yield a trade-off between attenuation and bandwidth. The concept of phononic crystals [1], synthetic materials made of periodic variation of material properties first proposed nearly three decades ago, has the potential to address this shortcoming. One of the most desirable characteristics is the possibility of having phononic bandgaps due to Bragg scattering [2]. However, bandgap pertaining to Bragg scattering occurs at the wavelengths of the order of the lattice size, which would require extremely large systems for low-frequency vibration attenuation.

1.2 Locally Resonant Metamaterials and Metastructures

To overcome the limitations of phononic crystals and to design feasible structures for real-world applications, locally resonant (LR) metamaterials and resulting finite LR metastructures with specified boundary conditions have been extensively studied over the past decade since the seminal work by Liu et al. [3]. Metamaterials made from LR unit cells exhibit frequency bandgaps of wave attenuation that are similar to Bragg scattering-based bandgaps in phononic crystals, but are fundamentally different in terms of their physical principles. The out-of-phase motion of the local resonators with respect to the main structure leads to the attenuation, typically occurring at the resonant frequency of the attachments. Therefore, LR bandgaps can happen at wavelengths much larger than the lattice size. This provides

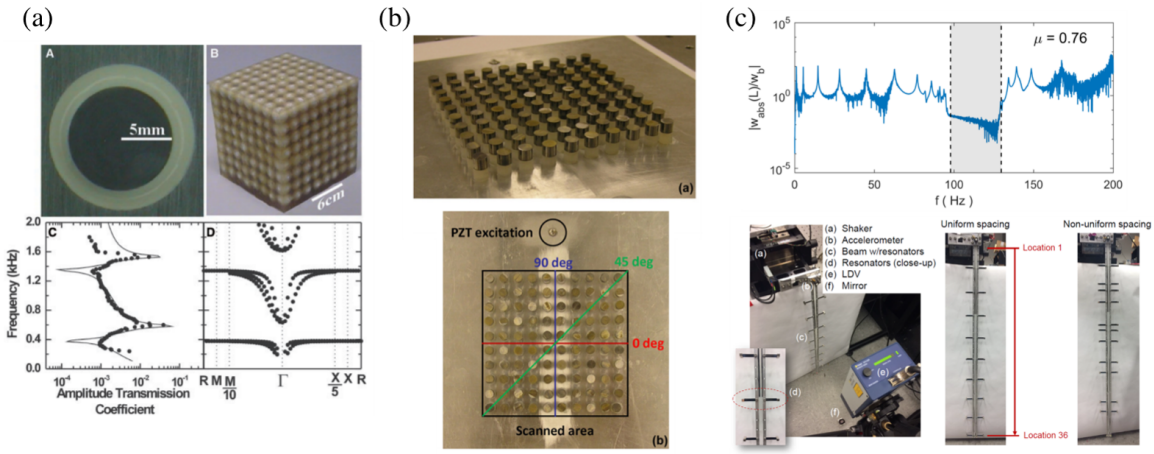

Figure 1.1: Examples of mechanical locally resonant linear metamaterials and metastructures. (a) Sonic crystals with unit consisting of a solid core material and a coating of elastically soft material [3]. (b) Plate-type acoustic metamaterials consisting of a periodic arrangement of composite stubs (tungsten/silicone rubber) deposited on a thin aluminium plate [4]. (c) Locally resonant cantilever beam under base excitation [5].

an opportunity to use LR elastic/acoustic metastructures for low-frequency vibration/noise attenuation and wave filtering, among other applications [3, 6, 7, 8, 4, 9, 10].

Most investigations have considered nominally identical linear local resonators that are periodically attached to the structure. In these cases, the LR bandgap size, i.e., the attenuation bandwidth, is limited by the added mass [10], which is typically to be minimized in most applications spanning from aerospace structures to those requiring compact designs due to space and other limitations. The attenuation frequency range is given by:

$$\omega_t < \omega < \omega_t \sqrt{1+\mu}, \tag{1.1}$$

where ω_t is the natural frequency of the resonator and μ is the ratio of the total mass of the resonators to the total mass of the plain main structure. It is worth mentioning that, in a discrete configuration, such as a spring-mass system hosting internal spring-mass resonators investigated in [11], the lower bound of the LR bandgap also depends on the stiffness ratio between the spring connecting the resonator mass to the main mass and the spring connecting main masses with each other. The aforementioned efforts on locally

resonant metamaterials and metastructures are purely mechanical configurations.

In analogy with mechanical locally resonant metamaterials, electromechanical metamaterials using many piezoelectric elements with resonant shunt circuits have been studied [12, 13, 14, 15, 16, 17, 18]. The electromechanical locally resonant bandgap is shown to be limited by the system level electromechanical coupling [18], with the attenuation frequency range given by:

$$\frac{\omega_t}{\sqrt{1+\alpha}} < \omega < \omega_t, \tag{1.2}$$

where α is the dimensionless system-level electromechanical coupling parameter that measures how strongly coupled the electrical and the mechanical domains are. Although electromechanical metamaterials are more complex than their mechanical counterparts, the flexibility in piezoelectric shunt circuits gives significant advantages for the system to be tunable or programmable. For instance, Sugino et al. [19] recently employed synthetic impedance circuit based locally resonant metastructures with unprecedented bandgap tuning capabilities.

1.3 Nonlinear Dynamics for Bandwidth Enhancement

As mentioned in the previous section, mechanical LR metamaterials and metastructures using linear oscillators have been widely studied and the bandgap size is limited by the added inertia. Compared to linear configurations, nonlinearities provide rich dynamics such as sub- and super-harmonic resonances and in some cases chaotic behavior. As leveraged in the vibration energy harvesting field, properly designed nonlinear oscillators offer various advantages, among which substantially enhanced frequency bandwidth is of primary interest. For instance, as summarized in [20], both monostable and bistable nonlinear oscillators have been investigated to enable wideband energy harvesters over the past decade. Especially, bistable configurations provide a plethora of wideband dynamic behavior through periodic intrawell and interwell oscillations, and chaotic interwell vibrations depending on

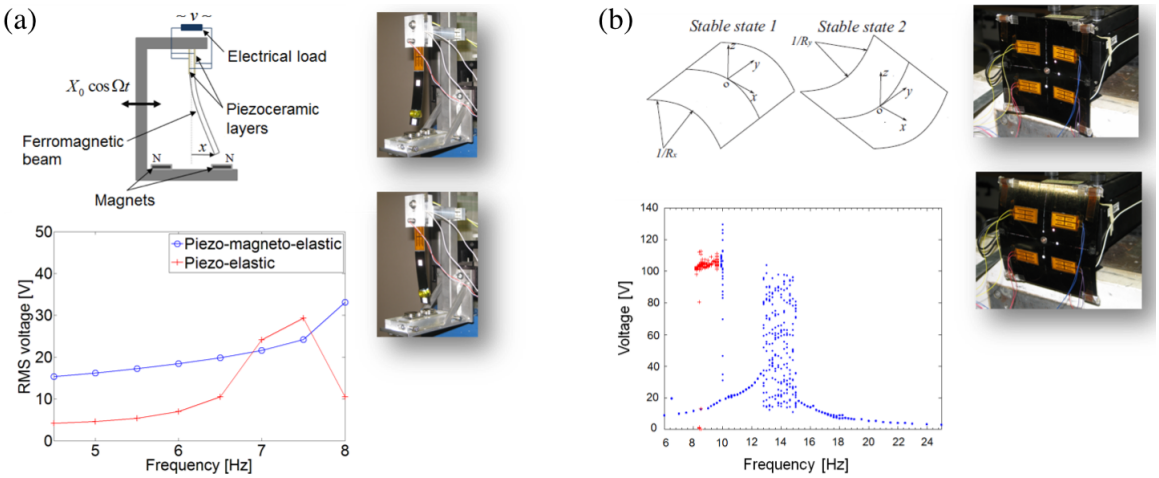

Figure 1.2: Examples of utilizing bistability for bandwidth enhancement. (a) A piezomagnetoelastic structure with bistability due to magnetic attraction of external magnets to the ferromagnetic cantilever [21]. (b) A piezoelectric buckled asymmetric plate [25].

the input amplitudes [21, 22, 23, 24]. These studies shed light on the design of individual bistable oscillators to target a specific frequency bandwidth, not only for harvesting energy but also for other applications. In terms of nonlinear vibration attenuation, many efforts have focused on the concept of nonlinear energy sink (NES) [26, 27, 28, 29, 30, 31], evolving from relatively simple systems of one linear oscillator with one NES attached to a continuous structure with one NES attached. In addition, some researchers utilized bistable oscillators; however, they mainly explored low degree-of-freedom (DOF) systems, typically in the form of a linear oscillator coupled to a bistable attachment [32, 33, 34, 35]. These studies, on both the transient dissipative dynamics under impulse excitation and the steady-state responses under harmonic excitation, unveil the potential of bistable attachments for wideband attenuation behavior.

On the other hand, in metamaterial/metastructure settings, limited work has focused on nonlinear resonating configurations [36]. For example, Lazarov et al. [37] considered Duffing type cubic hardening nonlinear resonators; Banerjee et al. [38] numerically investigated the effects of cubic hardening nonlinearity in a series of spring mass-in-mass system; Casalotti et al. [39] explored the nonlinear frequency response of a metamaterial beam with nonlinear absorbers and demonstrated enhanced vibration suppression performance.

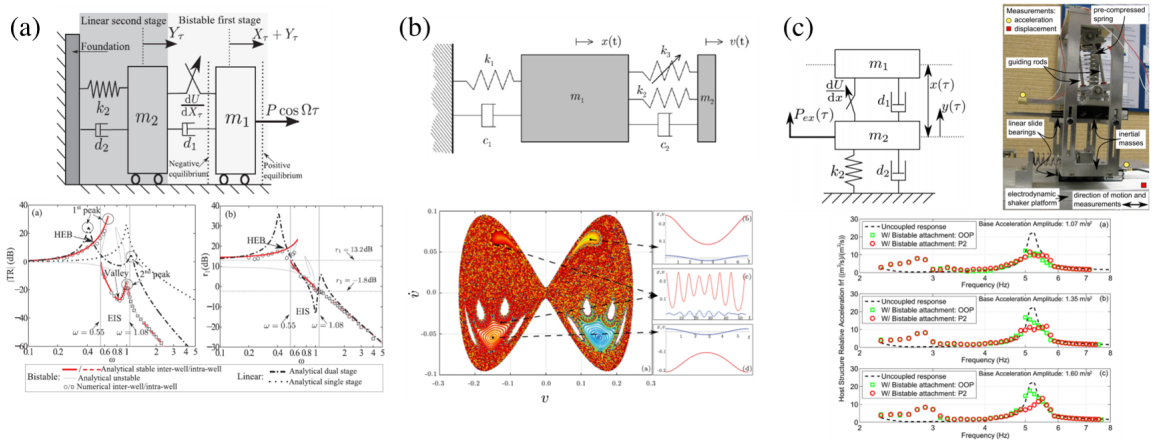

Figure 1.3: Examples of investigations on strongly nonlinear (bistable) absorbers and energy sinks. (a) A bistable dual-stage vibration isolator under harmonic excitation [32]. (b) A linear oscillator coupled to a bistable light attachment under impulse excitation [34]. (c) Vibration control using a bistable snap-through attachment [33].

It is also worth mentioning that, in a parallel body of work, interesting phenomena such as solitary wave propagation and unidirectional wave propagation have been demonstrated in bistable lattices [40, 41, 42].

1.4 Quasiperiodic Metamaterials and Metastructures

Attempts at extending the resonant gap through non-uniform resonators, both in terms of their natural frequency and their spacing, can be found in [7, 43, 44], among others. Parallel to these efforts, there is considerable interest on the conditions that govern the onset of localization [45, 46, 47]. Vibration localization can be both beneficial in terms of isolating components and limiting exposure, but can also be the source of catastrophic failures [48], and therefore is of great relevance to the engineering community.

Inspired by the discovery of topologically non-trivial phases in electronic [49] and photonic [50] systems, various classes of topological phenomena such as quantum Hall and quantum spin Hall effects have been studied and realized in acoustic and mechanical systems [51]. These works exploit defect-immune modes localized at edges or interfaces for robust acoustic/elastic waveguiding. Recently, topological phases have also been explored

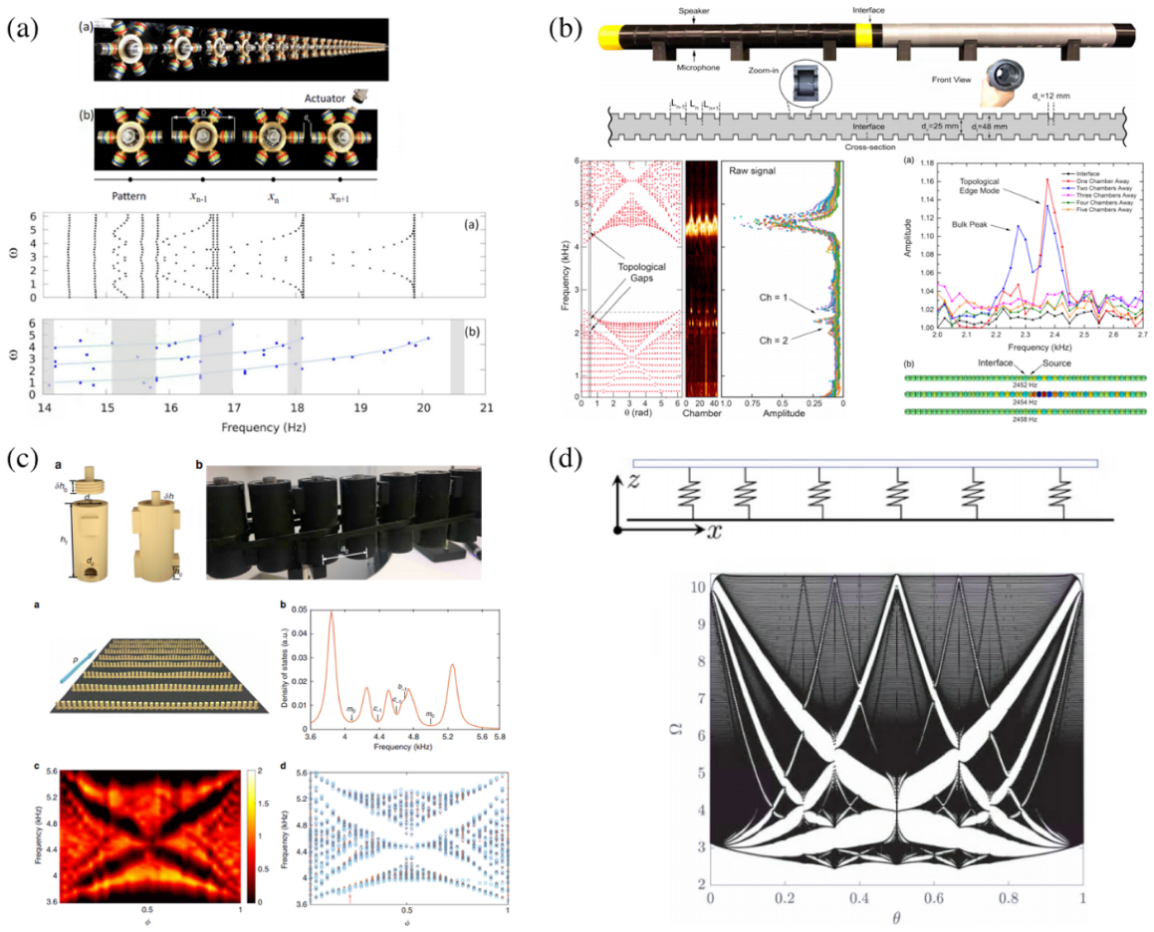

Figure 1.4: Quasiperiodic systems in mechanics and acoustics. (a) Localized modes at the boundary of finite arrays of quasiperiodic discrete mechanical resonators [60]. (b) Topological boundary and interface modes in quasiperiodic acoustic waveguides [61]. (c) Hofstadter spectrum observed in reconfigurable quasiperiodic acoustic crystals [62]. (d) Hofstadter spectrum shown in continuous beams supported by a quasiperiodic array of ground springs [63].

in lower physical dimensional systems by exploiting virtual dimensions in relevant parameter spaces [52, 53, 54, 55]. In particular, quasi-crystalline or quasiperiodic structures have been linked to topological insulators [56, 57, 58]. Quasiperiodicity defines a broad class of geometrical patterns, of which periodic assemblies are particular cases. Thus, the study of quasiperiodic (QP) arrangements of inclusions can extend the range of capabilities of periodic metamaterials and metastructures [59].

A recent line of work considers a framework to investigate QP systems based on the evaluation of their spectral properties, the evaluation of the density of states, and the es-

timation of topological invariants that may characterize non-trivial gaps and the onset of associated edge states [60, 61, 62, 63]. For example, recent work in mechanics [60] has demonstrated that topological boundary modes can emerge solely from the patterning of a metamaterial, in a manner that is entirely independent upon the structure of the resonators and their coupling. The experimental observations in [60] also show the onset of localized modes at the boundary of finite arrays of discrete mechanical resonators, implemented in the form of a chain of magnetically-coupled spinners. Topological boundary and interface modes in QP acoustic waveguides are also observed in [61], while reconfigurable QP acoustic crystals [62] are employed to experimentally observe their spectrum in the form of a Hofstadter butterfly [64]. Furthermore, the numerical results in [63] have shown how a Hofstadter spectrum also characterizes continuous structural beams supported by a QP array of ground springs, and how localized modes can be predicted through topological considerations on such spectrum. The studies referenced above provide insights into modes that are localized at edges or interfaces and suggest new methodologies for wave transport and localization. In addition, this body of work generally contributes to the literature that regards QP geometries as projections of higher dimensional manifolds onto lower dimensional lattices, and that explores topological properties of higher dimensional periodic systems, to assess properties in the lower dimensional physical space [65, 53, 55, 66].

In the context of utilizing synthetic dimensions to explore higher dimensional topological effects in lower dimensional systems, topological pumping emerges as a phenomenon of particular interest, whereby transitions of edge states from one boundary to another of a 1D system are induced by parametric variations along one additional (synthetic) dimension, either spatial [52, 67, 68, 69, 70, 71] or temporal [72, 73, 74, 75, 76, 77, 78]. A temporal pump embodies a 2D topological effect that governs the robust energy transport in systems of a single spatial dimension. While the concept is very promising and supported mostly by theoretical investigations, [79, 75, 76, 78] its experimental realization for

elastic waves has so far been elusive. Notable recent studies include the temporal pumping illustrated in a dimerized magneto-mechanical system emulating the Su-Schreefer-Heeger (SSH) model [74], and the mapping of egde state transitions in reconfigurable quasiperiodic acoustic lattices [62].

1.5 Motivation and Dissertation Outline

Linear locally resonant metamaterials and metastructures have been well studied and currently it is well known that locally resonant bandgap bandwidth is limited by the added inertia and the electromechanical coupling for mechanical and electromechanical metastructures, respectively. In addition, even though locally resonant bandgaps do not require a periodic arrangement of unit cells (unlike Bragg scattering-based bandgaps), most investigations have been limited to structures with identical resonators that are placed uniformly.

To enhance the vibration attenuation capabilities such as broadening the attenuation frequency bandwidth or controlling the vibration localization, this dissertation aims to expand the concept of linear LR metamaterials and metastructures. Two directions as summarized in the previous sections shed light onto performance enhancement: one is introducing designed nonlinearity, specifically considering bistable attachments; the other one is introducing aperiodicity, namely by considering resonators in quasiperiodic arrangements.

To this end, the subsequent chapters are outlined as follows. Chapter 2 investigates the performance of nonlinear mechanical locally resonant metastructures via bistable attachments, with experimental validation for a cantilever beam hosting an array of bistable magnetoelastic attachments. Chapter 3 studies the dynamic behavior and topology of mechanical locally resonant metastructures hosting quasiperiodic distributions of resonators, with experimental validation on the existence of additional topologically non-trivial bandgaps and edge-localized modes. Chapter 4 investigates the electromechanical locally resonant metastructures using quasiperiodically resonated shunt circuits, with experimental validation for a piezoelectric bimorph beam shunted to digitally programmable synthetic impedance

circuits. Chapter 5 investigates the temporal topological pumping in an electromechanical metastructure, with experimental validation using a piezoelectric bimorph beam connected to controllable negative capacitance circuits. Finally, Chapter 6 summarizes the contribution of this dissertation and discusses the potential directions for future research.

CHAPTER 2
MECHANICAL LOCALLY RESONANT METASTRUCTURES WITH BISTABLE ATTACHMENTS

2.1 Introduction

In this chapter, the aim is to explore amplitude-dependent bandwidth enhancement in locally resonant metamaterials/metastructures via bistable attachments. A lumped parameter model comprising a linear mass-spring chain with bistable attachments is considered for the purpose of a basic qualitative concept demonstration. Numerical studies simulate the system under low, moderate and high intensity excitations, so that the bistable attachments exhibit linear intrawell, nonlinear intrawell and nonlinear interwell oscillations, respectively. Additionally, escapes of the attachments from the potential wells under various forcing frequencies and amplitudes are predicted numerically. In addition, for experimental validation, a distributed parameter model consisting of a cantilever beam with bistable attachments is developed. Experimental results are then presented for a base-excited cantilever beam hosting seven bistable magnetoelastic attachments. Transition from a linear locally resonant bandgap to nonlinear attenuation is observed, and the amplitude-dependent bandwidth enhancement is shown.

2.2 Lumped Parameter Nonlinear Model

Consider the system of a linear mass-spring chain with bistable attachments as illustrated in Fig. 2.1. The system has $2N$ degrees of freedom (DOF) with N identical main masses, m, and N identical bistable attachment masses, m_a. The main masses are connected to each other by identical linear springs of stiffness k, while the springs between the main masses and the attachments are nonlinear with a negative linear stiffness k_{a1} and a positive

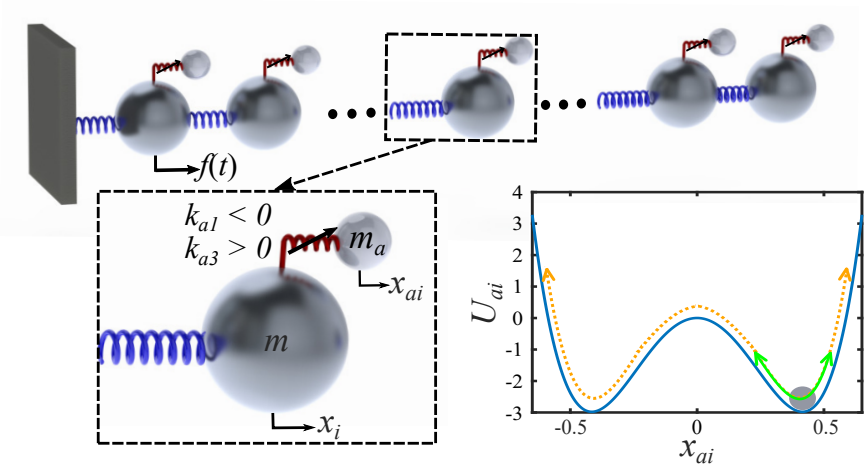

Figure 2.1: Schematic of a linear mass-spring chain with bistable attachments showing an inset of a unit cell. Bottom right plot shows the double-well potential of i-th bistable attachment, U_{ai}, as a function of relative displacement x_{ai}, with illustrations of intrawell (green line) and interwell (orange dotted line) oscillations.

cubic stiffness k_{a3}. The potential energy of the i-th bistable attachment with respect to the corresponding main mass is:

$$U_{ai} = \frac{1}{2}k_{a1}x_{ai}^2 + \frac{1}{4}k_{a3}x_{ai}^4. \tag{2.1}$$

Therefore the attachments exhibit a double-well potential with two stable equilibrium positions as shown in Fig. 2.1. A harmonic external force $f(t) = f_1 \cos \Omega t$ is applied to the first main mass. The governing equations of motion for the i-th main mass and the i-th attachment are:

$$(m + m_a)\ddot{x}_i + m_a\ddot{x}_{ai} - c\dot{x}_{i-1} + 2c\dot{x}_i - c\dot{x}_{i+1} - kx_{i-1} + 2kx_i - kx_{i+1} = f(t)\delta_{i1}, \tag{2.2}$$

$$m_a(\ddot{x}_i + \ddot{x}_{ai}) + c_a\dot{x}_{ai} + k_{a1}x_{ai} + k_{a3}x_{ai}^3 = 0, \tag{2.3}$$

where x_i is the absolute displacement of the i-th main mass, x_{ai} is the displacement of the i-th attachment relative to the i-th main mass, and δ_{ij} is the Kronecker delta. Eq. 2.2 and

Eq. 2.3 can be non-dimensionalized into:

$$(1+\mu)u_i'' + \mu u_{ai}'' - \zeta u_{i-1}' + 2\zeta u_i' - \zeta u_{i+1}' - u_{i-1} + 2u_i - u_{i+1} = p_i \delta_{i1} \cos(\omega\tau), \quad (2.4)$$

$$u_i'' + u_{ai}'' + \zeta_a u_{ai}' + \alpha^2 u_{ai} + u_{ai}^3 = 0, \quad (2.5)$$

where the non-dimensional displacements are $u_i = x_i/L_c$ and $u_{ai} = x_{ai}/L_c$ (for the characteristic frequency $\Omega_c = \sqrt{k/m}$ and the characteristic length $L_c = \sqrt{m_a\Omega_c^2/k_{a3}}$). Furthermore, the non-dimensional time $\tau = \Omega_c t$, excitation frequency $\omega = \Omega/\Omega_c$, excitation amplitude $p_i = f_i/m\Omega_c^2 L_c$, mass ratio $\mu = m/m_a$, damping $\zeta = c/m\Omega_c$ and $\zeta_a = c_a/m_a\Omega_c$, and $\alpha^2 = k_{a1}/m_a\Omega_c^2$ are defined, while $(\cdot)'$ denotes derivative with respect to non-dimensional time τ. With the choice of negative linear stiffness k_{a1}, α^2 is negative and there exist two stable equilibrium points for the attachment:

$$\bar{u}_{ai} = \pm\sqrt{-\alpha^2}, \quad (2.6)$$

where $\bar{u}_{ai}$ are the stable equilibrium positions for the i-th attachment. Equation 2.5 can be linearized around either of the two stable equilibrium positions. The resulting linear natural frequency, β, of the attachment around either of the two stable equilibrium positions is given by:

$$\beta = \sqrt{-2\alpha^2}. \quad (2.7)$$

2.2.1 Numerical Study

In this section, both the up-sweep and down-sweep frequency response of the lumped parameter system are presented. By varying the forcing amplitude, the amplitude-dependent behavior is investigated.

Analysis Approach

For the nonlinear system in Fig. 2.1, response to harmonic excitation may exhibit periodic and aperiodic oscillations of intrawell and interwell types as known from the vast literature of bistable structures [21, 22, 23, 20]. For the periodic steady-state solutions of u_i and u_{ai}, the method of harmonic balance is used (details of the harmonic balance method and its application examples for nonlinear structures can be found elsewhere [80, 81]). Since the system has cubic nonlinearity, the truncated Fourier series representation should contain a sufficient number of terms [81]; three harmonics are used here. Eqs. 2.8 and 2.9 represent the assumed three-term Fourier series expansion of the displacement of i-th main mass and the relative displacement of i-th bistable attachment, respectively.

$$\hat{u}_i = a_i + \sum_{m=1}^{3} \left[A_{i,m} \cos\left(\frac{2\pi m t}{T}\right) + B_{i,m} \sin\left(\frac{2\pi m t}{T}\right) \right], \qquad i = 1, 2, ..., N \tag{2.8}$$

$$\hat{u}_{ai} = a_{ai} + \sum_{m=1}^{3} \left[A_{ai,m} \cos\left(\frac{2\pi m t}{T}\right) + B_{ai,m} \sin\left(\frac{2\pi m t}{T}\right) \right], \qquad i = 1, 2, ..., N \tag{2.9}$$

The resulting nonlinear algebraic equations for the Fourier coefficients are then solved using the multivariate Newton-Raphson method. For aperiodic solutions (including chaos), the Runge-Kutta method (time-domain numerical simulation) is used.

Case Study

The numerical case study considers a 10-DOF system, which includes 5 main masses and 5 bistable attachments. Non-dimensional parameters used in the numerical study are summarized in Table 2.1. To target the second mode of the plain mass-spring chain (for concept demonstration), the bistable attachments are tuned to have $\beta = \omega_{n2} = 0.8308$ (using $\alpha^2 = -0.3451$), where ω_{n2} is the second natural frequency of the 5-DOF plain mass-spring

Table 2.1: Non-dimensional parameters for the lumped parameter model

Symbol	Description	Value
N	Number of unit cells	5
Ω_c	Characteristic frequency	1
L_c	Characteristic length	$\sqrt{5}$
μ	Mass ratio	0.1
η	Damping for main masses	0.1
η_a	Damping for attachments	0.02
β	Linear natural frequency	0.8308

chain. Harmonic force is applied to the first main mass, and six levels of non-dimensional forcing amplitude are simulated. For the frequency response analysis of the nonlinear system, simulations are performed for both up and down frequency sweeps at each forcing amplitude over the non-dimensional frequency range of $0.6 < \omega < 1.1$.

Simulated non-dimensional results of up-sweep frequency responses for the 5-th attachment and 5-th mass are presented in Fig. 2.2 using the root-mean-square (RMS) value at each frequency. Whereas Fig. 2.3 shows the simulated down-sweep frequency responses for the 5-th attachment and 5-th mass. Here the RMS value instead of the amplitude value of the displacements is used in the plots to capture the aperiodic dynamics of the system. In Fig. 2.2b and Fig. 2.3b, the shaded region shows the linear bandgap based on the theory developed for a finite and discrete metamaterial chain [11]. The range of the bandgap is:

$$\frac{\beta}{\sqrt{2}}\sqrt{(1+\mu+4\Gamma)-\sqrt{(1+\mu+4\Gamma)^2-16\Gamma}} < \omega < \beta\sqrt{1+\mu}, \tag{2.10}$$

where $\Gamma = 1/\beta^2$. For very low forcing levels (e.g. $p = 5.0 \times 10^{-4}$), the system exhibits linear/quasilinear behavior, yielding a locally resonant bandgap. The second mode (the target mode) of the plain mass-spring chain is attenuated while additional resonances appear, which is similar to the behavior of just using linear locally resonant attachments. As the forcing level increases, nonlinear intrawell softening and interwell oscillations are enabled gradually. Especially interwell chaotic oscillations of the attachments yield a very broad-

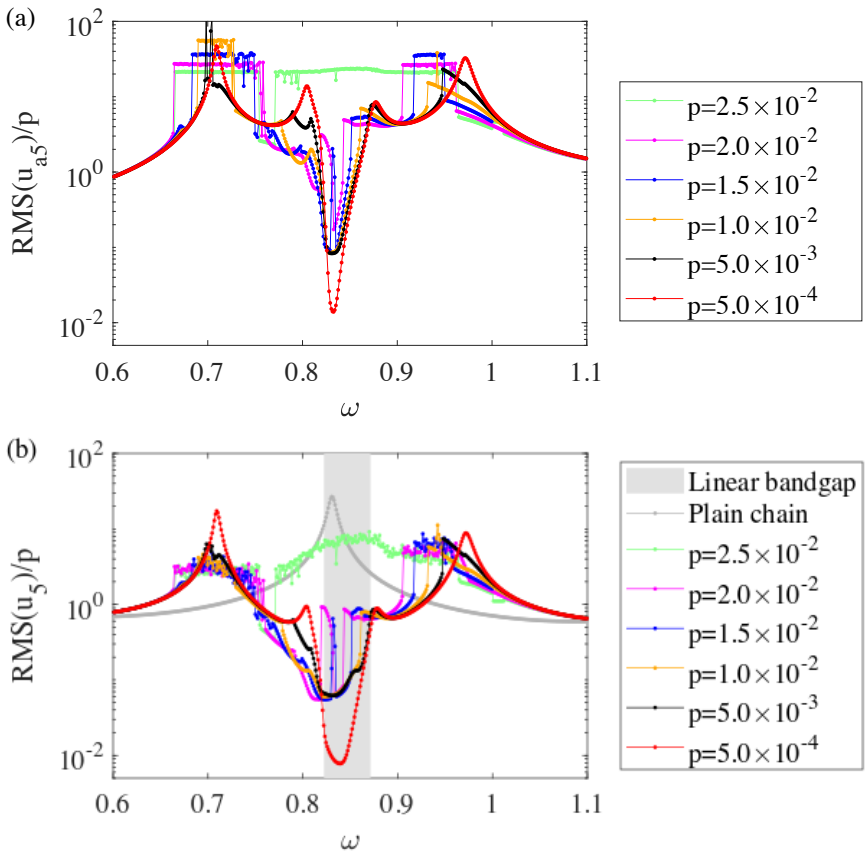

Figure 2.2: Numerical simulation results for non-dimensional displacement up-sweep frequency response of 5-th attachment (a) and 5-th mass (b) under different force levels normalized by the non-dimensional forcing amplitude.

band attenuation. In addition, time histories of the 5-th mass and 5-th attachment under two different excitation levels at the same frequency ($\omega = 0.7091$) for the down-sweep case illustrate the amplitude-dependent dynamic behavior of the system in a more direct way as shown in Fig. 2.4. The comparison shows that the attachment oscillates periodically around one of the equilibrium location under low forcing level ($p = 5.0 \times 10^{-3}$), while it oscillates chaotically between two equilibrium locations under high forcing level ($p = 2.5 \times 10^{-2}$).

For design and analysis purposes, it is of interest to quantify the level of forcing intensity required for escape from the potential wells of the bistable attachments. Here, a numerical analysis is performed to this end, as summarized next (analytical approaches exist for lower DOF systems [82]). Figure 2.5 presents maps for the prediction of all five

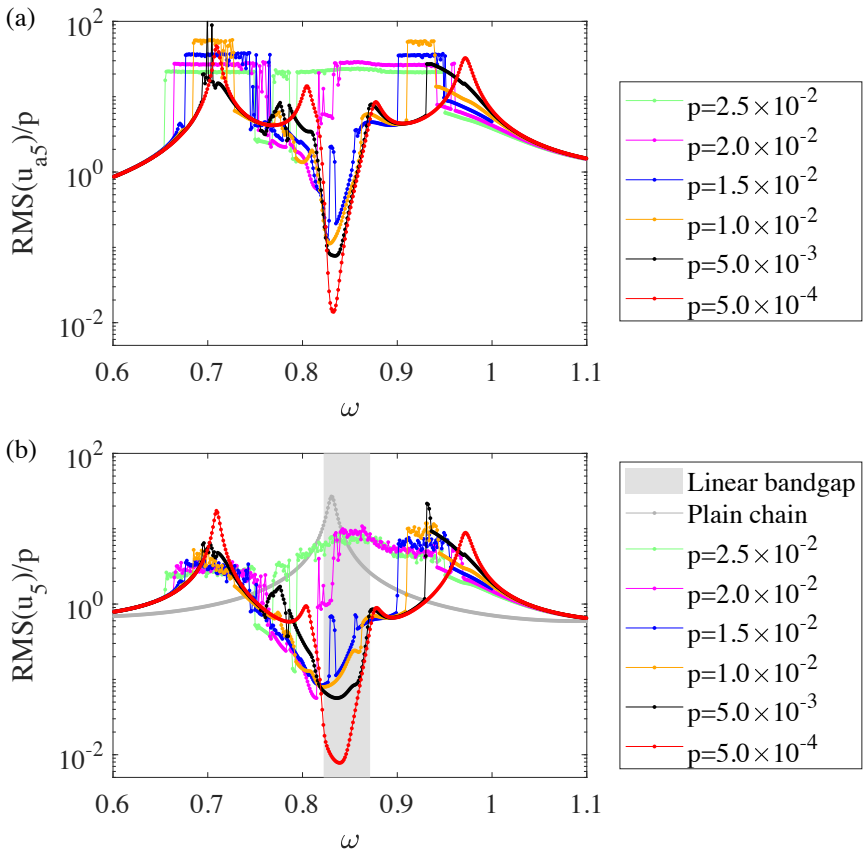

Figure 2.3: Numerical simulation results for non-dimensional displacement down-sweep frequency response of 5-th attachment (a) and 5-th mass (b) under different force levels normalized by the non-dimensional forcing amplitude.

attachments' escape from the potential well by varying the forcing frequency and amplitude. The maps are produced by varying the normalized frequency from 0.6 to 1.1 with increments of 5×10^{-4}, while varying the normalized forcing amplitude from 0 to 0.1 with steps of 5×10^{-4}. Both the black region and the yellow region represent intrawell oscillations, with black denoting periodic oscillations using the harmonic balance method, and yellow indicating aperiodic oscillations from time-domain simulations. Red regions represent interwell chaotic oscillations of the attachments based on time-domain simulations. As can be seen from the maps in Fig. 2.5, a threshold forcing amplitude exists for the bistable attachments to undergo intrawell oscillations for all excitation frequencies. Remarkably, interwell oscillations are easier to form with a lower forcing amplitude especially around

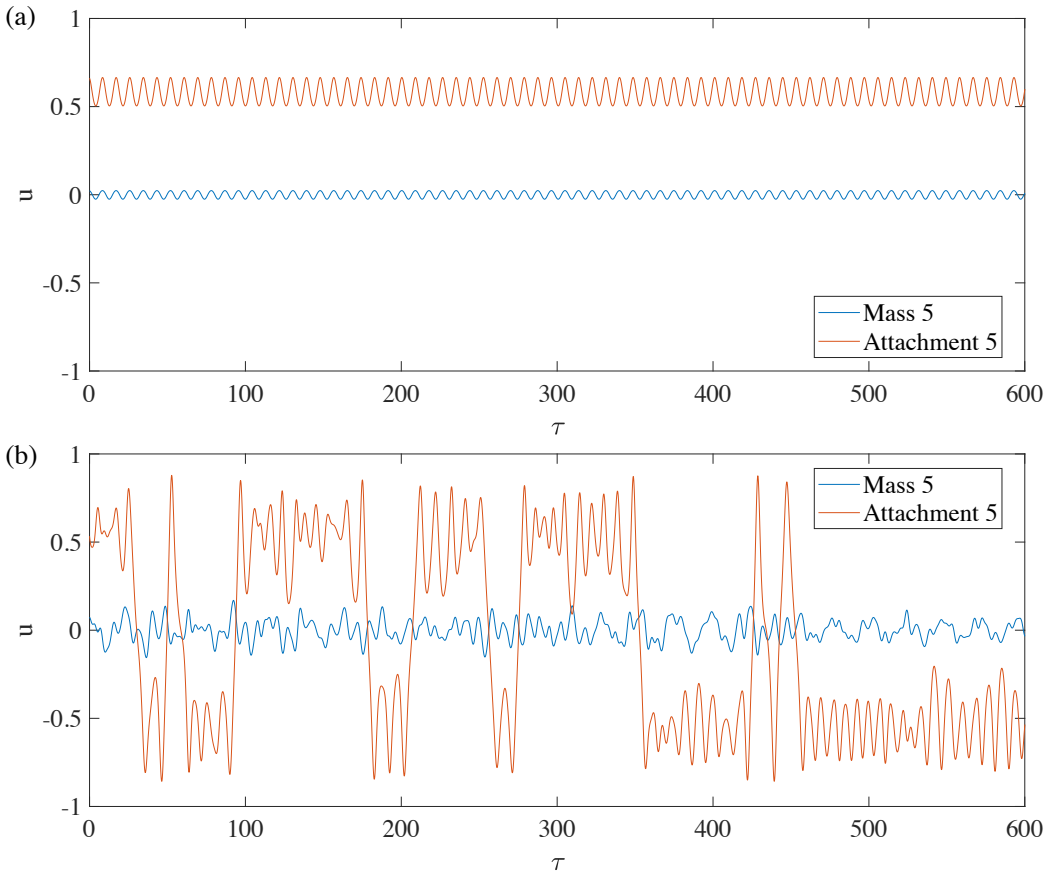

Figure 2.4: Numerical simulation results for the time history of non-dimensional displacements for the 5-th mass and 5-th attachment under different excitation amplitudes at $\omega = 0.7091$: (a) $p = 5 \times 10^{-3}$ and (b) $p = 2.5 \times 10^{-2}$.

the two resonances of the linear/quasilinear frequency response curves (cf. the frequency axes in Fig. 2.2b and Fig. 2.5).

2.2.2 Experimental Validation

Experimental investigations are presented next to demonstrate the overall concept of bistable locally resonant metastructures and validate amplitude-dependent bandwidth enhancement.

Experimental Setup

The metastructure is physically implemented in the form of a cantilever beam with 7 magnetoelastic beams as bistable local attachments (Fig. 2.6). The experimental setup shown

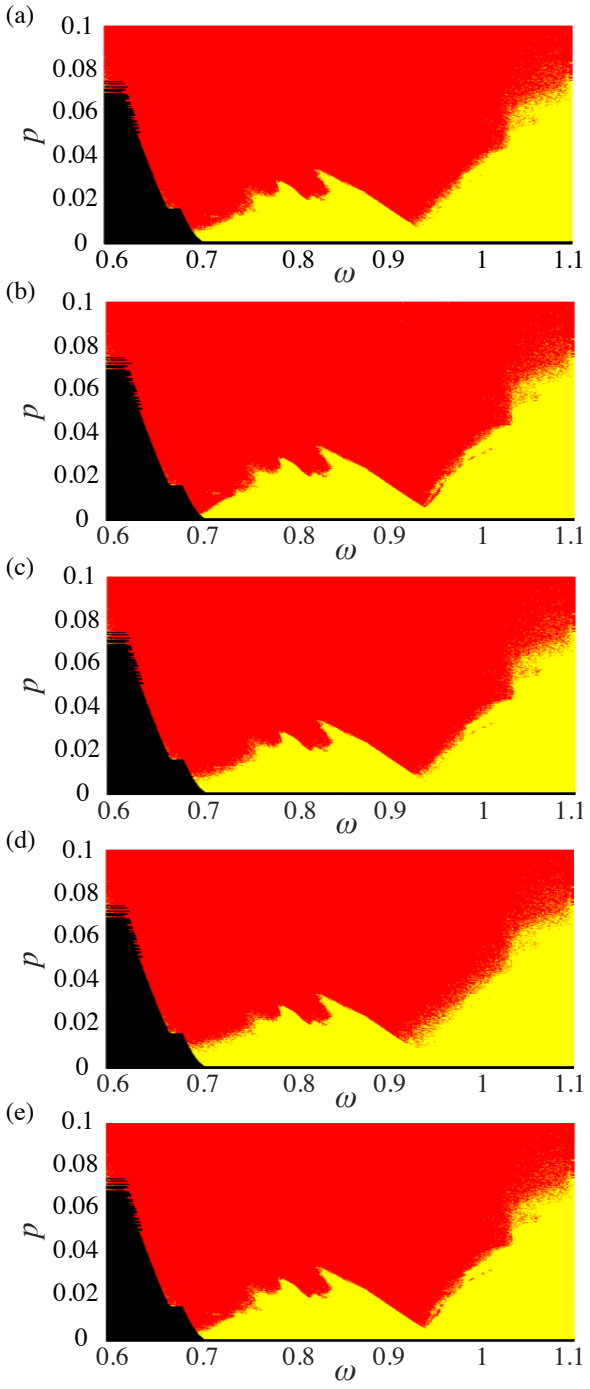

Figure 2.5: Numerical map to quantify the forcing required for potential well escape of the attachments as a function of normalized frequency and normalized forcing amplitude: (a)-(e) correspond to attachment 1 to 5 respectively. Black region: intrawell periodic oscillations; Yellow region: intrawell aperiodic oscillations; Red region: interwell aperiodic/chaotic oscillations.

in Fig. 2.6 consists of a 3.175 mm thick, 3.175 cm wide, and 88.9 cm long aluminum beam, divided into 7 unit cells. The bistable attachments are made from spring steel cantilevers with tip masses. Each spring steel cantilever is 9.525 mm wide, 0.254 mm thick and extending the edge of the extruded slot by 3.94 cm long. Two 9.525 mm cube-shaped permanent magnets are placed at the free end of each spring steel cantilever. Each magnet has a hole through the center which is perpendicular to the magnetization direction. To realize the bistability, the other pair of two magnets are attached to the aluminum beam (Fig. 2.6a) and two stable equilibrium positions are obtained (Fig. 2.6b).

Since the cantilever is clamped on one side of the aluminum beam, the thickness of the beam affects the symmetry of the double-well potential of the attachments. Spacers are placed between the beam and magnets to compensate for the beam thickness so that the double-well potential can be as symmetric as possible. The beam is clamped vertically to an APS-113 long stroke shaker, which excites the beam by base motion horizontally. The shaker is driven by an APS-125 amplifier and controlled by a SPEKTRA VCS-201 controller for the purpose of having a harmonic base acceleration at specified amplitudes and frequencies. Base acceleration measured by an accelerometer is fed back to the VCS-201 controller. The tip velocity of the beam is measured with a Polytec OFV-505 laser Doppler vibrometer (LDV) near the free end of the beam. The transmissibility frequency response of the beam is obtained by sweeping the excitation frequency up from 8 Hz to 20 Hz and down from 20 Hz to 8 Hz at a rate of 2.5 Hz/min for different base acceleration levels.

Experimental Results

As shown in Fig. 2.7, the unit cells are designed to allow flexibility in the potential wells of the bistable attachments by varying the distance between magnets, which is quantified by the vertical distance, d, between the lower edge of the rectangular slot and the upper face of the cubic magnet. The transmissibility frequency response in Fig. 2.7a is defined as the

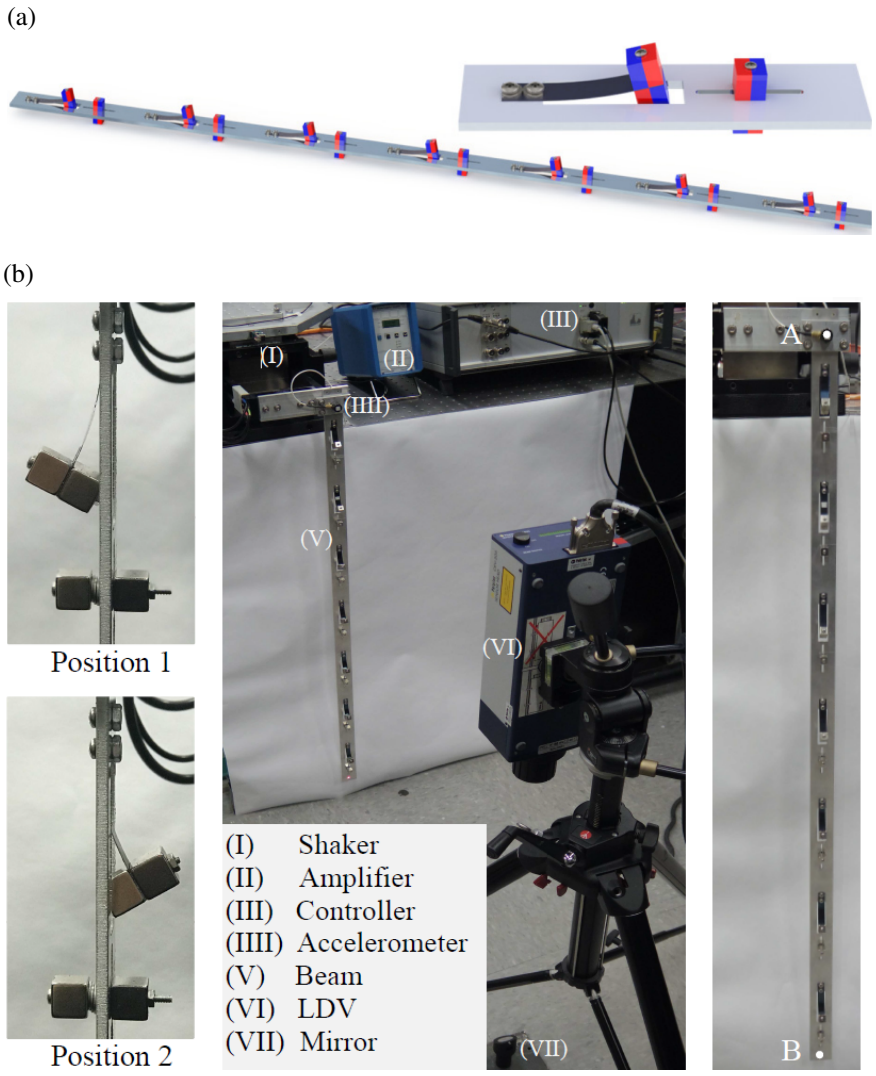

Figure 2.6: (a) LR metastructure (cantilevered beam with 7 magnetoelastic bistable beam attachments) with a close up view of a unit cell (magnet polarity: red is north and blue is south). (b) Left: A bistable attachment in its two stable equilibrium positions. Middle: Experimental setup with an LDV oriented vertically at a 45-degree mirror to measure the transverse tip velocity of the beam. Right: Front view of the beam.

ratio of the steady-state velocity at Point B to that at Point A on the spring steel cantilever (shown in Fig. 2.7b). Since the clamping of the spring steel cantilever is asymmetric, the resulting double-well potential is not perfectly symmetric in the experiments (i.e., a small amount of quadratic nonlinearity is inevitable). Slightly different post-buckled linear natural frequencies (previously defined as the non-dimensional β) are observed for the bistable attachment in stable equilibrium positions 1 and 2 (while it is negligible here, the effect of

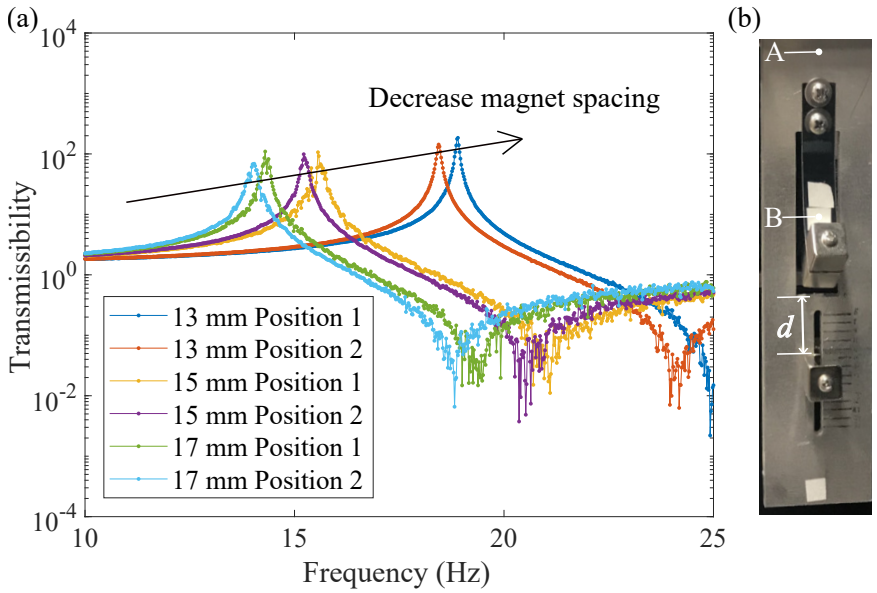

Figure 2.7: (a) Effect of magnet spacing on the stable equilibrium positions of a bistable attachment (experimental) and (b) a close-up view.

significantly asymmetric potential wells can be found in the nonlinear energy harvesting literature [83, 84]). As the distance between magnets decreases, the post-buckled linear natural frequency of the bistable attachment increases, which is a useful design and tuning parameter. With $d = 15$ mm, the post-buckled linear natural frequency is identified to be 15.1 Hz. This magnet spacing is selected to target the second mode neighborhood of the main structure in this work (as will be discussed next). Characterization of the unit cell with $d = 15$ mm is performed as shown in Fig. 2.8. As the base excitation level is increased, intrawell linear resonance turns into intrawell nonlinear softening, and then eventually interwell oscillations and chaos are observed with a substantial bandwidth, as expected from individual bistable beam dynamics [20].

Having analyzed an individual bistable unit cell in detail, experiments are performed on the main cantilevered structure with and without bistable attachments. In Fig. 2.9, the experimentally measured transmissibility frequency response of the beam under base excitation is plotted for various RMS base acceleration levels and for both up and down frequency sweep. Transmissibility here is defined as the ratio of the steady-state velocity at the tip of

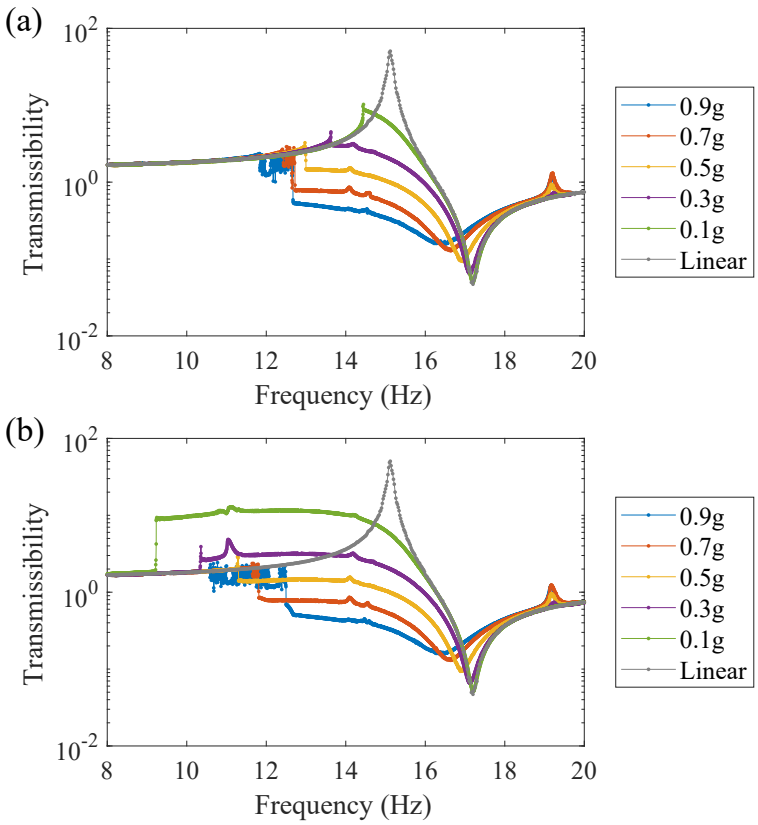

Figure 2.8: Amplitude-dependent nonlinear characterization of a unit cell with magnet spacing $d = 15$ mm: (a) up-sweep and (b) down-sweep (experimental).

the aluminum beam (Point B in Fig. 2.6b) to that at its base (Point A in Fig. 2.6b). The plain beam (baseline) here is the main cantilever without the bistable attachments, specifically by removing all 7 magnetoelastic cantilevers and the corresponding pairs of magnets at the tip, while keeping all other pairs of magnets on the beam with $d = 15$ mm. The second mode of the plain beam is identified to be at 16.14 Hz. The distance between the magnets can be tuned so that post-buckled linear natural frequency of the bistable attachments is 16.14 Hz or higher. However, as desired post-buckled linear natural frequency, the distance between the magnets must be decreased, resulting in deeper potential wells. In view of the experimental limitations (to avoid very deep potential wells and achieve escape from the potential wells for reasonable base excitation levels), $d = 15$ mm is deemed suitable to target the second mode neighborhood of the plain beam (cf. the frequency axes in Figs. 2.8 and 2.9). Note that, variations in manually adjusted magnet spacing can lead to slightly different

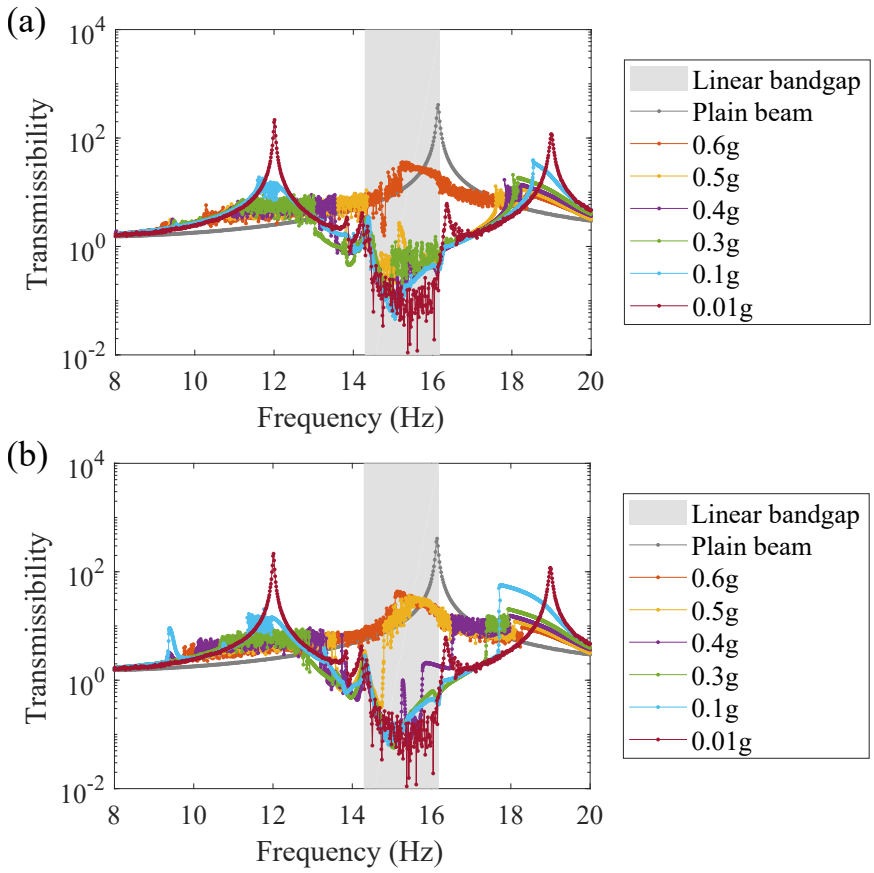

Figure 2.9: Amplitude-dependent nonlinear dynamics of the metastructure with bistable attachments, showing a dramatic enhancement of the attenuation bandwidth (with comparisons against the plain beam and the locally resonant linear bandgap): (a) up-sweep and (b) down-sweep (experimental).

post-buckled linear natural frequencies for the bistable attachments. The post-buckled linear natural frequencies of all seven bistable attachments on the beam then are identified individually, and the average value is 14.3 Hz. Even though the bistable attachments are not tuned to target the first mode of the beam exactly, the desired trends of vibration attenuation are kept, confirming the robustness of the nonlinear attenuation mechanism. At a very low RMS base acceleration level ($0.01g$), it is observed that the bistable attachments stay within the potential well, vibrating linearly/quasilinearly around their respective static equilibria. The metastructure experiences a bandgap similar to the one with linear local attachments, with the second mode of the plain beam attenuated while new resonances appear. The shaded region shows the linear locally resonant bandgap estimate based on the

theory developed for finite and continuous metastructures [10], $\omega_t < \omega < \omega_t\sqrt{1+\mu}$, with the target frequency $\omega_t = 14.3$ Hz and mass ratio $\mu = 0.27$. As the base excitation level increases, intrawell softening of the attachments start triggering nonlinear attenuation first. Further increase in the base excitation intensity leads to a dramatic bandwidth enhancement (as compared to the linear bandgap) when interwell chaotic motions of the attachments are manifested.

2.3 Distributed Parameter Nonlinear Model

In order to have a quantitative comparison with the experimental results, a distributed parameter model is developed in this section. The system consists of a cantilever beam under transverse vibration with S bistable attachments as shown in Fig. 2.10. The beam is

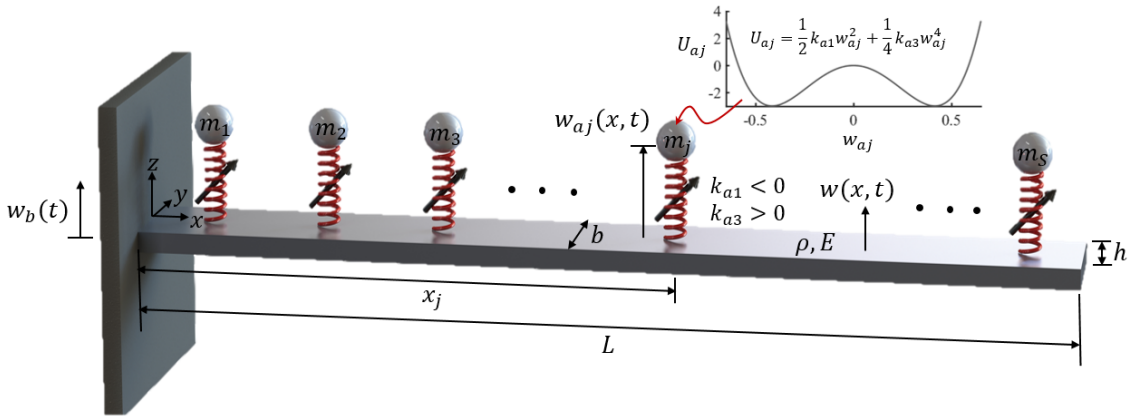

Figure 2.10: Schematic of the nonlinear locally resonant metastructure (cantilever with bistable attachments) under base excitation.

clamped at one end ($x = 0$) and free to vibrate at the other end ($x = L$). It has width b, thickness h, Young's modulus E, and density ρ. Each attachment is connected to the beam through a bistable spring with negative linear stiffness k_{a1} and positive cubic stiffness k_{a3}. The total transverse displacement, $w_t(x,t)$, of the cantilever beam under base excitation is defined as:

$$w_t(x,t) = w_b(t) + w(x,t), \tag{2.11}$$

where $w_b(t)$ is the base displacement at $x = 0$ and $w(w, t)$ is the beam displacement relative to the moving space at position x and time t. The governing equation of the beam based on Euler–Bernoulli beam theory is:

$$EI\frac{\partial^4 w(x,t)}{\partial x^4}+m\frac{\partial^2 w(x,t)}{\partial t^2}-\sum_{j=1}^{S}\left[k_{a1}w_{aj}(t)+k_{a3}w_{aj}^3(t)\right]\delta(x-x_j) = -m\frac{\mathrm{d}^2 w_b(t)}{\mathrm{d}t^2}. \quad (2.12)$$

At this point, the system is assumed to be undamped and modal damping will be introduced at a later stage. The associated equations of motion for the attachments are:

$$m_j\frac{\mathrm{d}^2[w(x_j,t)+w_{aj}(t)]}{\mathrm{d}t^2} + k_{a1}w_{aj}(t) + k_{a3}w_{aj}^3(t) = -m_j\frac{\mathrm{d}^2 w_b(t)}{\mathrm{d}t^2}, \qquad j = 1, 2, \ldots, S \quad (2.13)$$

where $w_{aj}(t)$ is the relative displacement of the j-th attachment with respect to $w(x_j, t)$, x_j is the location of the j-th attachment, $I = bh^3/12$ is second moment of area about y-axis, $m = \rho bh$ is the mass per length of the beam, and m_j is the mass of the j-th attachment. The boundary conditions of the clamped-free beam are given by:

$$w(0,t) = 0, \quad (2.14a)$$

$$\frac{\partial w(0,t)}{\partial x} = 0, \quad (2.14b)$$

$$EI\frac{\partial^2 w(L,t)}{\partial x^2} = 0, \quad (2.14c)$$

$$EI\frac{\partial^3 w(L,t)}{\partial x^3} = 0. \quad (2.14d)$$

The study mainly focuses on the frequency range in the neighbourhood of one target mode (i.e., the second mode) of the cantilever beam with no attachments (plain beam). Nonlinear modal interactions are neglected since the modes of the plain beam are well separated. As mentioned in [5], an expansion using the mode shapes of a uniform clamped-free beam, $\phi(x)$, can provide a significant simplification in the analysis. The approximate

solution of the displacement of the beam is:

$$w(x,t) = \sum_{r=1}^{N} \eta_r(t)\phi_r(x), \tag{2.15}$$

where N is the number of modes in the expansion and $\eta_r(t)$ is the modal weighting of the r-th mode of the clamped-free beam. The mass-normalized mode shapes of the beam are given by the following equation:

$$\begin{aligned}\phi_r(x) = \frac{1}{\sqrt{mL}}\Bigg[&\cos\left(\frac{\lambda_r x}{L}\right) - \cosh\left(\frac{\lambda_r x}{L}\right) \\ &+ \left(\frac{\sin\lambda_r - \sinh\lambda_r}{\cos\lambda_r + \cosh\lambda_r}\right)\left(\sin\left(\frac{\lambda_r x}{L}\right) - \sinh\left(\frac{\lambda_r x}{L}\right)\right)\Bigg], \quad r = 1,2,\ldots,N\end{aligned} \tag{2.16}$$

where λ_r is the r-th positive real solution of the characteristic equation given in:

$$\cos\lambda\cosh\lambda + 1 = 0. \tag{2.17}$$

The mode shapes of the clamped-free beam satisfy the orthogonality conditions as shown below:

$$\int_{x=0}^{x=L} \phi_r(x) m \phi_s(x) \mathrm{d}x = \delta_{rs}, \qquad r,s = 1,2,\ldots \tag{2.18a}$$

$$\int_{x=0}^{x=L} \phi_r(x) EI \phi_s''''(x) \mathrm{d}x = \omega_r^2 \delta_{rs}, \qquad r,s = 1,2,\ldots \tag{2.18b}$$

where ω_r is the natural frequency of the r-th mode of the clamped-free beam. Substituting Eq. 2.15 into Eq. 2.12 gives the following equation:

$$\begin{aligned}EI\sum_{r=1}^{N}\eta_r(t)\phi_r''''(x) + m\sum_{r=1}^{N}\ddot{\eta}_r(t)\phi_r(x) - \sum_{j=1}^{S}\big[&k_{a1}w_{aj}(t) \\ &+ k_{a3}w_{aj}^3(t)\big]\delta(x - x_j) = -m\ddot{w}_b(t),\end{aligned} \tag{2.19}$$

where $()'$ denotes the derivative with respect to space variable x and $\dot{()}$ denotes the derivative with respect to time t. Multiplying Eq. 2.19 by $\phi_s(x)$, integrating from $x = 0$ to $x = L$, and applying the orthogonality conditions of the mode shapes shown in Eqs. 2.18a and 2.18b yield:

$$\ddot{\eta}_r(t) + \omega_r^2 \eta_r(t) - \sum_{j=1}^{S} \left[k_{a1} w_{aj}(t) + k_{a3} w_{aj}^3(t)\right] \phi_r(x_j) = -m\ddot{w}_b(t) \int_{x=0}^{x=L} \phi_r(x) \mathrm{d}x. \tag{2.20}$$

Substitute Eq. 2.15 into Eq. 2.13 gives:

$$m_j \left[\sum_{r=1}^{N} \ddot{\eta}_r(t) \phi_r(x_j) + \ddot{w}_{aj}(t) \right] + k_{a1} w_{aj}(t) + k_{a3} w_{aj}^3(t) = -m_j \ddot{w}_b(t), \quad j = 1, 2, \ldots, S. \tag{2.21}$$

Given that the nonlinearity is in the relative displacement of the attachments, Eq. 2.20 can be re-written by substituting Eq. 2.21 as the following:

$$\ddot{\eta}_r(t) + \omega_r^2 \eta_r(t) + \sum_{j=1}^{S} m_j \phi_r(x_j) \sum_{k=1}^{N} \ddot{\eta}_k(t) \phi_k(x_j) + \sum_{j=1}^{S} m_j \ddot{w}_{aj}(t) \phi_r(x_j) = q_r(t), \quad r = 1, 2, \ldots, N \tag{2.22}$$

where

$$q_r(t) = -\ddot{w}_b(t) \left(\int_{x=0}^{x=L} m \phi_r(x) \mathrm{d}x + \sum_{j=1}^{S} m_j \phi_r(x_j) \right). \tag{2.23}$$

Equations (2.21) and (2.22) form a system of $N + S$ coupled second order ordinary differential equations. Such system can be cast into the matrix form:

$$\mathbf{M}\ddot{\mathbf{u}} + \mathbf{K}\mathbf{u} + \mathbf{G}\mathbf{u}^3 = \mathbf{F}(t), \tag{2.24}$$

where $\mathbf{u} = \begin{bmatrix} \eta_1 & \eta_2 & \cdots & \eta_N & w_{a1} & w_{a2} & \cdots & w_{aS} \end{bmatrix}^\top$ contains the modal weightings of

the beam and the relative displacements of the bistable attachments. The mass matrix $\mathbf{M}$, linear stiffness matrix $\mathbf{K}$ and cubic stiffness matrix $\mathbf{G}$ are:

$$\mathbf{M} = \begin{bmatrix} \mathbf{M_{11}} & \mathbf{M_{12}} \\ \mathbf{M_{21}} & \mathbf{M_{22}} \end{bmatrix}, \qquad \mathbf{K} = \begin{bmatrix} \mathbf{K_{11}} & \mathbf{0} \\ \mathbf{0} & \mathbf{K_{22}} \end{bmatrix},$$
$$\mathbf{G} = \begin{bmatrix} \mathbf{0} & \mathbf{0} \\ \mathbf{0} & \mathbf{G_{22}} \end{bmatrix}, \tag{2.25}$$

where $\mathbf{M_{11}}$ is a $N \times N$ matrix, with the entries: $m_{mn} = \delta_{mn} + \sum_{j=1}^{S} m_j \phi_m(x_j)\phi_n(x_j)$; $\mathbf{M_{12}}$ is a $N \times S$ matrix, with the entries: $m_{mq} = m_q \phi_m(x_q)$; $\mathbf{M_{21}}$ is a $S \times N$ matrix, with the entries: $m_{pn} = m_p \phi_n(x_p)$; $\mathbf{M_{22}}$ is a $S \times S$ matrix, with the entries: $m_{pq} = \delta_{pq} m_p$; $\mathbf{K_{11}}$ is a $N \times N$ diagonal matrix, with the entries: $k_{mn} = \delta_{mn}\omega_m^2$; $\mathbf{K_{22}}$ is a $S \times S$ diagonal matrix, with the entries: $k_{pq} = \delta_{pq} k_{a1}$; $\mathbf{G_{22}}$ is a $S \times S$ diagonal matrix, with the entries: $G_{pq} = \delta_{pq} k_{a3}$. On the right hand side of Eq. 2.24, the forcing vector is:

$$\mathbf{F} = \begin{bmatrix} \mathbf{F_1} \\ \mathbf{F_2} \end{bmatrix}, \tag{2.26}$$

where $\mathbf{F_1}$ is a $N \times 1$ vector, with the entries:

$$f_m = q_m(t) = -\ddot{w}_b(t)\left[\int_{x=0}^{x=L} m\phi_m(x)\mathrm{d}x + \sum_{j=1}^{S} m_j \phi(x_j)\right]. \tag{2.27}$$

$\mathbf{F_2}$ is a $S \times 1$ vector, with the entries: $f_p = -m_p \ddot{w}_b(t)$. For all the indices above, $m, n = 1, 2, \ldots, N$ and $p, q = 1, 2, \ldots, S$.

Equation 2.24 can be rearranged as:

$$\ddot{\mathbf{u}} + \mathbf{\Lambda u} + \mathbf{\Psi u}^3 = \delta, \tag{2.28}$$

where $\mathbf{\Lambda} = \mathbf{M^{-1}K}$, $\mathbf{\Psi} = \mathbf{M^{-1}G}$, $\delta = \mathbf{M^{-1}F}$. Equation 2.28 can be further turned into

first order state space form:

$$\dot{\mathbf{z}} = \mathbf{A_0 z} + \mathbf{Q z}^3 + \mathbf{R}, \tag{2.29}$$

where

$$\mathbf{z} = \begin{bmatrix} \mathbf{u} \\ \dot{\mathbf{u}} \end{bmatrix}, \mathbf{A_0} = \begin{bmatrix} \mathbf{0} & \mathbf{I} \\ -\mathbf{\Lambda} & \mathbf{0} \end{bmatrix}, \mathbf{Q} = \begin{bmatrix} \mathbf{0} & \mathbf{0} \\ -\mathbf{\Psi} & \mathbf{0} \end{bmatrix}, \mathbf{R} = \begin{bmatrix} \mathbf{0} \\ \delta \end{bmatrix}. \tag{2.30}$$

For the nonlinear spring with a negative linear stiffness ($k_{a1} < 0$) and a positive cubic stiffness ($k_{a3} > 0$), the origin ($w_{aj} = 0$) of the attachment becomes unstable and there exist two stable equilibrium points, $\bar{w}_{aj,1}$ and $\bar{w}_{aj,2}$, in the potential energy plot.

$$\bar{w}_{aj,1} = -\sqrt{-k_{a1}/k_{a3}}, \tag{2.31a}$$

$$\bar{w}_{aj,2} = \sqrt{-k_{a1}/k_{a3}}. \tag{2.31b}$$

Equation 2.21 can be linearized around either of the two stable equilibrium points, and the resulting linear natural frequency, $\bar{\omega}_a$, of the attachment is given by:

$$\bar{\omega}_a = \sqrt{-2k_{a1}/m_r}. \tag{2.32}$$

2.3.1 Numerical Study

In this section, both the up-sweep and down-sweep frequency responses of the distributed parameter system are presented. By varying the base excitation amplitude, the amplitude-dependent behavior is investigated.

Analysis Approach

For the nonlinear system under harmonic base excitation, the response can exhibit periodic and aperiodic oscillations related to intrawell and interwell oscillations of the attachments. As in Section 2.2.1, the harmonic balance method is applied to solve for the periodic steady-state solutions of η_r and w_{aj}. Eqs. 2.33 and 2.34 represent the assumed three-term Fourier

series expansion of the modal weighting of the r-th mode and relative displacement of j-th bistable attachment, respectively.

$$\hat{\eta}_r = a_r + \sum_{m=1}^{3} \left[A_{r,m} \cos\left(\frac{2\pi m t}{T}\right) + B_{r,m} \sin\left(\frac{2\pi m t}{T}\right) \right], \qquad r = 1, 2, ..., N \tag{2.33}$$

$$\hat{w}_{aj} = a_{aj} + \sum_{m=1}^{3} \left[A_{aj,m} \cos\left(\frac{2\pi m t}{T}\right) + B_{aj,m} \sin\left(\frac{2\pi m t}{T}\right) \right], \qquad j = 1, 2, ..., S \tag{2.34}$$

Again, since a closed-form solution is beyond reach for such a nonlinear and high DOF system, Newton-Raphson method is employed to assist finding the Fourier series expansion coefficients. Runge-Kutta method (time-domain numerical simulation) is utilized to calculate aperiodic solutions (including chaos) when Newton-Raphson method does not yield a convergent harmonic balance solution (in aperiodic response forms).

Case Study

Here, the steady-state response of the system is investigated as a function of frequency under various excitation amplitudes. Parameters for the case study are chosen and adjusted according to the experimental setup that will be presented in the following section. All the attachments are assumed to have the same mass m_r, and all the springs have the same linear stiffness k_{a1} and cubic stiffness k_{a3}. Table 2.2 summarizes all the parameters of the system and the updated parameters used in the numerical investigations.

The first three resonant frequencies of the clamped-free cantilever beam without attachments (plain beam) are: 2.55 Hz, 15.9 Hz and 44.55 Hz as seen in Fig. 2.11. Transmissibility here and in the rest of the section is defined as the ratio of the steady-state velocity at the tip of the aluminum beam to that at its base. Since the first three modes of the plain beam are well separated, modal interactions are neglected with a focus on the primary resonance

Table 2.2: Parameters for the distributed parameter model

Symbol	Parameter	Value	Unit
L	Length of the beam	0.889	m
b	Width of the beam	3.175	cm
h	Thickness of the beam	3.175	mm
h_a	Adjusted thickness of the beam	2.6	mm
E	Young's modulus of the beam	69	GPa
ρ	Density of the beam	2700	kg/m^3
ρ_a	Adjusted density of the beam	2970	kg/m^3
m_r	Attachment mass	36	g
k_{a1}	Spring linear stiffness	-63.451	N/m
k_{a3}	Spring cubic stiffness	634509	N/m^3
ζ_b	Modal damping for the beam	0.002	
ζ_a	Damping ratio for the attachments	0.02	
N	Number of modes in expansion	10	
S	Number of attachments	7	

around the mode of interest (which is the second mode).

Based on Eqs. 2.31a and 2.31b, and Eq. 2.32, parameters of the nonlinear springs are obtained from the equilibrium positions of the bistable attachments ($\bar{w}_{aj,1} = 0.75$ cm and $\bar{w}_{aj,2} = -0.75$ cm) and the linear natural frequency around either of the equilibrium positions ($\bar{\omega}_a = 16.8$ Hz) measured in the experiments. Here, $\bar{\omega}_a$ is in the neighbourhood of the second mode of the plain beam. It should be noted that the values of thickness and density for the beam used in the simulations (adjusted thickness h_a and adjusted density ρ_a) are slightly different than the actual thickness and density of the beam to compensate the non-uniformity of the beam implemented in the experiments, which includes extruded cuts, holes and added point masses. This is a reasonable approach given the long wavelengths in the modal neighborhood of interest. In addition, in the numerical analysis, for better consistency with experiments, damping (modal damping for the beam and damping ratios for the bistable attachments) is added to the previously derived equations of motion in Eq. 2.21 and Eq. 2.22. For simplicity, all the modes of the beam are assumed to have the same modal damping, $\zeta_r = 0.002$, and all the bistable attachments are assumed to have

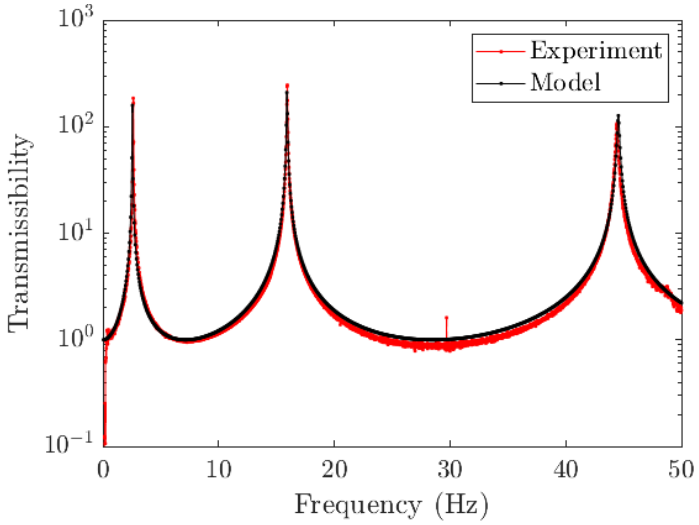

Figure 2.11: Linear transmissibility of the clamped-free beam without attachments (plain beam). The first three modes are well separated. Black curve shows the simulated results based on the adjusted (updated) parameters; red curve shows the experimental data.

the same damping ratio, $\zeta_a = 0.02$. As can be seen in Fig. 2.11, the simulated response of plain beam based on the adjusted parameters matches very well with experimental data.

Since the behavior of the nonlinear system is amplitude dependent (i.e., base excitation amplitude dependent), different levels of base excitation should be explored. Four different cases are simulated and the root-mean-square (RMS) values of the base acceleration are: $0.005g$, $0.1g$, $0.3g$ and $0.5g$, where g denotes gravity. For the frequency response analysis of the nonlinear system, simulations are performed for both up and down frequency sweep at each base acceleration amplitude over the frequency range from 10 Hz to 24 Hz. It is assumed that the beam starts from the rest and all the bistable attachments stay in the positive equilibrium positions ($\bar{w}_{aj,2} = 0.75$ cm) at the beginning of the frequency sweep as the initial conditions.

Simulated results of the transmissibility frequency response of the beam under base excitation are plotted in Fig. 2.12 for various RMS case acceleration levels and for both the frequency up-sweep and down-sweep. The shaded region in Fig. 2.12 shows the estimate of the linear locally resonant bandgap based on the theory developed for finite and continuous metastructures [5] [10] given by $\omega_t < \omega < \omega_t\sqrt{1+\mu}$ where ω_t is the target frequency of

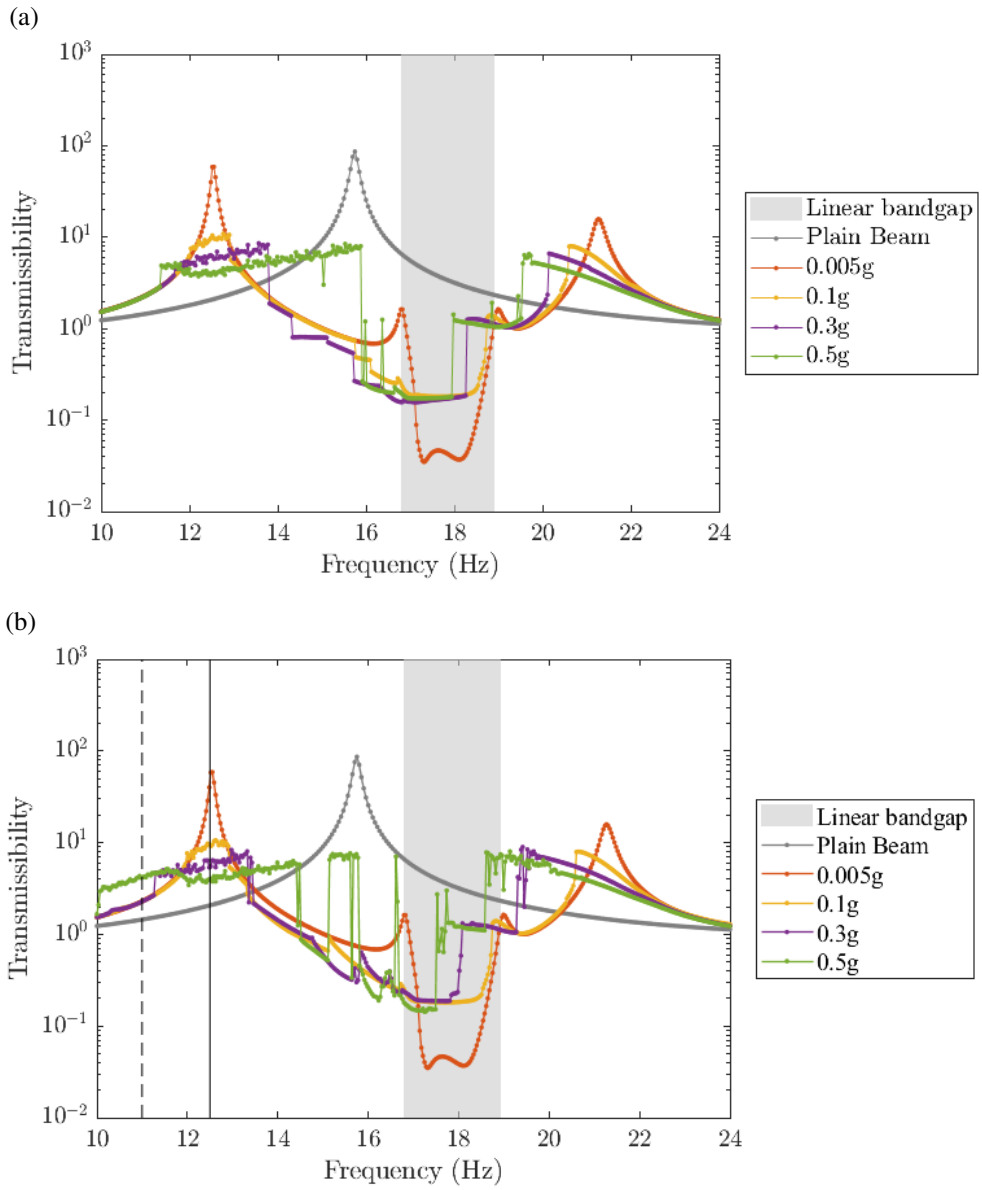

Figure 2.12: Numerical simulation results for the transmissibility of the beam under different base excitation amplitudes normalized by the base acceleration: (a) up-sweep and (b) down-sweep.

the resonators and μ is the mass ratio of the total mass of the resonators to the total mass of the plain main structure as follows:

$$\mu = \frac{\sum_{j=1}^{S} m_j}{mL} = \frac{m_r S}{\rho b h L}. \tag{2.35}$$

Here, $\omega_t = \bar{\omega}_a = 16.8$ Hz and $\mu = 0.27$ are used in the plot for the system under linear

behavior.

At very low base excitation amplitudes (e.g. $\ddot{w}_b = 0.005g$ RMS acceleration), the bistable attachments oscillate around the equilibrium positions at the linear natural frequency $\bar{\omega}_a$ and the system exhibits linear/quasilinear behavior, yielding a typical LR bandgap. The second mode of the plain bean is attenuated while additional resonances appear, which is similar to the behavior of just using linear locally resonant attachments. As the excitation level increases, nonlinear intrawell softening and interwell oscillations are enabled gradually. The first side peak around 12.5 Hz is reduced significantly and a softening behavior is seen on the second side peak, achieving a broader bandwidth of attenuation. For high acceleration levels (e.g. $\ddot{w}_b = 0.5g$ RMS acceleration), wideband chaotic behavior is observed.

Select time histories of the relative displacements of all seven attachments along with the phase portraits are presented for excitation at 12.5 Hz (marked in black line in Fig. 2.12b) under $0.1g$, $0.3g$ and $0.5g$ RMS acceleration levels in Figs. 2.13, 2.14, and 2.15 respectively. For a concise demonstration, duration of 4 s time history (from 116 s to 120 s) of the relative displacements of the attachments are plotted. While the phase portraits of the attachments are based on much longer time histories (from 100 s to 120 s) so that the dynamics behavior of individual attachments are better captured. In addition, select time instants of the relative displacement distribution of the beam and the time average responses of the beam, $w_{\mathbf{avg}}(x)$, from 116 s to 120 s are plotted. The trend is clearly shown for gradually enabled interwell oscillations (chaotic behavior) as the excitation level increases. Under $0.1g$ RMS acceleration level (Fig. 2.13), attachments 1 and 5 stay within the potential well, while the other five attachments undergo interwell chaotic vibrations. The locations of the attachment indeed affect the dynamic behavior. As seen from the select time instants of the beam's response (Fig. 2.13c), the displacements of beam at the locations of attachments 1 and 5 are relatively small compared to the responses at the locations of the other five attachments; hence, the attachments do not escape the potential well yet for the mentioned excitation

level. As the RMS acceleration level increases to $0.3g$ (Fig. 2.14) and $0.5g$ (Fig. 2.15), all the attachments begin to exhibit chaotic interwell oscillations. Higher-intensity oscillations of the bistable attachments at 12.5 Hz under $0.5g$ RMS acceleration compared to those under $0.3g$ RMS acceleration further suppress the transmissibility of the beam more as shown in Fig. 2.12.

Interestingly, high-energy periodic branch of the system is captured for $0.5g$ RMS acceleration level due to the large-orbit interwell oscillations of the bistable attachments. For example, as shown in Figs. 2.16a and b, the time histories and phase portraits of the attachments illustrate periodic interwell oscillations for $0.5g$ RMS acceleration level at 11 Hz (marked in black dash line in Fig. 2.12). Periodic responses of the beam itself are clearly shown in the select time instants and the time average responses of the beam displacement distribution in Fig. 2.16c. The response of the beam manifests itself as similar to the second mode shape of a clamped-free beam, which is the targeted mode.

2.3.2 Experimental Validation

Experimental investigations are presented next to validate the distributed-model for the LR metastructure with bistable attachments. Experimental setup shown in Fig. 2.6 has been modified slightly for shallower potential wells for the bistable attachments. The spring steel cantilever is modified to be 9.525 mm wide, 0.254 mm thick and extending the edge of the extruded slot by 4.06 cm long. In addition, the distance between the magnets, quantified by the vertical distance, d, between the lower edge of the extruded cut and the upper face of the cubic magnet, is set to be 17 mm. The post-buckled linear natural frequency is identified as 16.8 Hz. The equilibrium position of the attachment is measured to be 0.75 cm, which is approximated by the distance between the center of tip mass to the beam. The selection of this magnet spacing is to target the second mode neighborhood (around 15.9 Hz) of the plain beam in this work. The rest of the experimental setup is the same as described in detail in Section 2.2.2. The excitation frequencies are swept up from 10 Hz to 24 Hz and

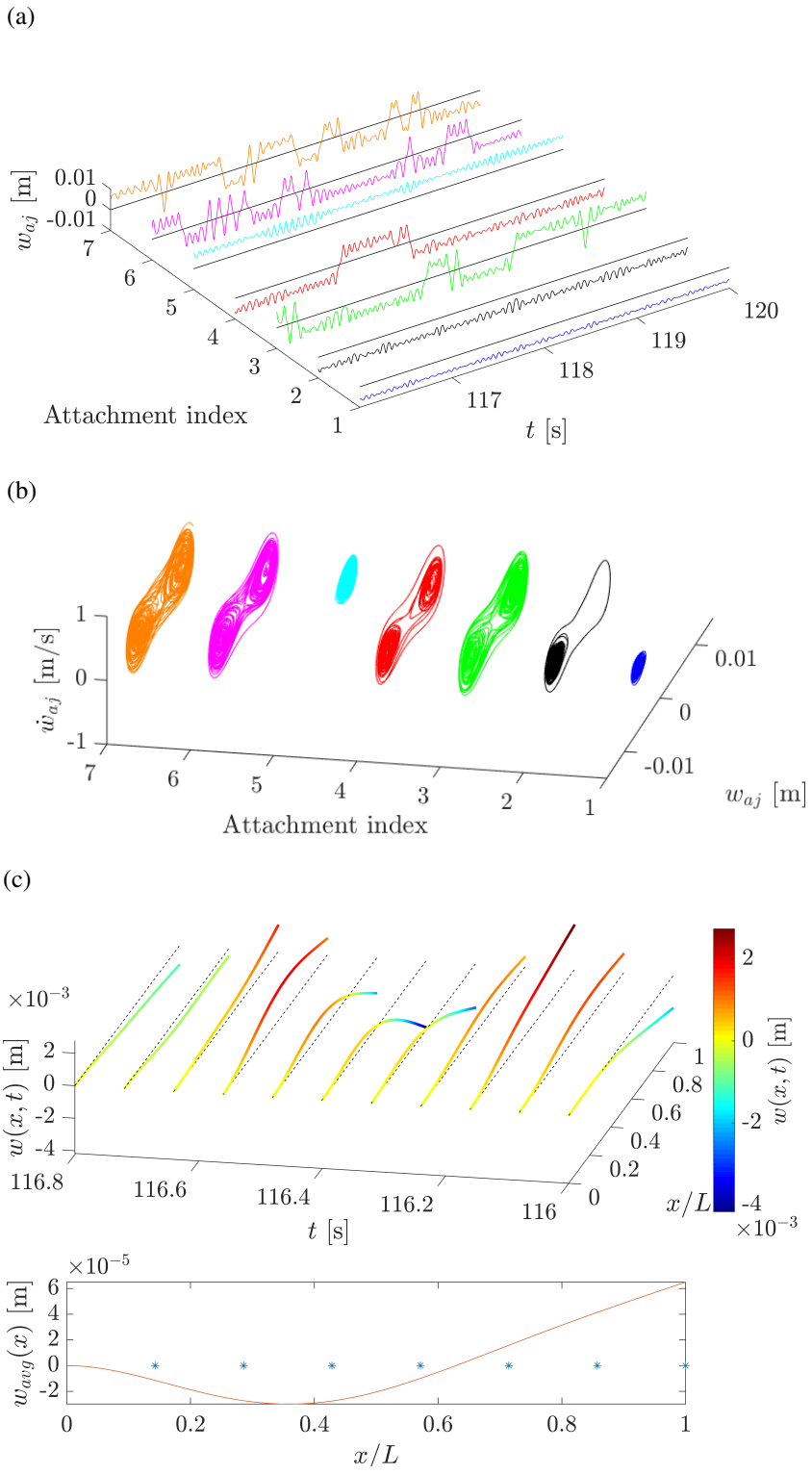

Figure 2.13: Numerical simulation results for the base acceleration of $0.1g$ at 12.5 Hz. (a) Time histories and (b) phase portraits for relative displacements of the attachments. (c) Select time history of beam displacement distribution (up) and time average displacement distribution (down). Blue asterisks mark the locations of the attachments.

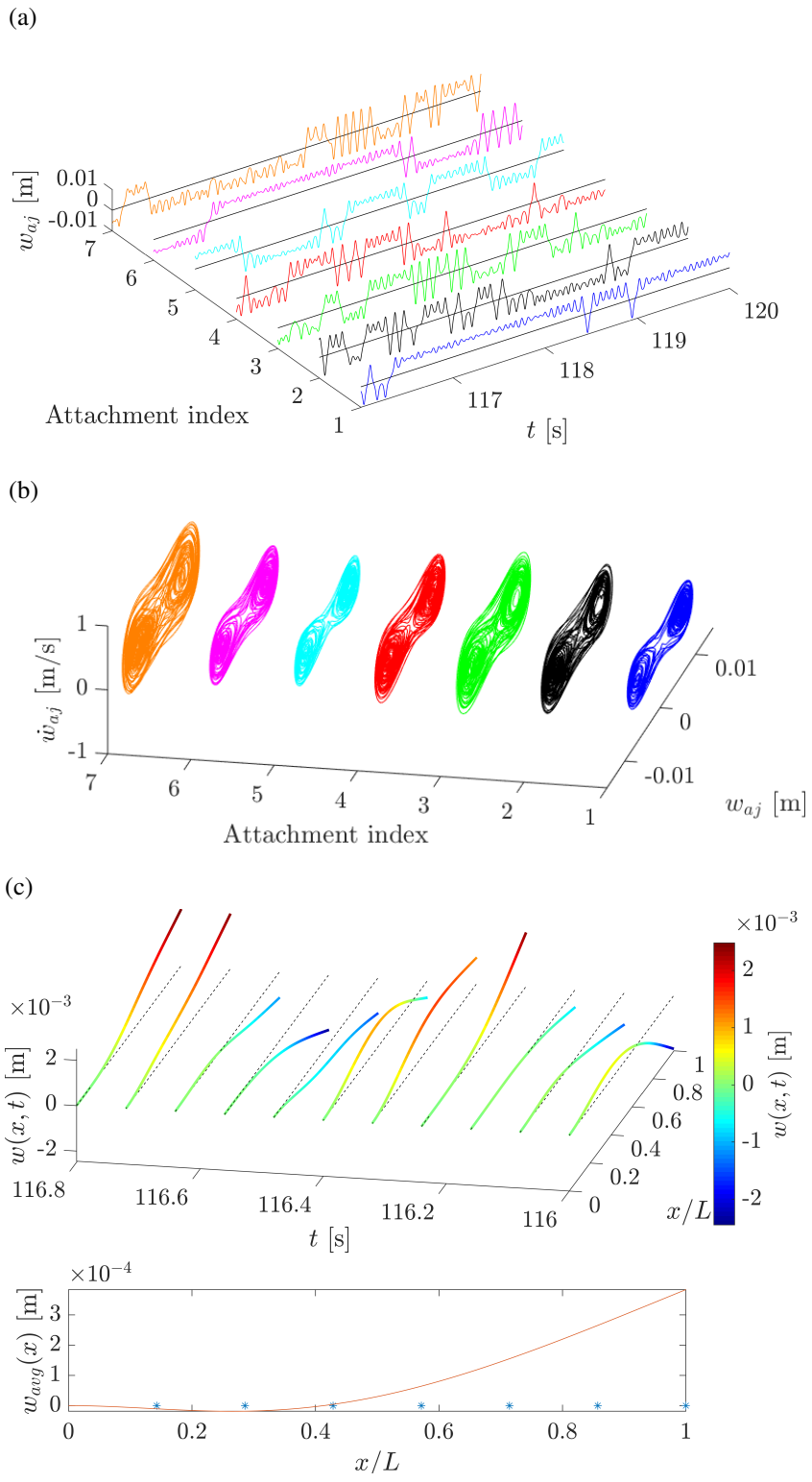

Figure 2.14: Numerical simulation results for the base acceleration of $0.3g$ at 12.5 Hz. (a) Time histories and (b) phase portraits for the relative displacements of attachments. (c) Select time history of beam displacement distribution (up) and time average displacement distribution (down). Blue asterisks mark the locations of the attachments.

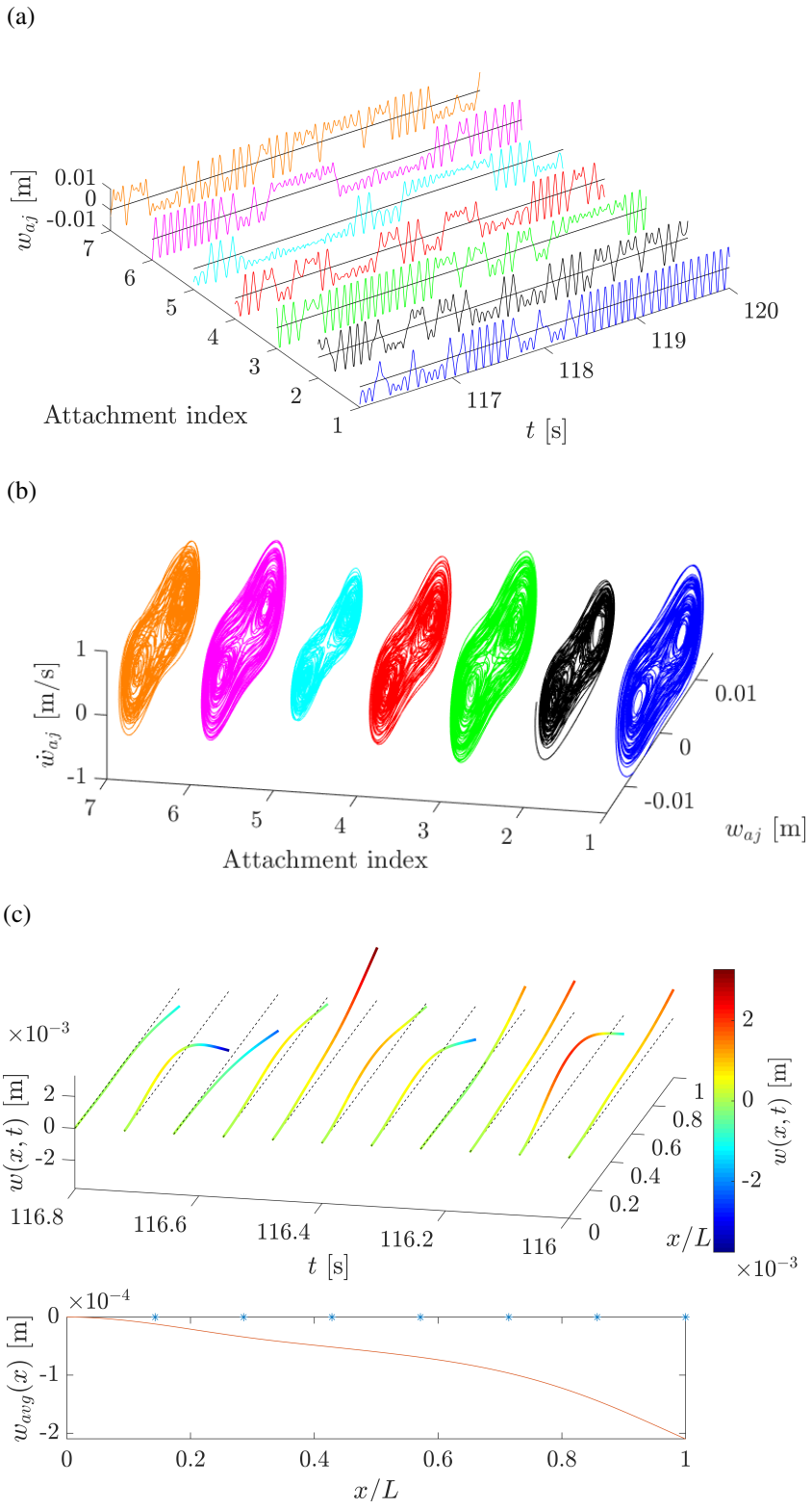

Figure 2.15: Numerical simulation results for the base acceleration of $0.5g$ at 12.5 Hz. (a) Time histories and (b) phase portraits for relative displacements of the attachments. (c) Select time history of beam displacement distribution (up) and time average displacement distribution (down). Blue asterisks mark the locations of the attachments.

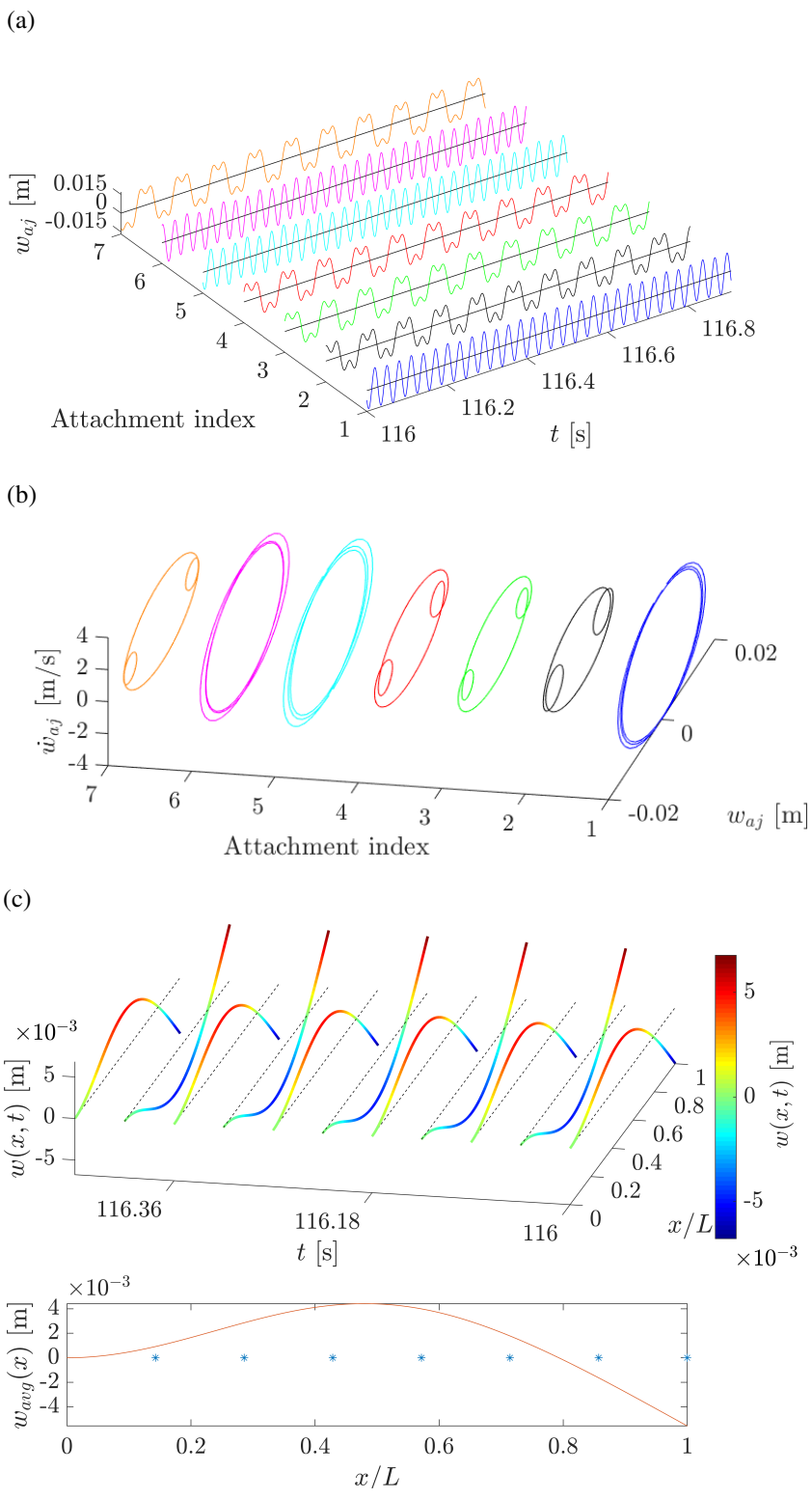

Figure 2.16: Numerical simulation results for the base acceleration of $0.5g$ at 11 Hz. (a) Time histories and (b) phase portraits for relative displacements of the attachments. (c) Select time history of beam displacement distribution (up) and time average displacement distribution (down). Blue asterisks mark the locations of the attachments.

down from 24 Hz to 10 Hz at a rate of 2.5 Hz/min for four different base acceleration levels.

Experiment is first performed on the plain beam, which is the main cantilever without the bistable attachments. All 7 magnetoelastic cantilevers with the corresponding pairs of magnets at the end are removed first, while all other pairs of magnets on the beam with $d = 17$ mm are kept. The first three modes of the plain beam are plotted in the transmissibility frequency response in Fig. 2.11. Next, the beam with all seven bistable attachments is tested. The transmissibility frequency responses of the beam are measured for various RMS base acceleration levels, as shown in Figs. 2.17a and b for up and down frequency sweeps, respectively.

It can be seen that the experimental results agree well with the responses predicted from the simulations (comparing Figs. 2.12 and 2.17). The shaded region shows the estimated linear locally resonant bandgap with the target frequency $\omega_t = 16.8$ Hz and mass ratio $\mu = 0.27$. At a very low RMS base acceleration level ($0.005g$), the metastructure has a bandgap similar to the one using linear local resonators. The second mode of the plain beam is significantly attenuated, while new resonances appear. It is observed that, at such low excitation intensity level, the bistable attachments vibrate linearly (or quasilinearly) around their respective stable equilibria, staying within the potential well as expected. As the base excitation level increases, the nonlinear attenuation is triggered first by the intrawell softening of the bistable attachments. Further increase in the base excitation intensity triggers chaotic motions of the attachments, leading to bandwidth enhancement. Overall, an attenuation frequency range that is 350% wider than the corresponding linear locally resonant bandgap is observed. A high energy branch at $0.5g$ RMS acceleration level is also observed in the experiments, especially in the down-sweep frequency response.

In general, the experimental results agree well with the numerical results based on the distributed parameter model. The small discrepancies can be caused by the following reasons. First, the slots in the beam in the experiments are not directly considered in the simulation, which assumes the beam is uniform. Secondly, the determination of the linear

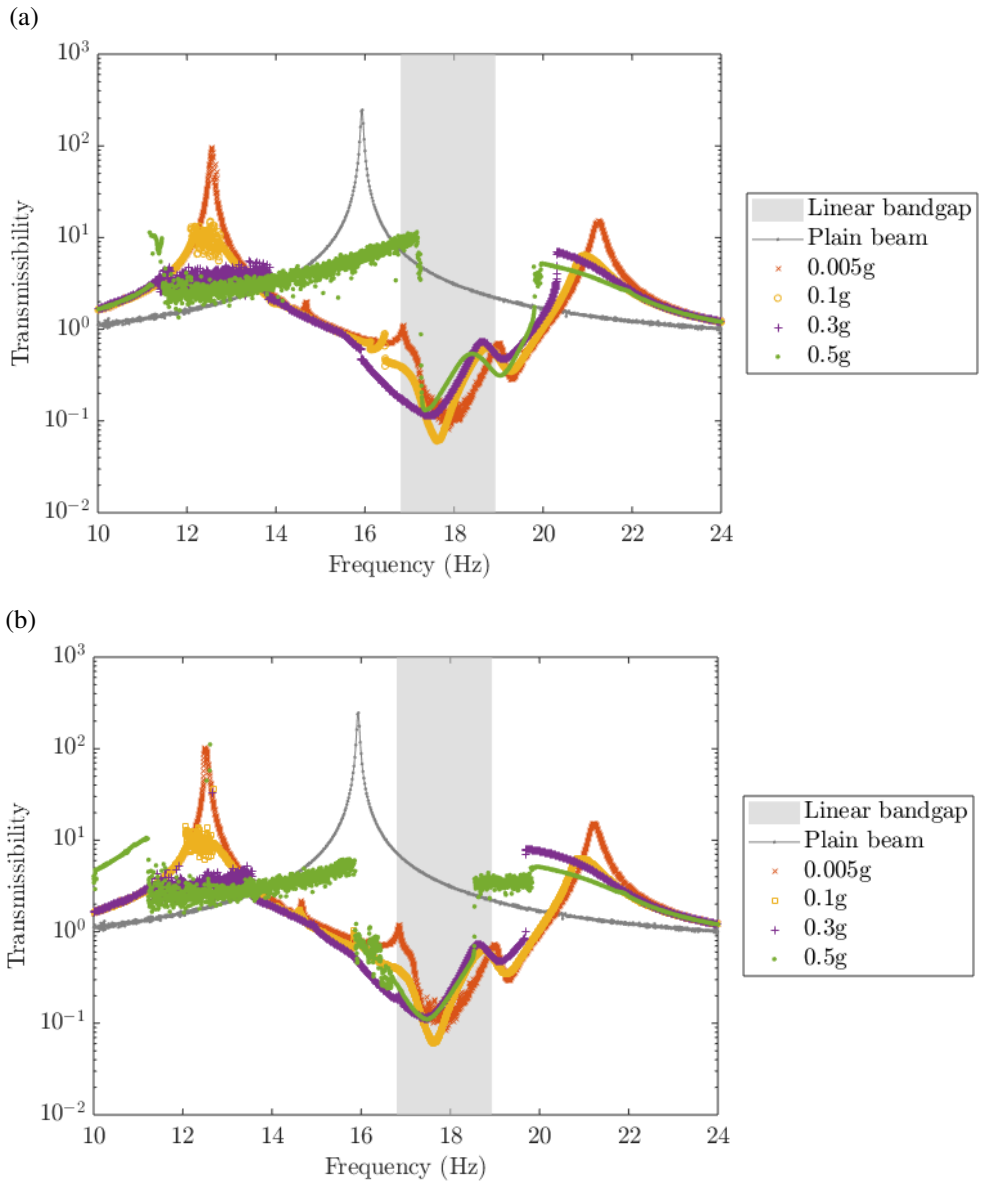

Figure 2.17: Experimental results for the transmissibility of the beam under different excitation levels normalized by the base acceleration: (a) up-sweep and (b) down-sweep.

and cubic terms of the stiffness is also simplified, obtained from the measurement of attachment's equilibrium positions and post-buckled linear natural frequencies. Thirdly, the existence of magnetic damping from the eddy currents can affect the response of the beam at large base excitation levels when the tip magnets travel though the slots on the beam. In addition, the clamping of the spring steel cantilever on the beam is asymmetric, the resulting double-well potential is not perfectly symmetric in the experiments (i.e., a small

amount of quadratic nonlinearity is inevitable). The effect of significantly asymmetric potential wells can be found in the nonlinear energy harvesting literature [83, 84]). Furthermore, small variations in manually adjusted magnet spacing are inevitable and can lead to slightly different post-buckled linear natural frequencies for the bistable attachments.

2.4 Conclusions

In this chapter, the dynamics of mechanical locally resonant metastructures with bistable attachments are investigated. Both lumped parameter and distributed parameter nonlinear models are developed. The amplitude-dependent enhancement of the frequency bandwidth is observed numerically and validated experimentally. The bandwidth offered by nonlinear interwell oscillations of bistable attachments is substantially wider than the corresponding linear locally resonant bandgap. Such nonlinear vibrations can be triggered with increased excitation amplitude or by designing the potential wells to be shallow enough to ensure interwell dynamics for a given excitation level. This class of nonlinear metastructures provides much wider bandwidths than their linear counterparts whose bandgap is known to be limited by the added mass ratio.

CHAPTER 3
MECHANICAL LOCALLY RESONANT METASTRUCTURES WITH QUASIPERIODIC RESONATORS

3.1 Introduction

This chapter returns to linear locally resonant metamaterials and metastructures and explores aperiodicity, specifically by disturbing the locations or the natural frequencies of the resonators according to a quasiperiodic pattern. The dynamic behavior and topology of quasiperiodic resonant metastructures are investigated. Analyses show that the quasiperiodic arrangement of resonators introduces frequency bandgaps in addition to the LR bandgap. The concept is illustrated on a beam in transverse motion with an array of mechanical resonators. Numerical studies evaluate the frequency spectra as a function of a free quasiperiodic parameter which defines arrangement of resonators, revealing a structure reminiscent of a Hofstadter butterfly. The study of key topological properties are followed by exploring the integrated density of states. Results illustrate the occurrence of additional bandgaps that are topologically non-trivial and that host edge-localized modes in finite structures. Mode transitions by varying the quasiperiodic parameter or additional phase modulation parameter are demonstrated. In addition, experimental validations are performed on a cantilever beam carrying an array of 30 resonators.

3.2 Quasiperiodic Pattern Generation: Varying Locations

This section introduces a quasiperiodic (QP) pattern to the LR metastructures. The systems that are considered here contain elastic beams in transverse motion equipped with resonators placed at locations defined by the projection operation described in [60]. This pattern-generating procedure identifies families of structures ranging from periodic to QP

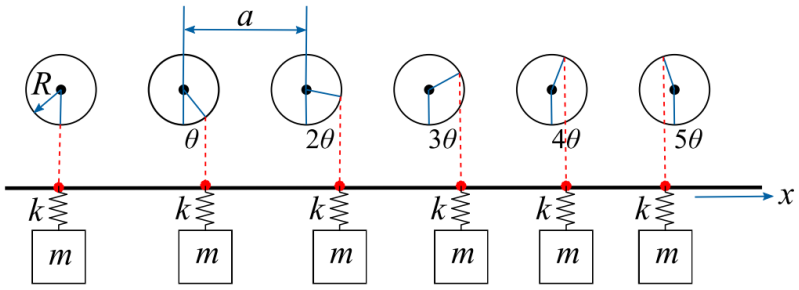

Figure 3.1: Projection operation for placement of the local resonators on a beam according to the procedure described in [60].

obtained through smooth variation of the parameters defining the projection, which can be interpreted geometrically as shown in Fig. 3.1. Accordingly, the location of resonator s is given by:

$$x_s = sa + R\sin(2\pi s\theta). \tag{3.1}$$

Here, a is the distance between the centers of adjacent circles defining the spacing between resonators in an underlying periodic arrangement, while the radius of the circle R and the angular increment θ define the projection. In addition, all resonators are assumed to be identical with the same mass m and stiffness k. The governing equations for the beam and the s-th resonator are:

$$D\frac{\partial^4 w(x,t)}{\partial x^4} + \rho A\frac{\partial^2 w(x,t)}{\partial t^2} - k\sum_s w_s(t)\delta(x - x_s) = 0, \tag{3.2}$$

$$m\frac{\partial^2 (w(x_s,t) + w_s(t))}{\partial t^2} + kw_s(t) = 0, \quad s = 1,\ldots,S \tag{3.3}$$

where $w(x,t)$ is the transverse displacement of the beam at location x and time t, and $w_s(t)$ is the displacement of the s-th resonator relative to the beam at location x_s. Also, $D = EI$ is the beam bending stiffness, where E is the Young's modulus, and I is the second moment of area of the beam cross section, while ρ is the mass density and A is the cross-sectional area. In addition, δ is the Dirac delta function.

An aluminum beam (mass density $\rho = 2700$ kg/m^3, Young's modulus $E = 69$ GPa) of cross section 0.8×25.2 mm^2 is considered for all the numerical analyses. All resonators have the same natural frequency of 90 Hz, and an added mass ratio with respect to the beam of 1.26. Additionally, $a = 5.08$ cm and $R = 0.3a$ are chosen as fixed dimensions in accordance with the considered experimental setup described later in Section 3.2.3.

3.2.1 Non-trivial Topological Bandgaps and Edge-localized States

In this part, the study in terms of variations in θ, which is the considered free QP parameter, is conducted. Bulk frequency spectra for infinite beams and the frequency spectra for finite beams with various boundary conditions are compared. Edge-localized modes of finite beams and topological properties of the frequency bands are investigated.

Bulk and Finite Spectra

The spectrum of an infinite beam is evaluated approximately by considering a large structure (i.e., 600 cells) with periodic boundary conditions imposed on both ends so that it geometrically resembles a ring structure [63]. Via an analysis approach based on Galerkin's approximation, the natural frequencies of the large structure can be estimated from the discretized eigenvalue problem.

For rational θ values that are commensurate with 600, all the natural frequencies of the ring structure would lie on the bulk band of the underlying infinite domain. Figure 3.2 plots the frequencies for the first 1200 modes of the structure with uniformly-placed resonators ($\theta = 0$). As expected, LR bandgap appears and separates the first 600 natural frequencies (first band) from the rest. As θ increases from 0, bulk frequency bands are divided into more bands separated by additional frequency bandgaps, which form the typical fractal structure of QP media [64]. The illustration of band splitting is shown in Fig. 3.3, which focuses on the first 600 natural frequencies of the structure below the LR bandgap. For $\theta = 1/3$, two bandgaps appear, separating the 600 modes into 3 bands; while for $\theta = 1/4$, three

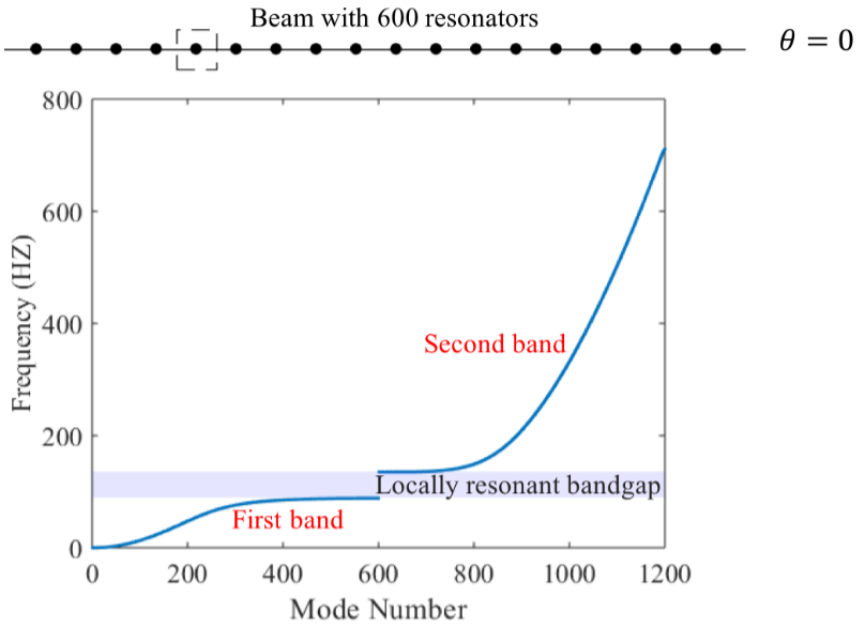

Figure 3.2: Natural frequencies of a large ring structure (beam with uniformly-placed 600 resonators under periodic boundary condition).

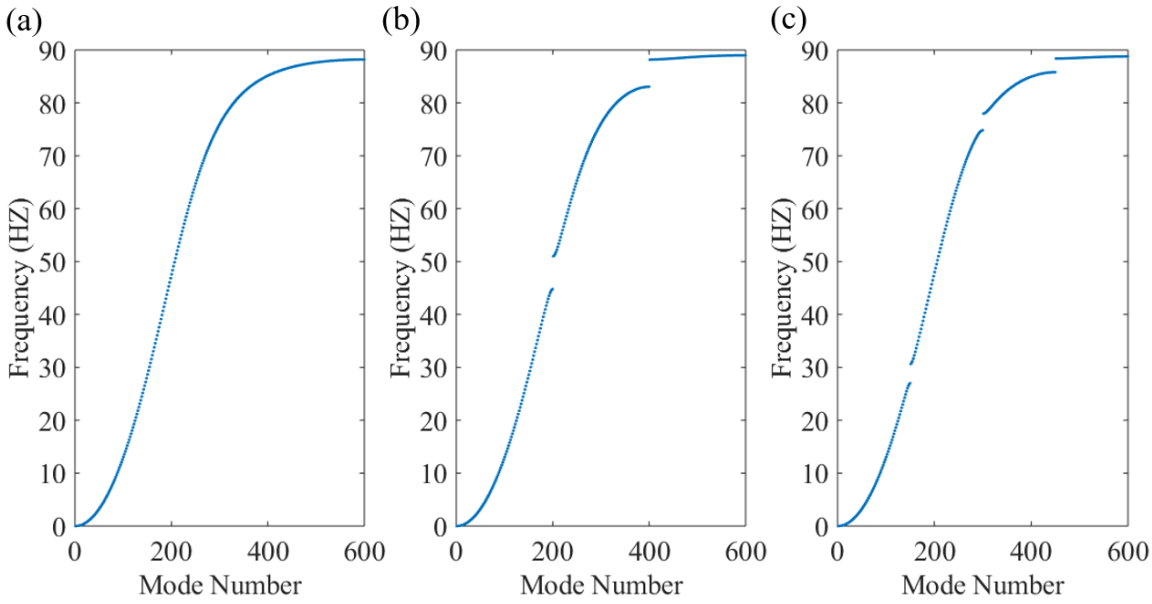

Figure 3.3: Illustration of band splitting (focusing on the first 600 modes) as θ changes: (a) $\theta = 0$, (b) $\theta = 1/3$, and (c) $\theta = 1/4$.

bandgaps emerge, dividing the 600 modes into 4 bands. Generally, for a rational $\theta = p/q$ (p and q are coprime), the first S modes are expected to be distributed among q bands with at most $q - 1$ bandgaps.

By considering all rational values of θ that are commensurate with 600 cells, the natural frequencies of all configurations are obtained and plotted together to get the approximated bulk spectrum shown in black in Fig. 3.4. The black region specifies the frequency ranges populated by the bulk eigenvalues, while the left white regions identify bandgaps where no eigenstates exist. Variation of vibrational frequencies in terms of QP parameter, θ, leads to a pattern that is reminiscent the Hofstadter butterfly [64].

Next, the spectrum of finite QP beams is examined. A beam of 30 unit cells is considered, with simply-supported boundary condition on both ends, i.e., subjected to $w(x = 0, L) = 0$ and $w_{xx}(x = 0, L) = 0$. Again, the Galerkin's approximation is used for obtaining the eigenfrequencies of the finite structure, which are plotted in red in Fig. 3.4.

Edge-localized Modes

Both bulk and finite spectra are characterized by a LR bandgap that remains unaltered as θ varies. This gap separates two spectral regions, which feature several additional bandgaps whose center frequencies depend on the value of θ. These gaps are crossed by several modes of the finite structure, whose distinctive feature is their localized nature. The zoomed-in spectrum in Fig. 3.5 compares selected modes corresponding respectively to bulk and finite structure frequencies. Notably, the modes in the finite beam that appear in the bandgap are edge-localized. Also, the response of the resonators (shown in red circles) is of a localized nature when the beam's deflection is localized, while the relative displacements of the resonators are in phase and out of phase with respect to the beam at frequencies below and above the LR bandgap, respectively.

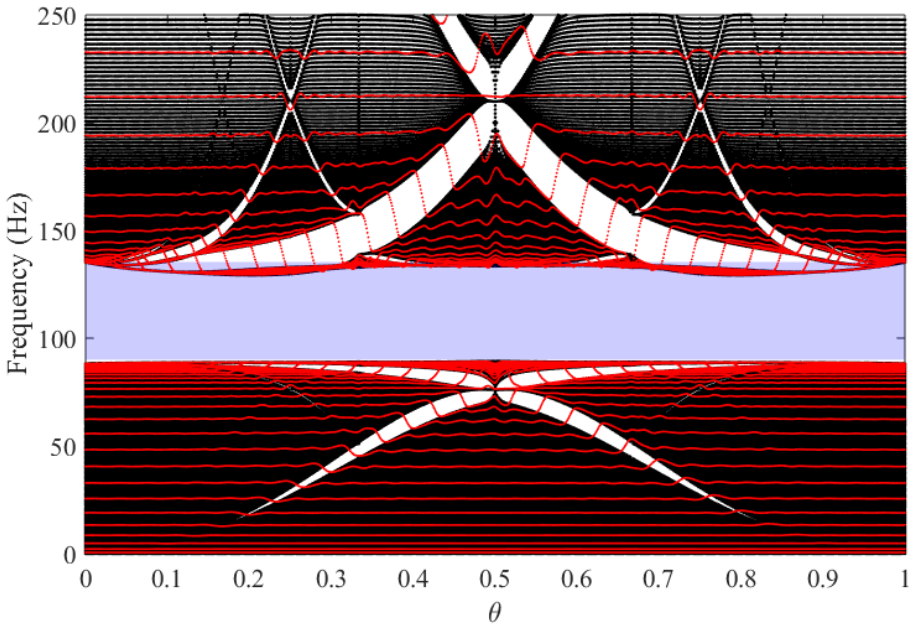

Figure 3.4: Bulk (black) and finite beam (red) spectra as a function of θ. The finite beam spectrum, obtained for a finite, simply supported beam with 30 cells, shows the presence of modes spanning the non-trivial gaps. The blue shaded area highlights the LR bandgap, which is estimated according to the formula derived in [10].

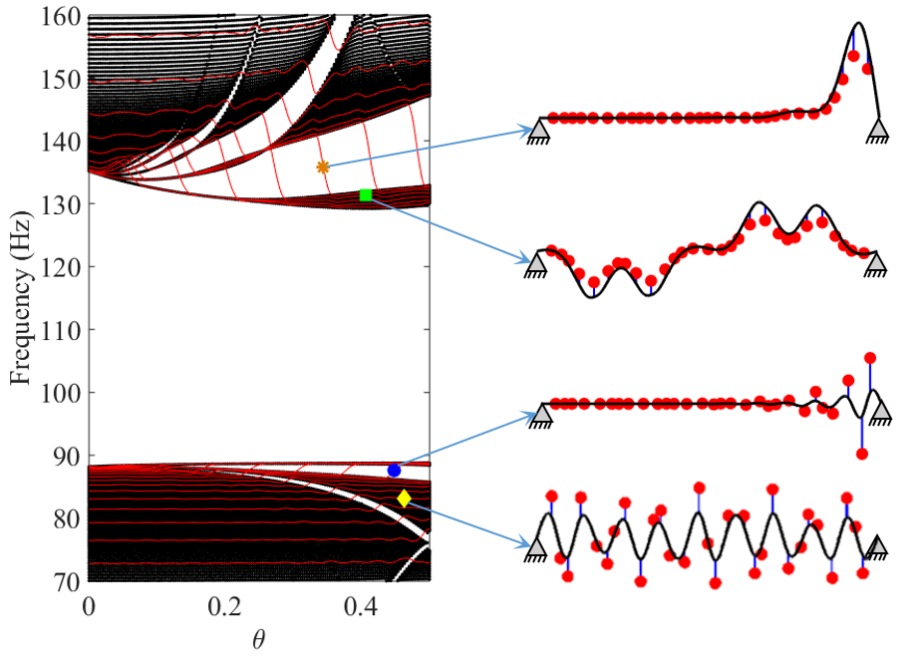

Figure 3.5: Detail of the spectrum showing four frequencies and the corresponding bulk and edge-localized modes. The black curve represents the deflection of the beam, while the red circles denote the displacements of the resonators.

Topological Properties of the Bands

Splitting of the bulk bands, as illustrated in Fig. 3.3, corresponds to the change in density of states. The existence of edge states can be predicted through the analysis of the topological properties of the bands, which are conveniently uncovered by estimating the integrated density of states (IDS) for the system [60, 63]. The IDS at frequency Ω is defined as:

$$IDS(\Omega) = \lim_{S\to\infty} \frac{\sum_n [\omega_n \leq \Omega]}{S}, \tag{3.4}$$

where $[\cdot]$ denotes the Iverson bracket, converting the logical proposition into number 1 if the statement is true. Non-trivial gaps and the resulting onset of edge states spanning them are associated to changes in the IDS as θ varies. Figure 3.6 displays the IDS as a function of θ, which corresponds to the bulk spectrum shown in Fig. 3.4. The colormap represents the frequency Ω in Eq. 3.4, and the rendering highlights the sharp changes of the color, indicating the jumps of frequency inside the bandgaps in the IDS. All the frequencies Ω inside a bandgap have the same IDS value. In the IDS representation of Fig. 3.6, a bandgap appears as a line, whose slope m indicates the number of topological boundary modes that span the bandgap in the interval between two subsequent commensurate values of θ [63]. In this case, three IDS lines corresponding to the three topological bandgaps (labeled in Fig. 3.7) are shown as white dashed lines in Fig. 3.6, whereby $m = 1, 2, 3$ respectively is the slope of the corresponding gaps. The red dashed IDS line related to the LR bandgap has a slope of $m = 0$, which indicates its topologically trivial nature and the lack of associated edge states spanning the gap (see Fig. 3.4). Another way to identify the LR bandgap as topologically trivial is to compare the spectra of finite beam with different boundary conditions as shown in Fig. 3.8. LR bandgap hosts defect modes depending on the boundary conditions of the finite structure (i.e., free-free and clamped-free boundaries); while additional topologically non-trivial bandgaps hold localized modes regardless of the boundary conditions of the finite structure.

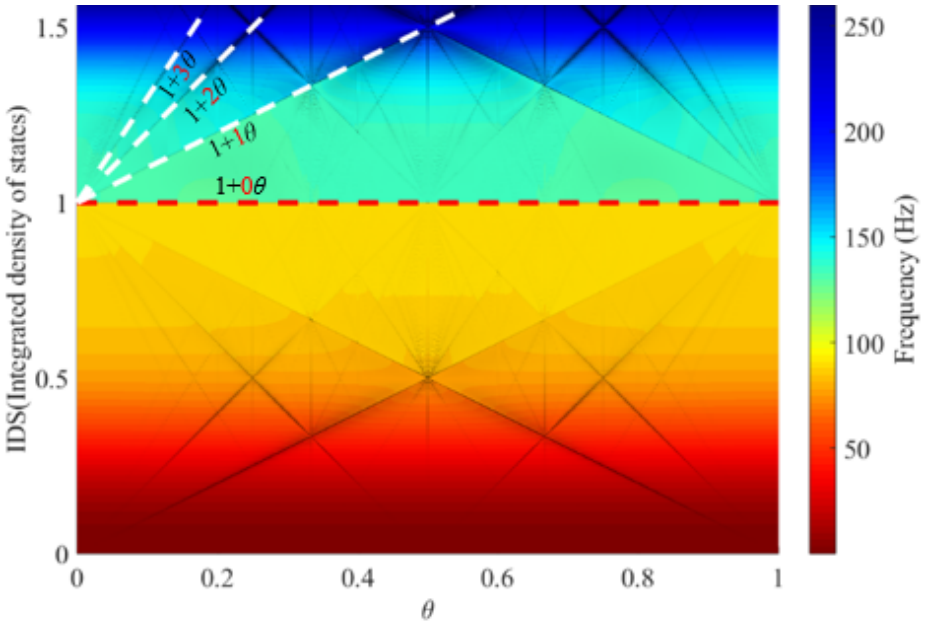

Figure 3.6: IDS as a function of θ exhibits sharp linear jumps at the bandgaps. The colormap indicates the frequency Ω. The slope of three of these lines (highlighted by the white dashed lines, and corresponding to the three gaps labeled in Fig. 3.7), is equal to $m = 1-3$, while for the LR bandgap (highlighted by the red dashed line) is $m = 0$, which indicates that this band is topologically trivial.

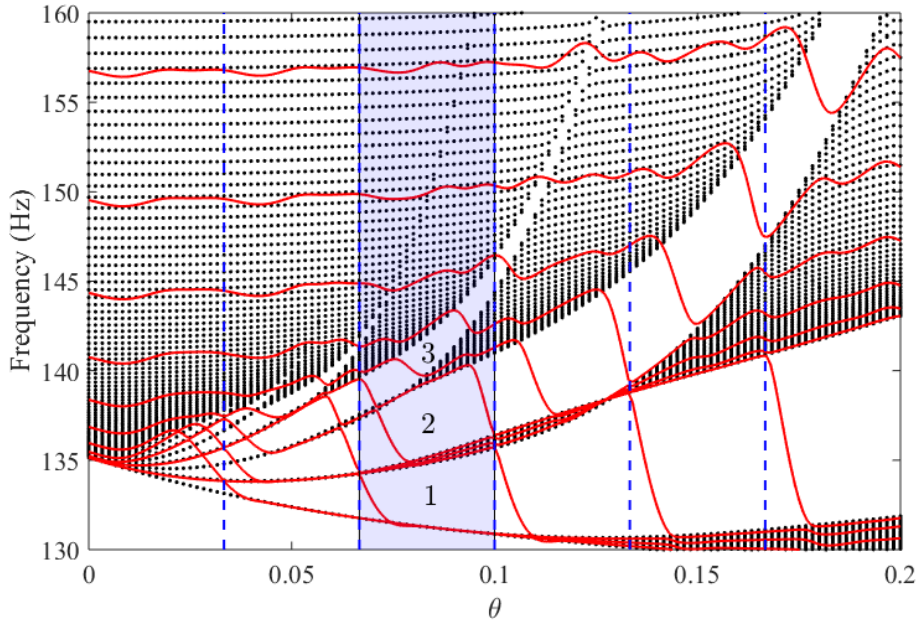

Figure 3.7: Detail of spectrum showing three labeled non-trivial topological bandgaps with increasing number of topological modes (blue dashed lines separate regions between commensurate values of θ, while the blue shaded area highlights the region between $\theta = 2/30$ and $\theta = 3/30$).

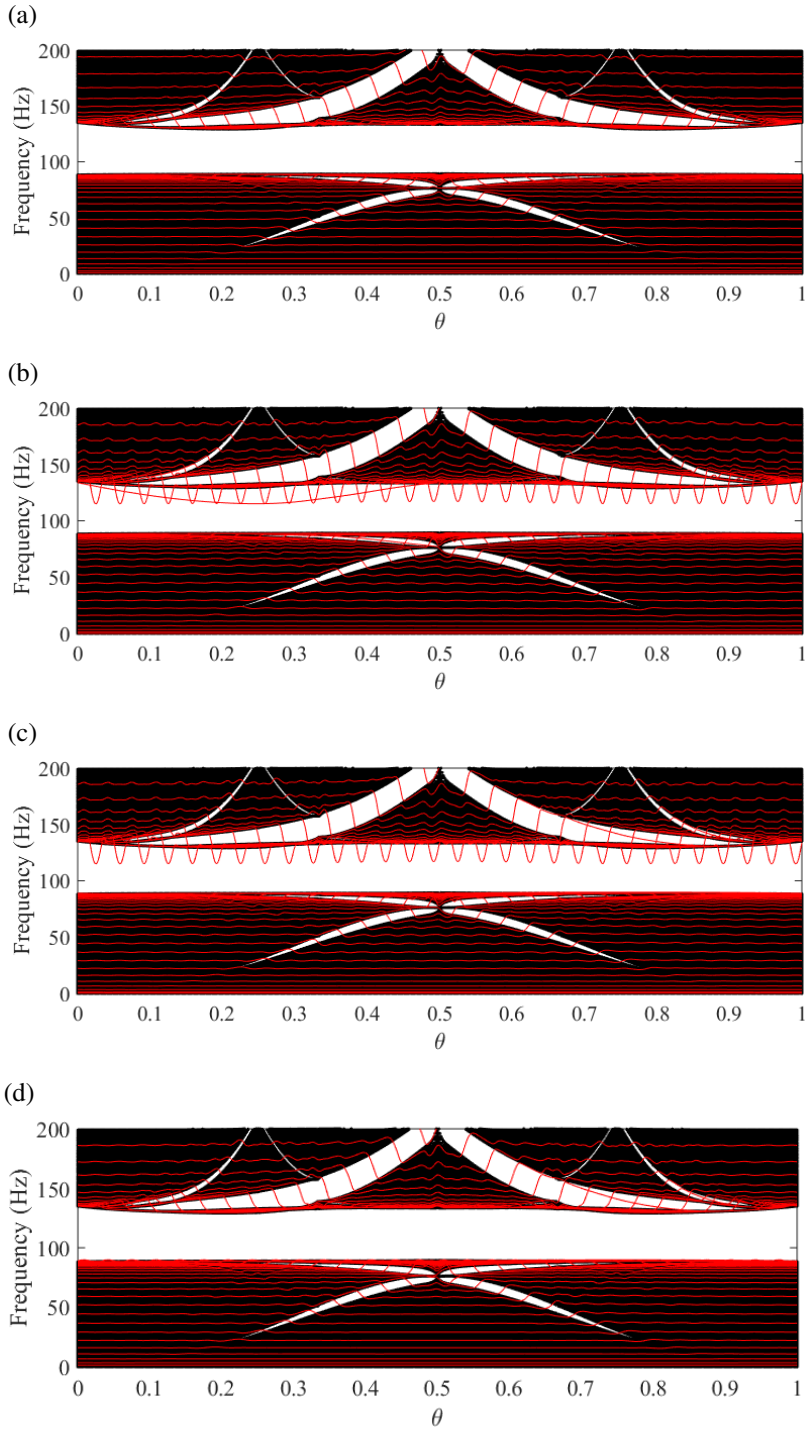

Figure 3.8: Comparison between the finite beam spectra as a function of θ for different boundary conditions: (a) simply supported-simply supported, (b) free-free, (c) clamped-free, and (d) clamped-clamped.

3.2.2 Numerical Analyses on a Clamped-free Cantilever beam

The finite system is implemented as a cantilever beam with clamped-free boundary conditions, with excitation applied at the free end. Numerical analyses (Fig. 3.9) are performed to evaluate the presence of the LR bandgap and of additional non-trivial bandgaps, and to guide the selection of θ values for experimental investigation. The equation of motion for the beam is slightly modified from Eq. 3.2 as:

$$D\frac{\partial^4 w(x,t)}{\partial x^4} + \rho A\frac{\partial^2 w(x,t)}{\partial t^2} - k\sum_s w_s(t)\delta(x-x_s) = f(L,t). \tag{3.5}$$

By using an assumed-modes type expansion with N modes, the transverse displacement of the beam is expanded as:

$$w(x,t) = \sum_{r=1}^{N} \phi_r(x)\eta_r(t), \tag{3.6}$$

where $\eta_r(t)$ are the modal weightings to be obtained, while $\phi_r(x)$ are the mass-normalized mode shapes of the beam obtained for specific boundary conditions (subjected to clamped-free boundary conditions as shown in Eq. 2.14). On the finite structure, bandgaps are conveniently visualized by evaluating the frequency response function for the beam, averaged over portions of the length. For example, Fig. 3.9b shows frequency response, corresponding to the ratio of magnitude of beam transverse deflection (output) to magnitude of forcing (input). The beam response is averaged between 20-30% of the span from the clamped end, which is sufficiently far from the excitation location, and not too close to the clamped boundary. As a result, the colormap in Fig. 3.9b is characterized by low response regions (in blue) that highlight the attenuation occurring in the bandgaps. This representation clearly outlines both the LR bandgap and the additional topological gaps as θ varies. In contrast, Fig. 3.9c, obtained by averaging the beams response near the free end (i.e., between 90-100% of the span), clearly highlights the modes of the finite systems, including the resonances localized in the gaps associated with the finite system. Of these

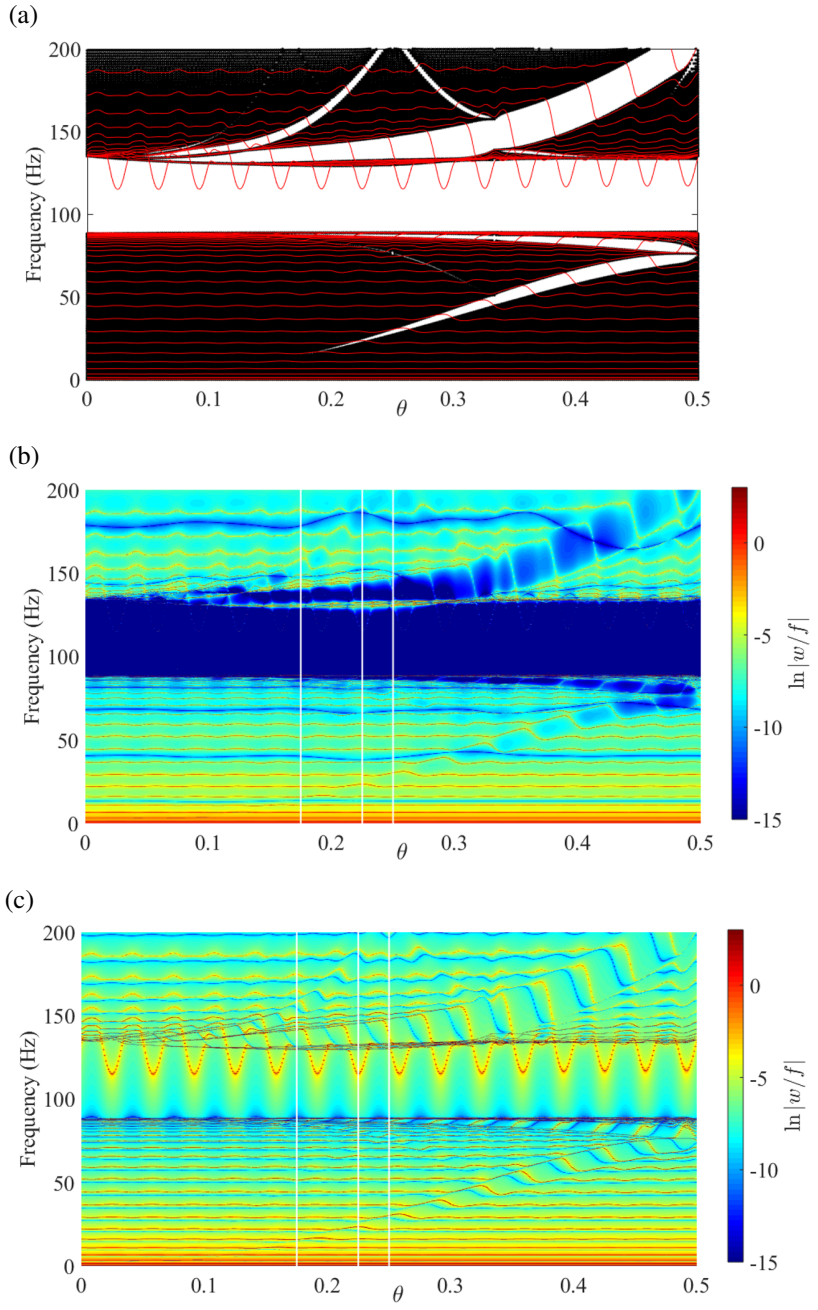

Figure 3.9: (a) Bulk (black) and finite spectra for a clamped-free beam with 30 resonators (red). (b) Numerical frequency response of the beam spatially averaged between 20% and 30% of the beam span: the colormap evolving from blue to red corresponds to the log scale of the magnitude. The blue regions highlight the low response ranges corresponding to the bandgaps. (c) Numerical frequency response of the beam spatially averaged between 90% and 100% of the beam span: the response near the beam tip highlights the presence of resonances within the gaps which correspond to edge states. Vertical white lines in (b,c) correspond to the values of $\theta = 0.175$, $\theta = 0.225$ and $\theta = 0.25$ considered in the experiments.

modes, those in the LR gap are not topological, and solely depend on the considered types of boundary conditions. The non-trivial additional gaps are instead spanned by topologically non-trivial resonant modes as θ varies.

3.2.3 Experimental Validation

For the experiments, $\theta = 0.175$, $\theta = 0.225$ and $\theta = 0.25$ are selected to ensure a well defined separation between the modes associated with the LR bandgap and the additional bandgap above. The selected three cases are highlighted in white lines in Fig. 3.9b and Fig. 3.9c for reference. The experimental investigations are presented to confirm the existence of the topologically non-trivial bandgaps and the occurrence of edge-localized modes.

Experimental Setup

The finite system is physically implemented by employing a 1.524 m long aluminum cantilever beam with 30 resonators (Fig. 3.10). Each resonator consists of a 8.26 cm long strip of spring steel, which is 0.5 mm thick and 6.35 mm wide. Each strip is clamped symmetrically along the beam, thus forming two identical cantilevers. Two 6.35 mm^3 permanent magnets are placed at the tip of each cantilever, to add a tip mass of 3.6 g. The resulting natural frequency of each resonator is measured to be around 90 Hz. The beam is clamped vertically on one end, and is excited by an electrodynamic shaker at the free end (Fig. 3.10c). The force applied by the shaker is measured by a force transducer, while the beam's velocity field is mapped by a scanning laser Doppler vibrometer (SLDV) over a grid of 158 points along the beam length, which corresponds to a spatial resolution of 9.65 mm.

Experimental Results

Figure 3.11 shows the experimental frequency response averaged between 20% and 30% of the beam span, i.e., away from the excitation location. The LR bandgap is clearly observed

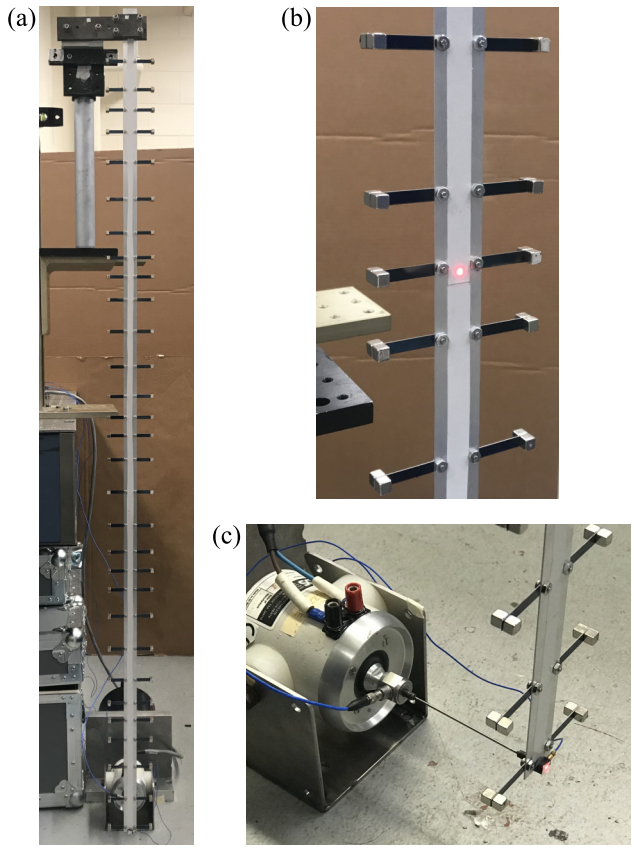

Figure 3.10: Experimental setup for the mechanical QP metastructure: a cantilever beam with 30 identical resonators that are located quasiperiodically. (a) Front view of the beam, (b) close-up of the resonators, and (c) view of the tip of the beam, excited by a electrodynamics shaker.

for $\theta = 0$, which is the case of the beam with uniformly-placed resonators; and it remains the same for the other three θ values. The topological bandgap is noticed to appear when the locations of the resonators are non-uniform ($\theta = 0.175$, 0.225, and 0.25). Overall, the center frequency location and frequency width of these bands agree well with the theoretical predictions of the LR and the non-trivial bandgaps, which are highlighted in blue and green shaded areas, respectively. Both center frequency and width of the topological bandgap increase as the QP patter parameter θ varies from 0.175 to 0.25.

Furthermore, the presence of the localized modes is found for both $\theta = 0.175$ and $\theta = 0.25$. Experimental frequency response of the beam and measured spatial distributions of selected deflection shapes are shown in Figs. 3.12b-d for $\theta = 0.175$ and in Figs. 3.13b-d

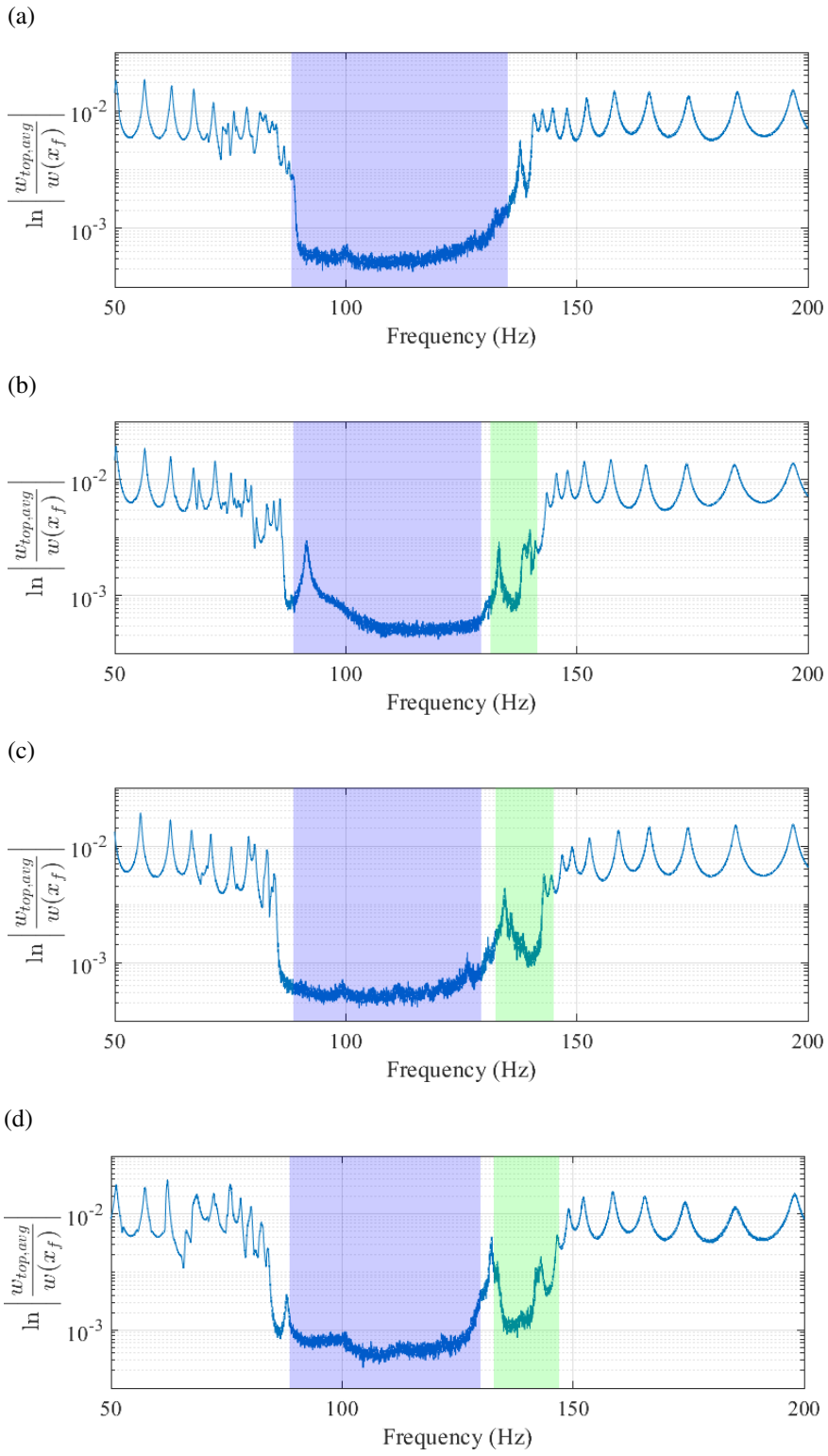

Figure 3.11: Experimental results of the beam frequency response (spatially averaged between 20% and 30% of beam span) for selected θ values: (a) $\theta = 0$, (b) $\theta = 0.175$, (c) $\theta = 0.225$, and (d) $\theta = 0.25$. Green and blue shaded regions highlight the theoretical LR and topologically non-trivial bandgaps, respectively.

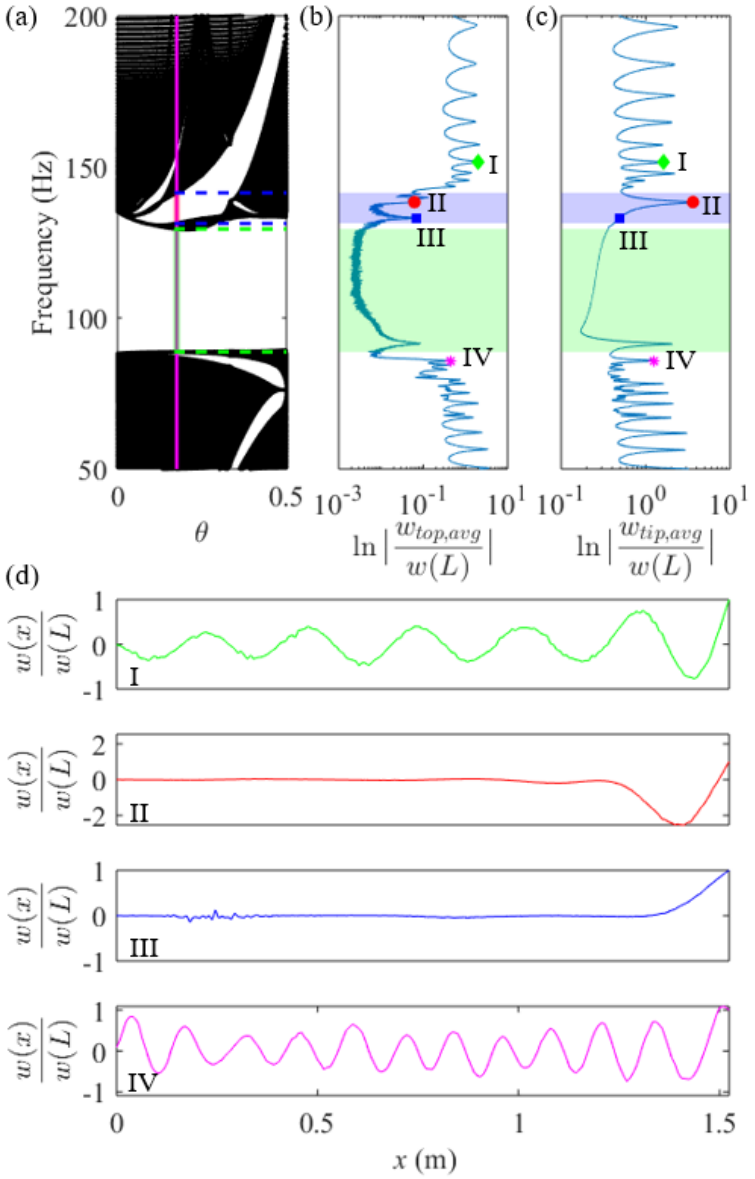

Figure 3.12: (a) Detail of numerical bulk spectrum with vertical magenta lines corresponding to $\theta = 0.175$. The green and blue dash lines show the theoretical boundaries of the LR and non-trivial topological bandgaps respectively. (b-d) Experimental results for $\theta = 0.175$. Magnitude of beam frequency response spatially averaged between 20% and 30% (b), 90% and 100% (c) of beam span. Green and blue shaded areas highlight the theoretical LR and topological bandgaps. (d) Measured deflection shapes of the beam. Modes 'I', 'III' and 'IV' are bulk modes at frequencies respectively before the LR gap, between the LR and topological bandgaps, and after the topological bandgap. The corresponding frequencies are marked by the green diamond, blue square and magenta asterisk in (b,c). The mode labeled as 'II' in (d) is edge-localized, and its frequency falls in the topologically non-trivial gap, and it is marked by red circle in (c).

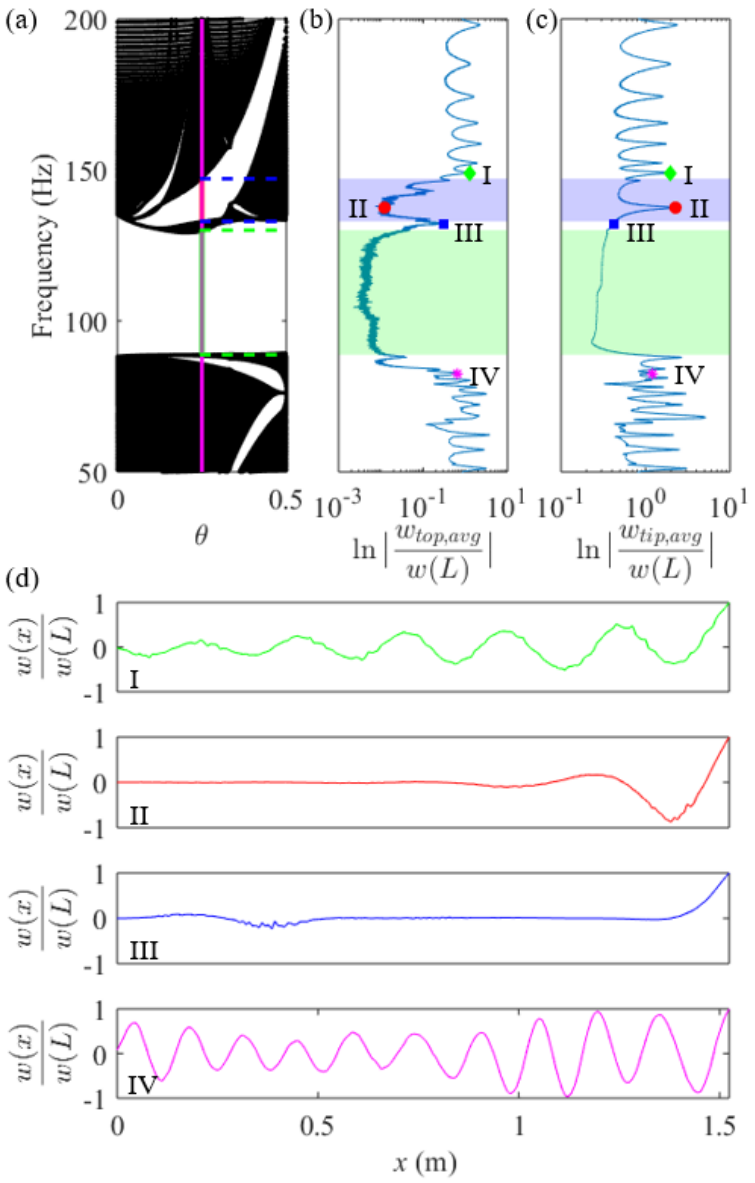

Figure 3.13: (a) Detail of numerical bulk spectrum with vertical magenta lines corresponding to $\theta = 0.25$. The green and blue dash lines show the theoretical boundaries of the LR and non-trivial topological bandgaps respectively. (b-d) Experimental results for $\theta = 0.25$. Magnitude of beam frequency response spatially averaged between 20% and 30% (b), 90% and 100% (c) of beam span. Green and blue shaded areas highlight the theoretical LR and topological bandgaps. (d) Measured deflection shapes of the beam. Modes 'I', 'III' and 'IV' are bulk modes at frequencies respectively before the LR gap, between the LR and topological bandgaps, and after the topological bandgap. The corresponding frequencies are marked by the green diamond, blue square and magenta asterisk in (b,c). The mode labeled as 'II' in (d) is edge-localized, and its frequency falls in the topologically non-trivial gap, and it is marked by red circle in (c).

for $\theta = 0.25$. The measured frequency response average near the free end (i.e., between 90% and 100% of the beam span) shows the presence of the localized modes which correspond to response peaks within the gaps highlighted in Figs. 3.12c and 3.13c. As expected from theoretical predictions, the measured localized modes (red circle) for each case appear within the topological bandgaps, and their localized nature at the edge are well confirmed by the corresponding deflection shapes plotted in red, and labeled 'II' in Figs. 3.12d and 3.13d. In addition, for each θ value considered, 3 bulk, non-localized modes are also presented to illustrate their global deflection patterns. These modes are labeled 'I', 'III' and 'IV' in the figure, and their corresponding frequencies are part of the bulk spectrum, specifically including the frequency range separating the LR and the topological bandgaps (green diamond).

3.3 Quasiperiodic Pattern Generation: Varying Natural Frequencies

This section introduces another way to apply the QP pattern to the LR metastructures, which contain elastic beams in transverse motion equipped with uniformly-located resonators with various natural frequencies as shown in Fig. 3.14. Accordingly, the natural frequencies of s-th resonator ω_s is given by:

$$\omega_s = \sqrt{\frac{k_s}{m_s}} = \omega_0[1 + \alpha \sin(2\pi s\theta)], \tag{3.7}$$

where ω_0 is the natural frequency of the resonators in an underlying periodic arrangement, α is a ratio that quantifies the maximum frequency variation from ω_0 (modulation level), and θ is still the angular increment. Figure 3.14b plots the natural frequencies as a function of resonator index s with three representative θ values: $\theta = 0$ for the uniform case, rational $\theta = 2/5$ for periodic cases, and irrational $\theta = 1/\sqrt{3}$ for aperiodic cases.

Resonators are placed uniformly on the beam with distance a between the adjacent ones. In addition, all the resonators are assumed to have the same mass $m_s = m$, then the

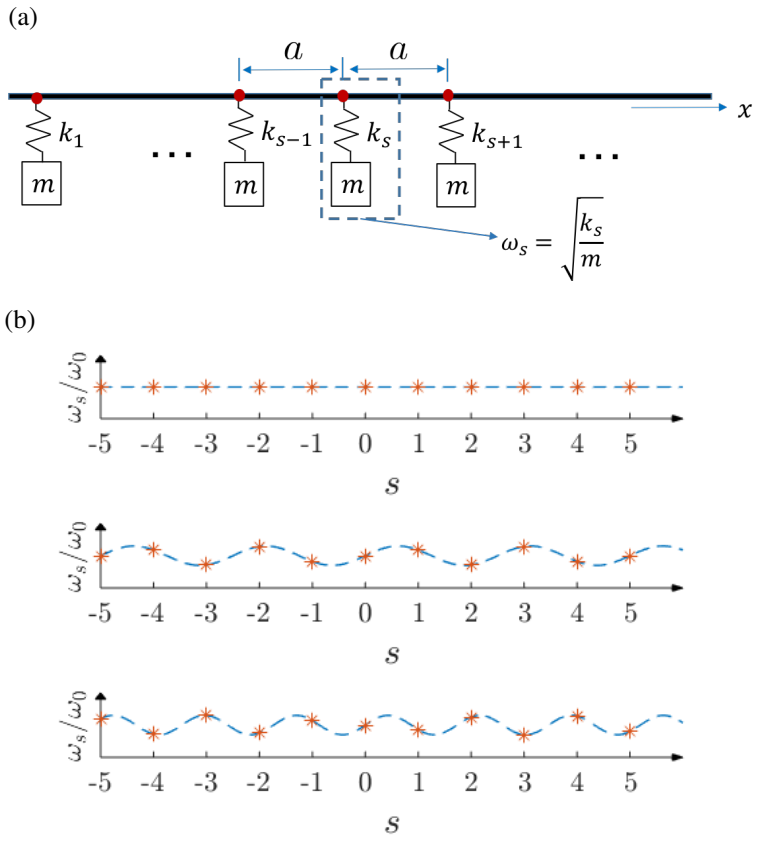

Figure 3.14: . Quasiperiodic operation on the natural frequencies of the local resonators. (a) Schematic of the beam with uniformly-placed resonators. (b) Natural frequencies as a function of resonator index s with $\alpha = 0.1$ for $\theta = 0$, $\theta = 2/5$, and $\theta = 1/\sqrt{3}$ from top to bottom accordingly.

stiffness of s-th resonator is:

$$k_s = m\omega_0^2[1 + \alpha \sin(2\pi s\theta)]^2. \tag{3.8}$$

The governing equations for the beam and the s-th resonator can be modified from Eqs. 3.2 and 3.3 to be:

$$D\frac{\partial^4 w(x,t)}{\partial x^4} + \rho A\frac{\partial^2 w(x,t)}{\partial t^2} - k_s \sum_s w_s(t)\delta(x - sa) = 0, \tag{3.9}$$

$$m\frac{\partial^2 (w(x_s,t) + w_s(t))}{\partial t^2} + k_s w_s(t) = 0, \quad s = 1, \ldots, S \tag{3.10}$$

For all the numerical analyses performed next, an identical aluminum beam as described in Section 3.2 is considered. Resonators are placed on the beam with distance $a = 5.08$ cm, and have an added mass ratio with respect to the beam of $\mu = 1.26$. In addition, ω_0 is chosen to be 90 Hz.

3.3.1 Non-trivial Topological Bandgaps and Edge-localized States

In this part, similar study as described in Section 3.2.1 in terms of variations in θ is conducted. Bulk frequency spectrum for infinite beams and the frequency spectrum for finite beams are evaluated. Edge-localized modes of finite beams and topological properties of the frequency bands are investigated. In addition, effect of the modulation level parameter α on the bulk frequency spectra is discussed.

Bulk and Finite Spectra

The approximated bulk frequency spectrum for infinite LR beams with QP natural frequencies is similar to the one obtained for infinite LR beams with QP locations (Fig. 3.4) when the modulation level α is small (i.e., $\alpha = 0.05$ as shown in Fig. 3.15a). The LR bandgap remains unaltered as θ varies, separating two spectral regions with additional bandgaps whose center frequencies depend on θ. However, when α increases, the variation of the natural frequencies of the resonators increases, and consequently the LR bandgap quickly narrows down for $\alpha = 0.1$ (Fig. 3.15b) or even rapidly closes for $\alpha = 0.3$ (Fig. 3.15c) as soon as θ deviates from 0. For small to moderate α values, the LR bandgap remains open for all the θ values. For large α values, the LR bandgap closes when θ value deviates from 0, reopens around $\theta = 0.5$ and diminishes again when θ value approaches 1. Overlapping of the additional bandgaps makes the bulk spectrum more fractal. It is worth mentioning that, the definition of low, moderate and high value of α is relative to the width of the LR bandgap which is limited by the added mass ratio. For example, if the mass ratio increases from 1.26 (used in all the numerical analyses) to 3, $\alpha = 0.3$ will be considered as

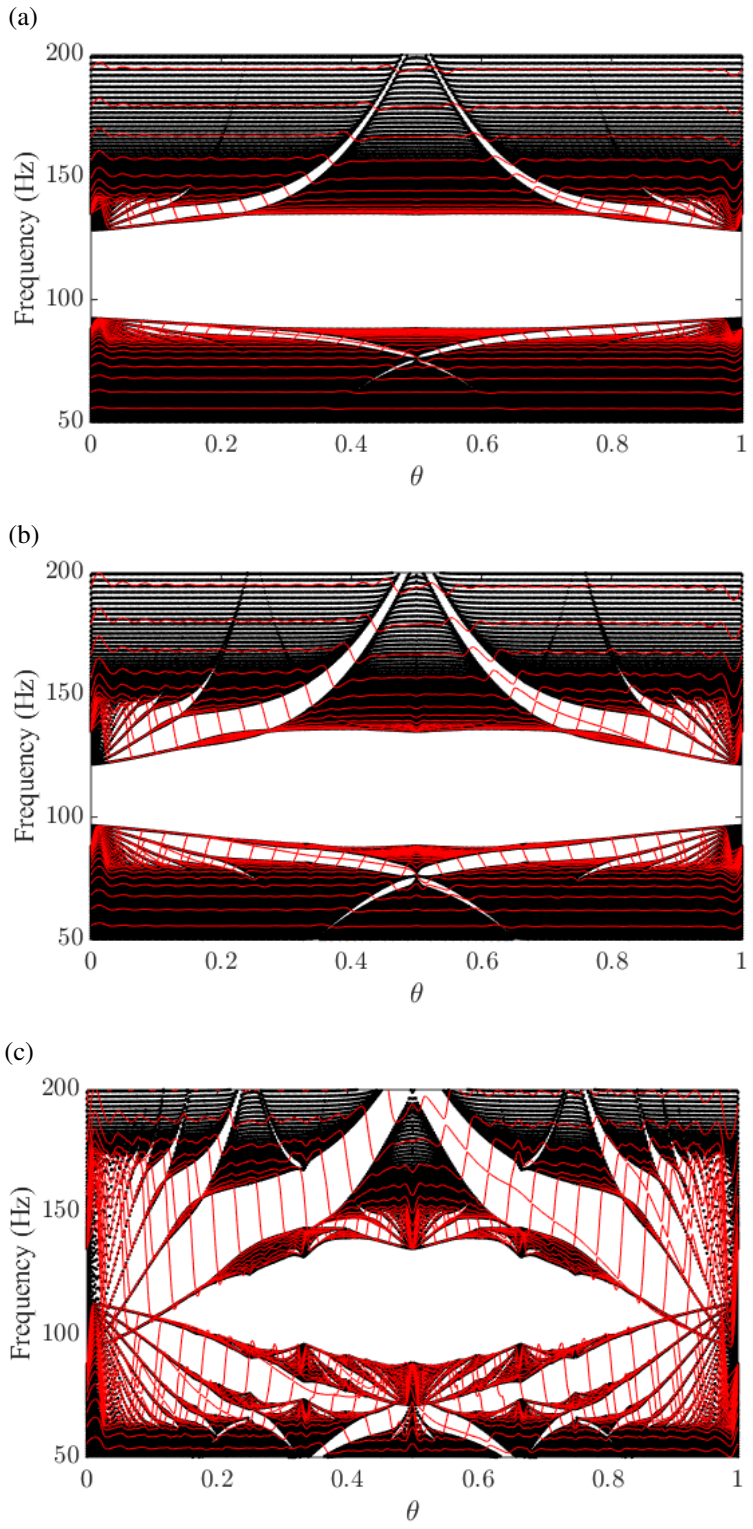

Figure 3.15: Comparison on the bulk (black) and finite beam (red) spectra as a function of θ between different modulation levels (a) $\alpha = 0.05$, (b) $\alpha = 0.1$, and (c) $\alpha = 0.3$. The finite beam spectrum, obtained for a simply supported beam, shows the presence of modes spanning the non-trivial gaps.

a moderate modulation level since the LR bandgap dose not fully close as θ varies.

In addition, the spectra of finite QP beams (30 unit cells with simply-supported boundary condition on both ends) for different modulation levels are evaluated. The obtained values are superimposed in red on top of the black bulk spectra for $\alpha = 0.05$, $\alpha = 0.1$, and $\alpha = 0.3$ in Figs. 3.15a-c respectively.

Edge-localized Modes

Red curves that are spanning the bulk gaps (white regions) in Fig. 3.15 correspond to topological edge modes localized at the right boundary of the finite beam. The zoomed-in spectra for $\alpha = 0.1$ and $\alpha = 0.3$ in Fig. 3.16 compare selected modes that correspond to bulk and finite structure frequencies. As expected, the selected modes that appear in the bandgap are edge-localized; while the modes lie inside the black region defined by the bulk bands are bulk modes. The localized nature for the response of the resonators is also observed. For $\alpha = 0.1$ (moderate modulation level), the relative displacements of the resonators are in phase and out of phase with respect to the beam's deflection at frequencies below and above the LR bandgap, which remains open for all θ values, respectively. For $\alpha = 0.3$ (high modulation level), even though the LR bandgap vanishes at very small θ values, the same phenomena for the in-phase and out-of-phase responses of the resonators are kept for larger θ values at which the LR bandgap reopens.

Topological Properties of the Bands

The topological properties of the bands are evaluated again by the IDS of the system defined in Eq. 3.4. Figure 3.17a displays the IDS as a function of θ for modulation level $\alpha = 0.1$, which corresponds to the bulk spectrum shown in Fig. 3.15b. Similarly, Fig. 3.17b shows the IDS of the system for $\alpha = 0.3$, which represents the bulk spectrum in Fig. 3.15c. In each figure, three representative additional bandgaps are highlighted by white dashed lines and labeled with the slope of the lines $m = 1, 2, 3$. However, the number of sharp lines

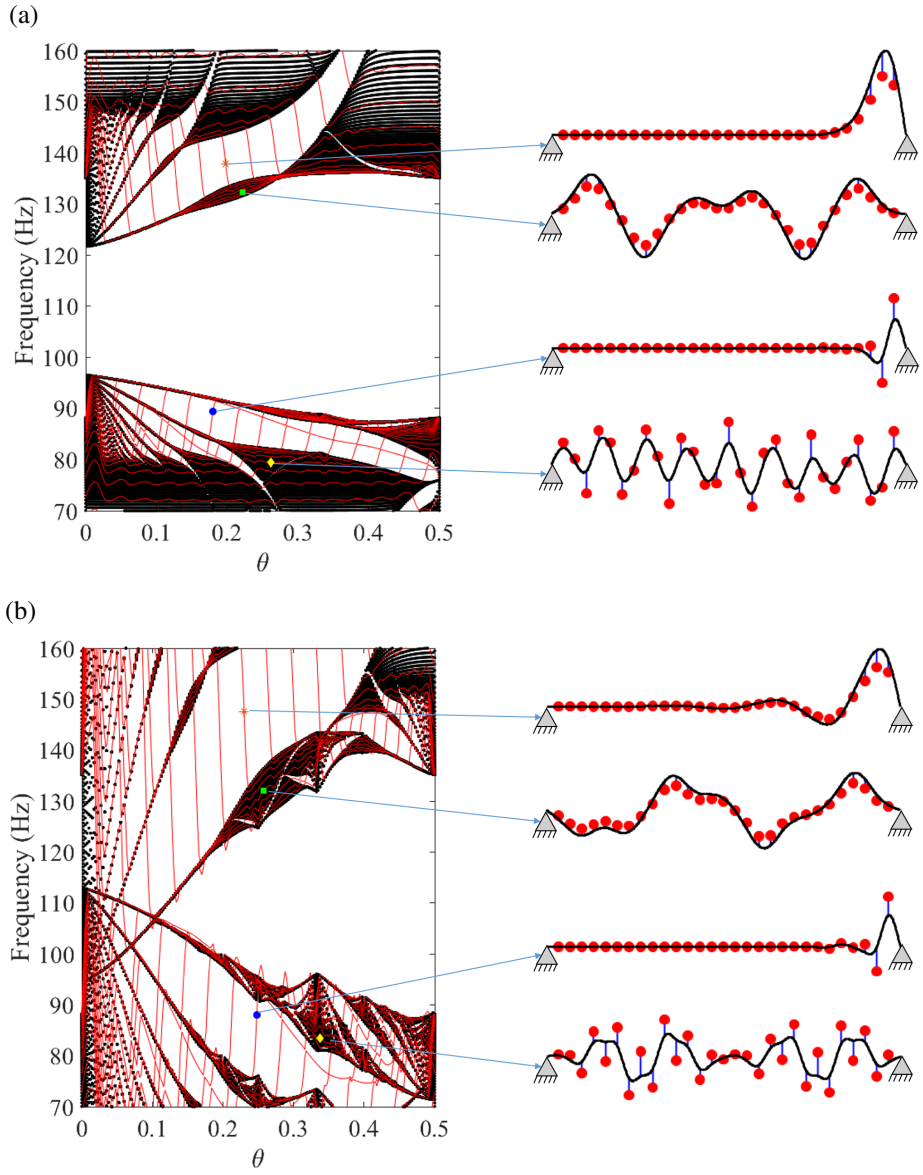

Figure 3.16: Details of the spectra for $\alpha = 0.1$ (a) and $\alpha = 0.3$ (b) and the corresponding bulk and edge-localized modes. The black curve represents the reflection of the beam, while the red circles denote the displacement of the resonators.

visible in the IDS colormap for $\alpha = 0.3$ is much larger than the one shown for $\alpha = 0.1$, manifesting the fact that the system with higher modulation level exhibits more fractal frequency spectrum with more additional bandgaps.

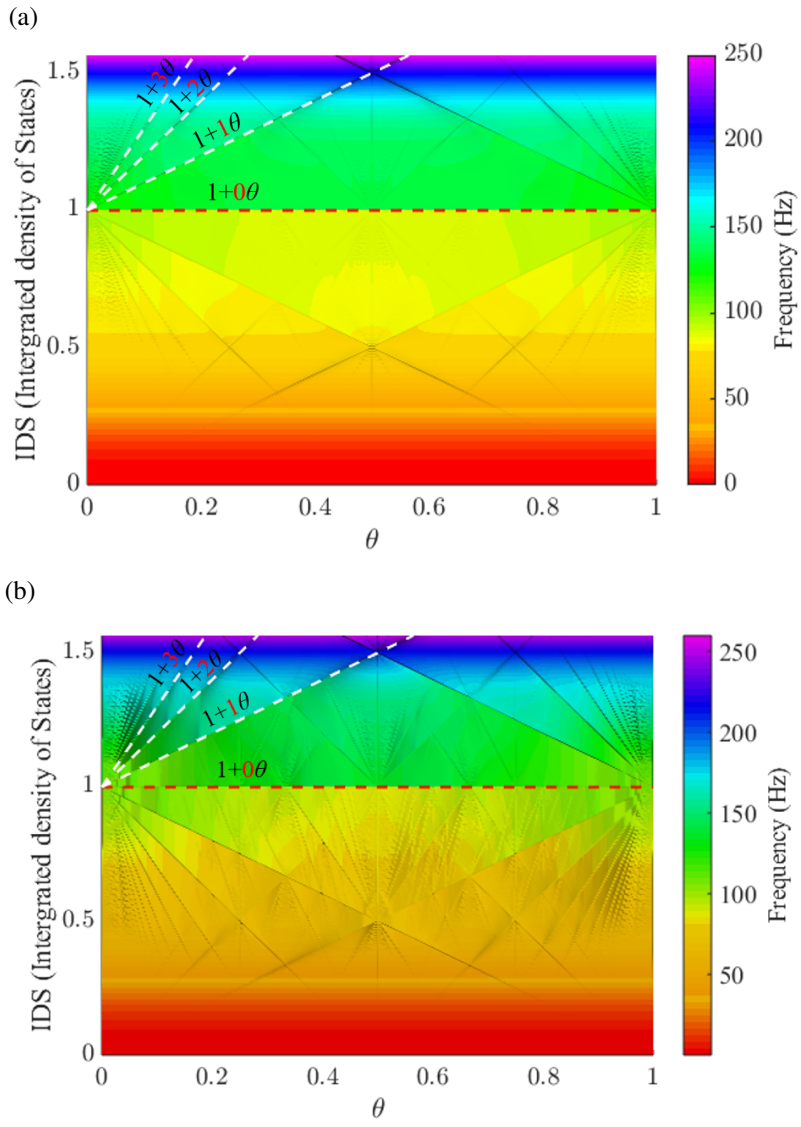

Figure 3.17: IDS as a function of θ exhibits sharp linear jumps at the bandgap for $\alpha = 0.1$ (a) and $\alpha = 0.3$ (b). The colormap indicates frequency Ω. The slope of three of theses lines (highlight by white dashed lines) is equal to $m = 1 - 3$, while for the LR bandgap (red dashed line) is $m = 0$, indicating this band is topologically trivial. System with higher modulation level α manifests more fractal frequency spectrum with more bandgaps, presenting larger number of sharp linear lines in IDS colormap.

3.4 Mode Transitions

In this section, mode transitions from edge-localized modes to interior-localized modes and the localization transitions from one boundary to the other boundary by phase modulations are investigated.

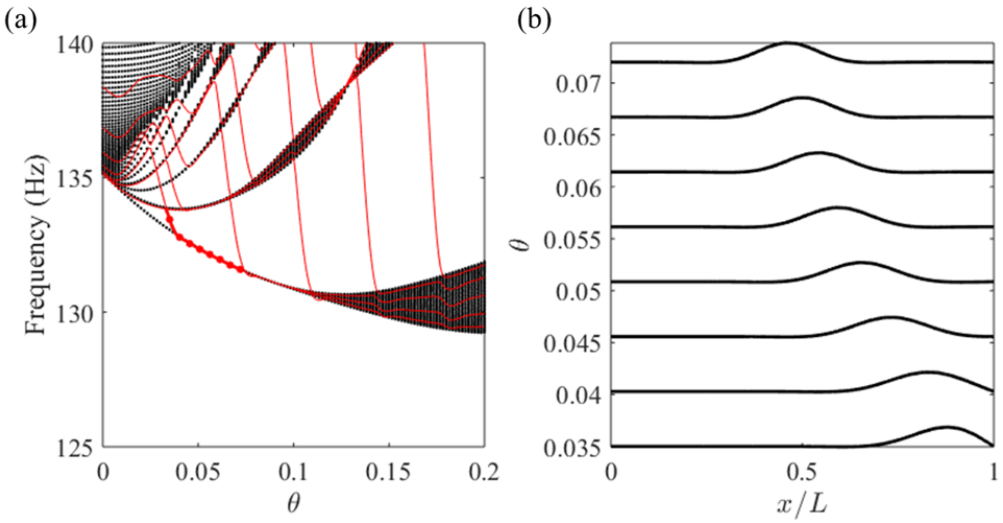

Figure 3.18: Localization transition from edge to interior for LR beam with QP locations of resonators ($R = 0.3a$). (a) Bulk (black) and finite beam (red) spectra as functions of θ, where selected branch of modes is tracked and marked by thick red lines. (b) The normalized mode shapes are displayed as a function of θ, which correspond to the red dots marked on the selected branch.

3.4.1 Localization Transitions from Edge to Interior

In addition to edge-localized states, the family of LR beams with QP resonators supports vibration modes that are localized in the interior of domain. These interior-localized modes are not classified as topological since they lie inside the regions defined by the bulk bands and do not span the non-trivial gaps, and they emerge from the joining of a topological mode branch to the bulk bands. Two illustrative examples are presented: one for varying the locations of the resonators with $R = 0.3a$ as shown in Fig. 3.18, and another one for varying the natural frequencies of the resonators with $\alpha = 0.1$ in Fig. 3.19. The finite beams are assumed to be simply-supported on both ends. For each case, the vibration modes highlighted by the thick red lines in the zoomed spectra are tracked by tracing the mode shapes with different θ values denoted by the red dots. A topological edge mode can migrate to the interior of the structure as its branch merges with the bulk. Interestingly, for some modes, the transition occurs while maintaining the shape, in a manner that is vaguely reminiscent of solitons [85].

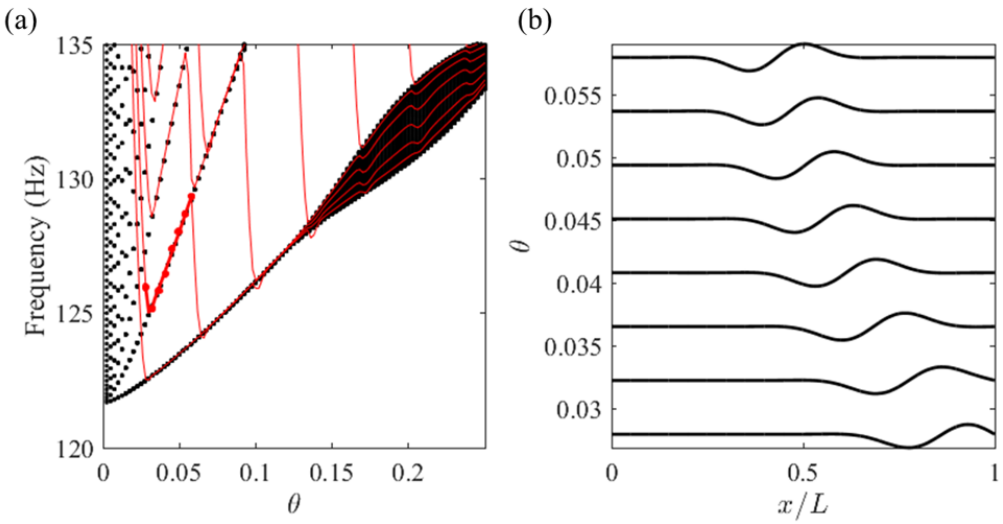

Figure 3.19: Localization transition from edge to interior for LR beam with QP natural frequencies of resonators ($\alpha = 0.1$). (a) Bulk (black) and finite beam (red) spectra as functions of θ, where selected branch of modes is tracked and marked by thick red lines. (b) The normalized mode shapes are displayed as a function of θ, which correspond to the red dots marked on the selected branch.

3.4.2 Mode Transitions by Phase Modulations

So far, all the modes spanning the topological bandgaps are localized at the right boundary of the structure as a consequence of the finite structure constructed according to the QP pattern from $x = 0$ (left boundary) and terminated at $x = L$ (right boundary). Here, localized modes at the left boundary is shown to be obtained by introducing a phase parameter ϕ in the quasiperiodic pattern. For varying the location of the resonators, Eq. 3.1 is modified to be:

$$x_s = sa + R\sin(2\pi s\theta + \phi). \tag{3.11}$$

And for varying the natural frequencies of the resonators, Eq. 3.7 is updated to be:

$$\omega_s = \omega_0[1 + \alpha\sin(2\pi s\theta + \phi)]. \tag{3.12}$$

For a given θ, varying the phase ϕ between 0 and 2π produces cyclic modulations of the resonators' locations or natural frequencies. Figure 3.20 demonstrates the mode transition

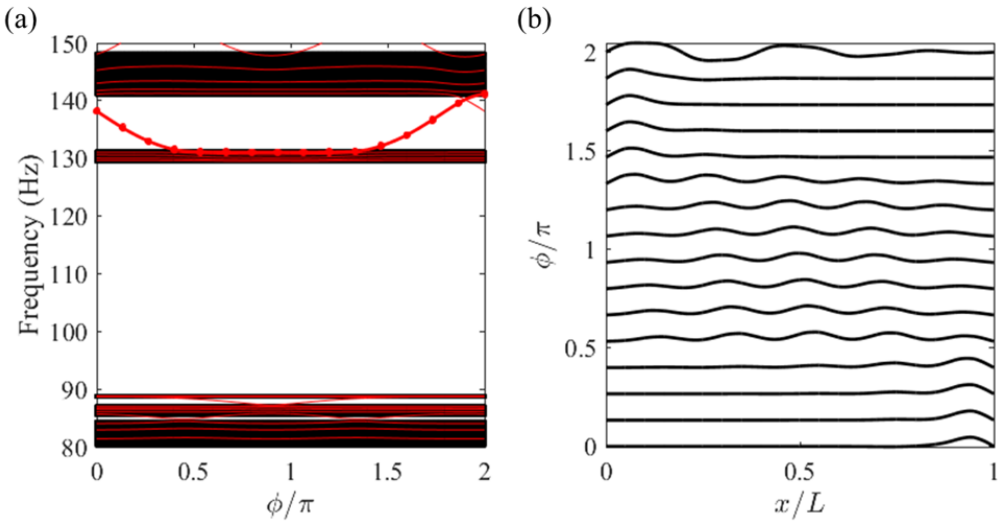

Figure 3.20: Mode transition through phase modulation on the locations of the resonators with $\theta = 0.17$ ($R = 0.3a$). (a) Bulk (black) and finite beam (red) spectra as functions of modulation ϕ, where selected branch of modes is tracked and marked by thick red lines. (b) The normalized mode shapes are displayed as a function of ϕ, which correspond to the red dots marked on the selected branch.

via phase modulation on the location of the resonators ($R = 0.3a$) with fixed $\theta = 0.17$. The mode starts from edge-localized at the right boundary ($x = L$) at $\phi = 0$. When the edge mode branch marked in Fig. 3.20a merges with the bulk bands, the mode changes to bulk mode, and eventually it localizes at the left boundary ($x = 0$) when the branch detaches from the bulk bands.

Figure 3.21 demonstrates the mode transition by phase modulation on the natural frequencies of the resonators ($\alpha = 0.1$) with fixed $\theta = 0.13$. The mode which starts from edge-localized at the right boundary ($x = L$) at $\phi = 0$ quickly transforms to bulk mode when the branch marked in Fig. 3.21a joins the bulk bands. After the branch leaves the bulk bands, the mode becomes localized at the left boundary ($x = 0$), and remains its left localization when the branch crosses the bandgaps. Interestingly, when two branches cross within a bandgap as marked in blue circle in Fig. 3.21a, the corresponding mode has a mode shape localized on both boundaries ($x = 0, L$), as highlighted in blue in Fig. 3.21b.

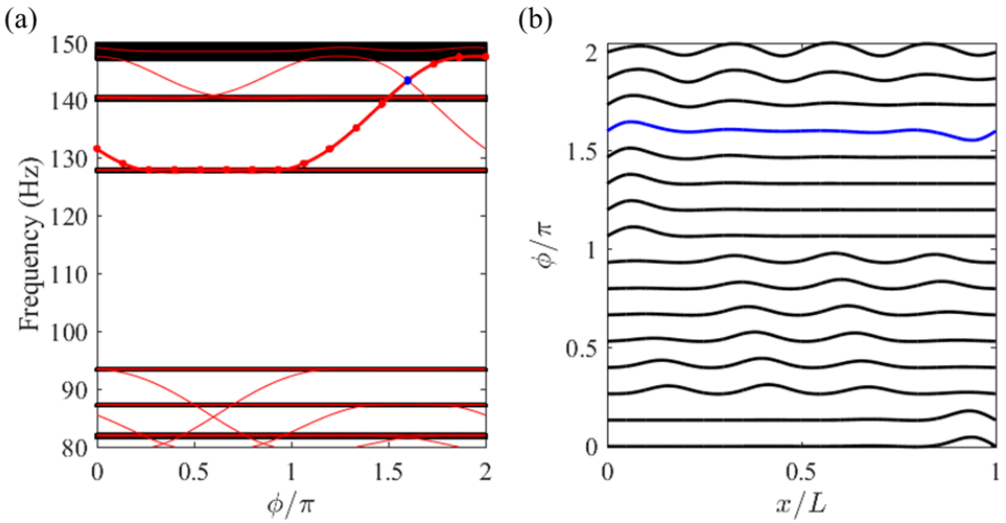

Figure 3.21: Mode transition through phase modulation on the natural frequencies of the resonators with $\theta = 0.13$ ($\alpha = 0.1$). (a) Bulk (black) and finite beam (red) spectra as functions of modulation ϕ, where selected branch of modes is tracked and marked by thick red lines. (b) The normalized mode shapes are displayed as a function of ϕ, which correspond to the red dots marked on the selected branch. When two branches cross within the bandgap as marked in blue circle in the spectrum, the corresponding mode shape is localized at both ends (highlighted in blue in the mode shape plot).

3.5 Conclusions

In this chapter, mechanical locally resonant metastructures in the form of beams with quasiperiodic distributions of resonators are investigated. The quasiperiodic pattern is applied to the metastructure in two ways.

First, by varying the parameter θ defining the locations of the resonators, additional non-trivial topological bandgaps are created. In finite metastructures, these bands host modes that are localized at the boundary and whose frequency can be chosen through proper selection of the quasiperiodic parameter which defines the location of the resonators. The onset of the locally resonant bandgap and of the additional non-trivial bandgaps with associated edge states is demonstrated both through numerical simulations and in experiments conducted on a cantilever beam carrying an array of 30 resonators.

Second, by varying the parameter θ defining the natural frequencies of the resonators,

non-trivial topological bandgaps and edge-localized states are also created. Higher modulation level α leads to more fractal bulk frequency spectrum.

Furthermore, transition of the localized modes as a function of θ from the boundary to the interior of the finite structure is illustrated. Additional ϕ as a phase modulation parameter is introduced to the system and edge-bulk-edge transitions are observed as ϕ varies.

The findings of this chapter suggest the application of quasiperiodic arrangement of resonators (or, in general, of mechanical inclusions) as a potentially effective way to achieve vibration attenuation over multiple frequency bands, to control the onset of vibration localization at desired frequencies, and to move the localization along the finite structure.

CHAPTER 4
ELECTROMECHANICAL LOCALLY RESONANT METASTRUCTURES WITH QUASIPERIODIC INDUCTIVE SHUNT CIRCUITS

4.1 Introduction

This chapter continues to explore quasiperiodic locally resonant metastructures. In analogy with purely mechanical locally resonant metastructures investigated in Chapter 3, the study is carried on electromechanical locally resonant metastructures, utilizing the flexibility offered by the connected shunt circuits. First, the concept is demonstrated on a piezoelectric bimorph beam in transverse motion with segmented electrodes acting as electromechanical resonators. Next, the frequency spectrum is evaluated as a function of a quasiperiodic parameter that defines the natural frequencies of the shunt circuits. Spectra of bimorph beams made of different piezoelectric materials are compared. The topological properties of the frequency bandgaps in the spectra are evaluated. Finally, experiments are performed on a beam with 30 pairs of piezoceramic patches that are connect to digitally programmable synthetic impedance shunt circuits.

4.2 Quasiperiodic Piezoelectric Bimorph Beams

The system under consideration is a piezoelectric bimorph beam, which is made of a conductive central substrate sandwiched by two continuous and symmetrically located piezoelectric layers as shown in Fig. 4.1. The thickness of the electrode layers and bonding layers is assumed to be negligible. Both piezoelectric layers are poled in the thickness direction ($+z$ direction in Fig. 4.1a). The outer surface electrodes are segmented as pairs and connected to inductive shunt circuits and the inner electrodes are connected through the conductive substrate. The central substrate has width b, thickness h_s, mass density ρ_s, and

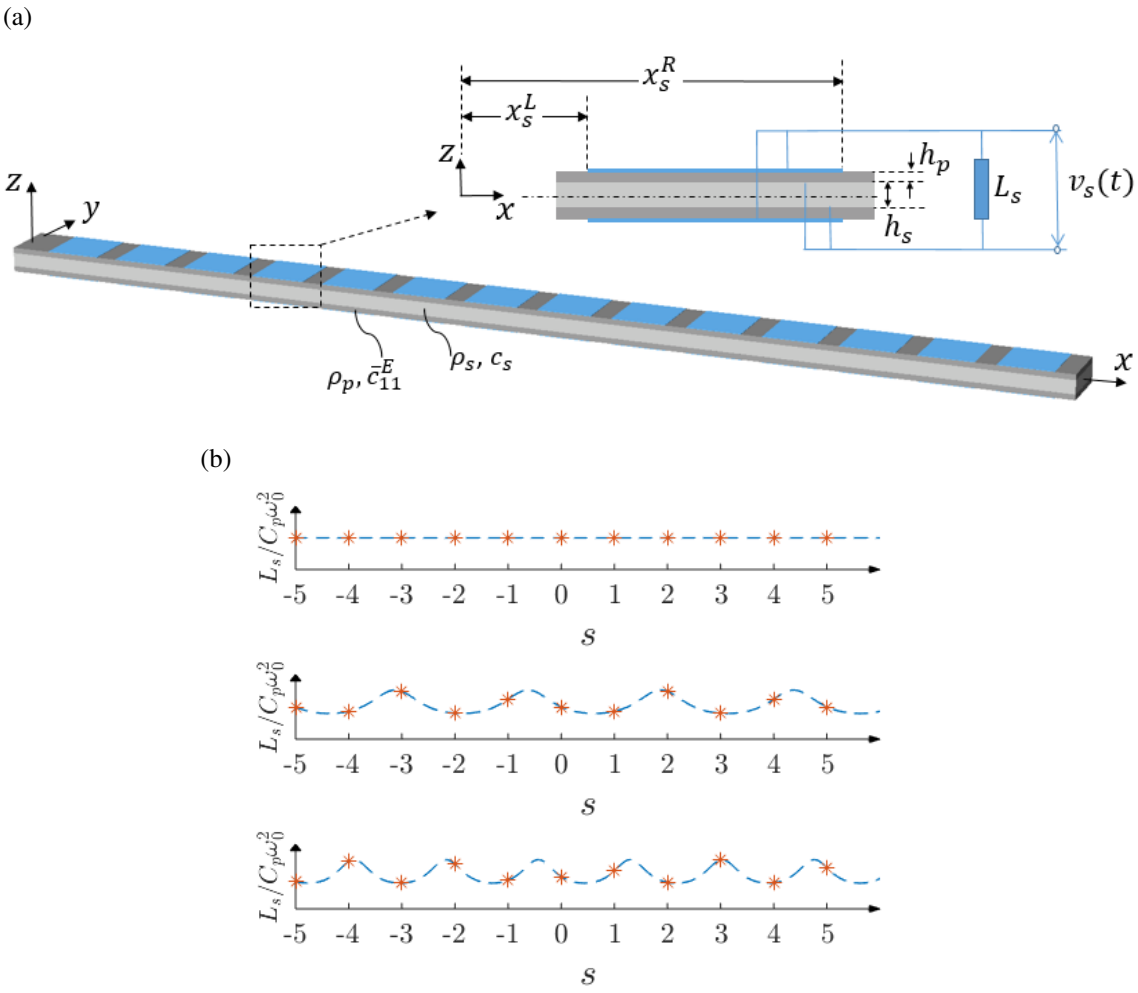

Figure 4.1: Quasiperiodic operation on the inductive shunt circuits. (a) Schematic of a piezoelectric bimorph beam with a close up showing the s-th electrode pair shunted to an inductor of inductance L_s. The piezoelectric layers are symmetrically bonded to the central substrate and connected in parallel for transverse vibrations. (b) Inductance values as a function of electrode pair index s for $\theta = 0$, $\theta = 2/5$, and $\theta = 1/\sqrt{3}$ from top to bottom accordingly.

elastic modulus c_s. The piezoelectric layers have width b, thickness h_p, elastic modulus at constant electric field $\bar{c}_{11}^E$, effective piezoelectric stress constant $\bar{e}_{31}$, and permittivity component at constant strain $\bar{\epsilon}_{33}^S$. The $\bar{(\cdot)}$ indicates effective piezoelectric material properties for 1D thin layers that are derived from 3D constitutive equations as:

$$\bar{c}_{11}^E = \frac{1}{s_{11}^E}, \quad \bar{e}_{31} = \frac{d_{31}}{s_{11}^E}, \quad \bar{\epsilon}_{33}^S = \epsilon_{33}^T - \frac{d_{31}^2}{s_{11}^E}, \tag{4.1}$$

where s_{11}^E is the elastic compliance at constant electric field, d_{31} is the piezoelectric strain constant, and ϵ_{33}^T is the permittivity component at constant stress.

Based on Euler–Bernoulli beam theory, the governing electromechanical equations for the beam with multiple segmented electrodes in transverse motion and the current balance in the inductive shunt circuits are:

$$D\frac{\partial^4 w(x,t)}{\partial x^4} + m\frac{\partial^2 w(x,t)}{\partial t^2} - \vartheta \sum_s v_s(t)\frac{\mathrm{d}^2}{\mathrm{d}x^2}\Big[H(x-x_s^L) - H(x-x_s^R)\Big] = 0, \quad (4.2)$$

$$C_{p,s}\frac{\mathrm{d}v_s(t)}{\mathrm{d}t} + \frac{1}{L_s}\int v_s(t)\mathrm{d}t + \vartheta \int_{x_s^L}^{x_s^R} \frac{\partial^3 w(x,t)}{\partial x^2 \partial t}\mathrm{d}x = 0, \quad s = 1,\ldots,S \quad (4.3)$$

where $w(x,t)$ is the transverse displacement of the beam at location x and time t, $v_s(t)$ is the voltage between the s-th electrode pair and the central substrate, and L_s is the inductance of the s-th inductor. The s-th electrode with width b starts at $x = x_s^L$ and ends at $x = x_s^R$. In addition, $D = \frac{2b}{3}\big(c_s\frac{hs^3}{8} + \bar{c}_{11}^E\big[\big(h_p + \frac{h_s}{2}\big)^3 - \frac{h_s^3}{8}\big]\big)$ is the short circuit bending stiffness of the bimorph beam, $m = b(\rho_s h_s + 2\rho_p h_p)$ is the mass per length of the beam, $\vartheta = \bar{e}_{31} b(h_s + h_p)$ is the electromechanical coupling term in physical coordinates, and $C_{p,s} = \frac{2\bar{\epsilon}_{33}^S b}{h_p}(x_s^R - x_s^L)$ is the piezoelectric capacitance across the s-th electrode pair.

The quasiperiodic pattern generation procedure is applied to the natural frequencies ω_s of the shunt circuits:

$$\omega_s = \frac{1}{\sqrt{L_s C_{p,s}}} = \omega_0[1 + \alpha\sin(2\pi s\theta)], \quad (4.4)$$

where ω_0 is the natural frequency of the shunt circuits in an underlying uniform/periodic arrangement (mean natural frequency), α is a ratio that quantifies the maximum frequency variation from ω_0 (modulation level), and θ is the angular increment. Assuming all the electrode pairs are the same with length $\Delta x_s = x_s^R - x_s^L = \Delta x$ and with capacitance

$C_{p,s} = C_p$, then the inductance values need to be varied as:

$$L_s = \frac{1}{C_p \omega_0^2 [1 + \alpha \sin(2\pi s\theta)]^2}. \tag{4.5}$$

Figure 4.1b plots the inductance values L_s as a function of electrode pair index s for three archetypal θ values: $\theta = 0$ as the uniform case, rational $\theta = 2/5$ representing periodic cases, and $\theta = 1/\sqrt{3}$ standing for aperiodic cases. In addition, the electrode pairs are equally spaced with distance $\Delta x_s^d = x_{s+1}^L - x_s^R = \Delta x^d$

4.3 Non-trivial Topological Bandgaps and Edge-localized States

In this section, the study on both the bulk frequency spectrum for infinite electromechanical beams and the the frequency spectrum for finite electromechanical beams in terms of variation in θ is conducted. Edge-localized modes of finite beams and topological properties of the frequency bandgaps are evaluated. Table 4.1 summarizes the parameters in the numerical analyses performed next.

4.3.1 Bulk and Finite Spectra

The spectrum of an infinite electromechanical LR beam is obtained approximately by a long structure (i.e., 600 cells) with periodic boundary conditions on both ends. The natural frequencies of the large structure can be estimated from the discretized eigenvalue problem via an analysis approach based on Galerkin's approximation. All the natural frequencies of the structure lie in the bulk band of the infinite configuration for rational θ values that are commensurate with 600. Figure 4.2 plots the variation of the natural frequencies as a function of QP parameter θ in black for three different piezoelectric materials with the same modulation level $\alpha = 0.05$. All three obtained bulk spectra have patterns that are similar to the Hofstadter butterfly [64].

For $\theta = 0$, all the inductive shunt circuits are the same, and an electromechanical LR

Table 4.1: Parameters for the model of the quasiperiodic electromechanical metastructure

Symbol	Description	Value	Unit
b	Width of the beam	2.1	cm
c_s	Elastic modulus of the central substrate	69.9	GPa
ρ_s	Mass density of the central substrate	2700	kg/m^3
h_s	Thickness of the central substrate	0.508	mm
h_p	Thickness of the piezoelectric layers	0.55	mm
ρ_p	Mass density of the piezoelectric layers	PMN-PT (33% PT): 8060	kg/m^3
		PZT-5A: 7750	
		PZT-5J: 7500	
$\bar{e}_{31}$	Effective piezoelectric stress constant	PMN-PT (33% PT): -19.3	C/m^2
		PZT-5A: -12.3	
		PZT-5J: -10	
$\bar{c}_{11}^E$	Effective piezoelectric elastic modulus at constant electric field	PMN-PT (33% PT): 14.5	GPa
		PZT-5A: 61.0	
		PZT-5J: 81.3	
$\bar{e}_{33}^S$	Effective piezoelectric permittivity component at constant strain	PMN-PT (33% PT): 47.0	nF/m
		PZT-5A: 13.3	
		PZT-5J: 10.3	
$\bar{\alpha}$	System-level electromechanical coupling	PMN-PT (33% PT): 0.4334	
		PZT-5A: 0.1649	
		PZT-5J: 0.1068	
Δx	Length of the electrode	2.1	cm
Δx^d	Space between two adjacent electrodes	1	mm
ω_0	Mean natural frequency of the circuit	320	Hz

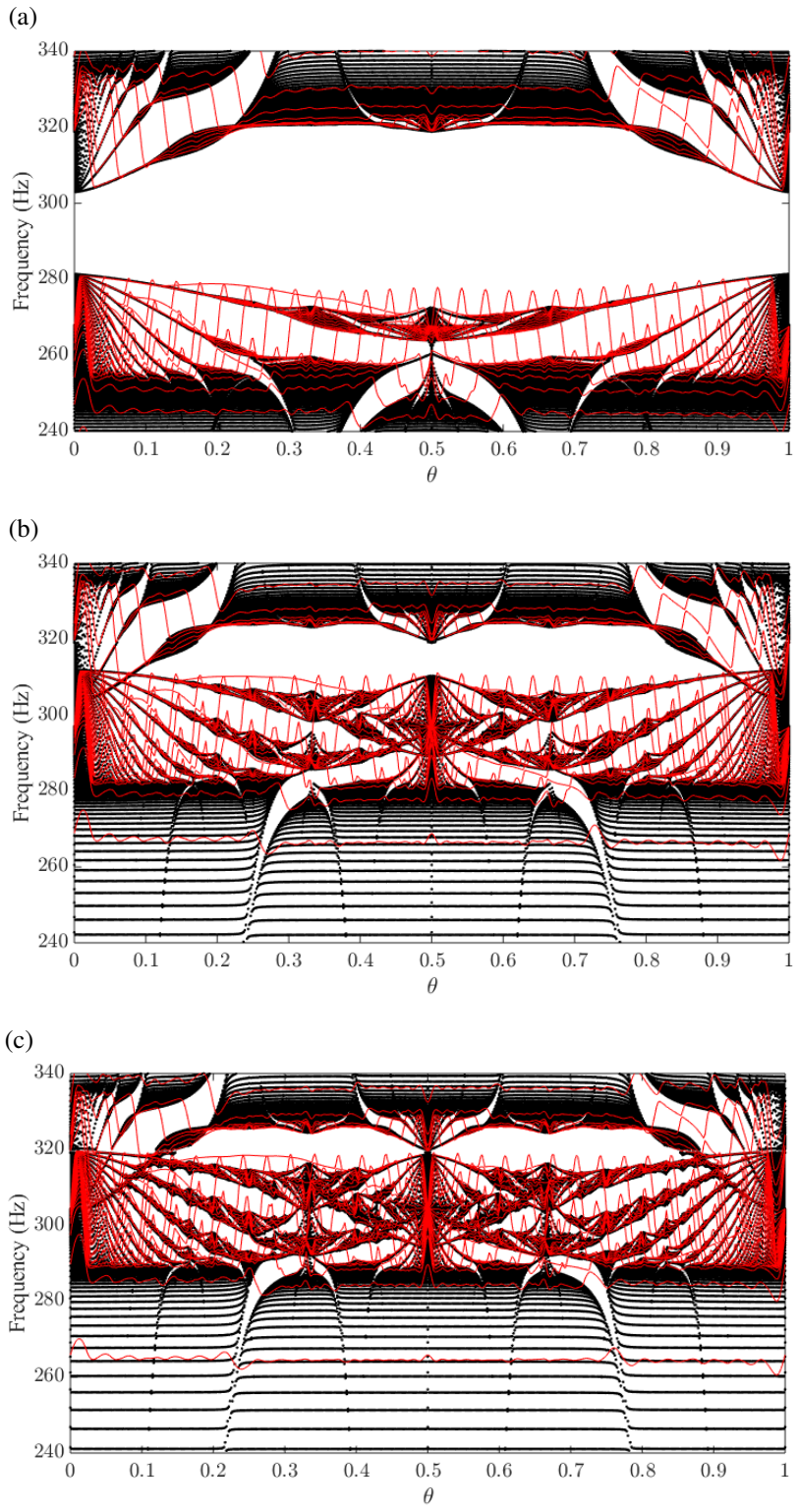

Figure 4.2: Comparison on the bulk (black) and finite bimorph beams (red) spectra as a function of θ between different piezoelectric materials (a) PMN-PT (33% PT), (b) PZT-5A, and (c) PZT-5J. The finite bimorph beam spectrum (simply supported on both ends) shows the presence of modes spanning the non-trivial gaps.

bandgap appears as expected. The bandgap formation in piezoelectric LR metastructure is shown to be associated with a frequency-dependent modal stiffness term, instead of the frequency-dependent modal mass term in mechanical LR metastructure [18]. As a consequence, unlike the mechanical LR bandgap which starts at the natural frequency of the resonators and of which the width is limited by the added mass ratio, electromechanical LR bandgap ends at the natural frequency of the resonant shunts and the bandwidth is limited by dimensionless system-level electromechanical coupling term $\bar{\alpha}$. A single crystal material (i.e., PMN-PT with 33% PT) is included in this comparison for its significantly larger electromechanical coupling and elastic compliance. In addition, PZT-5A and PZT-5J are both commonly used piezoelectric ceramics, and the latter is used in the experiments.

The bulk frequency spectra of electromechanical LR beams with QP inductive shunt circuits shown in Fig. 4.2 are analogous to the ones obtained for mechanical LR beams with QP natural frequencies shown in Fig. 3.15. Instead of the comparison between systems of various modulation levels α with fixed added mass ratio μ as done in Section 3.3.1, the investigation here is performed on structures with different system-level electromechanical coupling terms $\bar{\alpha}$ (by using different piezoelectric materials) with the same modulation level α.

As seen in the bulk spectrum for QP bimorph beams with high system-level electromechanical coupling $\bar{\alpha}$ made of PMN-PT (33% PT) in Fig. 4.2a, the LR bandgap remains open and separates spectral region with additional bandgaps as θ varies. When the coupling level $\bar{\alpha}$ decreases, the LR bandgap and all the additional bandgaps become narrower, and overlapping of the additional bandgaps makes the spectra more fractal. The LR bandgap closes rapidly as soon as θ value deviates from of PZT-5J (Fig. 4.2c). However, the spectrum for the case of PZT-5A reopens around $\theta = 0.5$, while the spectrum for the case of PZT-5J at $\theta = 0.5$ stays closed. It is worth mentioning that all the bandgaps can be widened through the use of negative capacitance (NC) circuits in parallel with the shunt circuits by increasing the effective value of the dimensionless coupling term $\bar{\alpha}$. For example, bimorph beams

made of PZT-5J with additional NC circuits connected with inductive shunt circuits can have similar bulk spectrum as the bimorph beams made of PMN-PT (33% PT), with a LR bandgap that does not fully close as θ varies.

In addition, the spectra of finite QP piezoelectric bimorph beams (30 unit cells with simply-supported boundary condition on both ends) for different piezoelectric materials are evaluated using the Galerkin's method. The obtained values are superimposed in red on top of the black bulk spectra in Fig. 4.2.

4.3.2 Edge-localized Modes

Figures 4.3a and 4.3b plot the close-up spectra for for bimorph beams made of PMN-PT (33% PT) and PZT-5J that are shown in Figs. 4.2a and 4.2c, respectively. Each spectrum is marked with representative bulk and edge-localized mode frequencies. The selected modes which are on the red curves spanning the bulk bandgaps are edge-localized modes, while the modes appear inside the bulk bands have mode shapes with deflection across the whole beam. With higher system-level electromechanical coupling, the QP bimorph beams made of PMN-PT (33% PT) can hold localized modes at lower frequencies than the beams made of PZT-5J.

4.3.3 Topological Properties

Splitting of the bulk bands relates to the change in the density of states. The topological properties of the bands are evaluated by the IDS of the piezoelectric bimorph beams as defined in Eq. 3.4. Figures 4.4a and 4.4b display the IDS as θ varies for both the piezoelectric bimorph beams made of PMN-PT (33% PT) and PZT-5J, which correspond to the bulk spectra shown in Figs. 4.2a and 4.2c, respectively. The colormap displays the frequency Ω in Eq. 3.4, and the sharp changes of the color highlight the jumps of frequency inside the bandgaps in the IDS. It can be noticed that more sharp lines are visible in the IDS for the bimorphs made of PZT-5J than those made of PMN-PT (33% PT). This again indicates

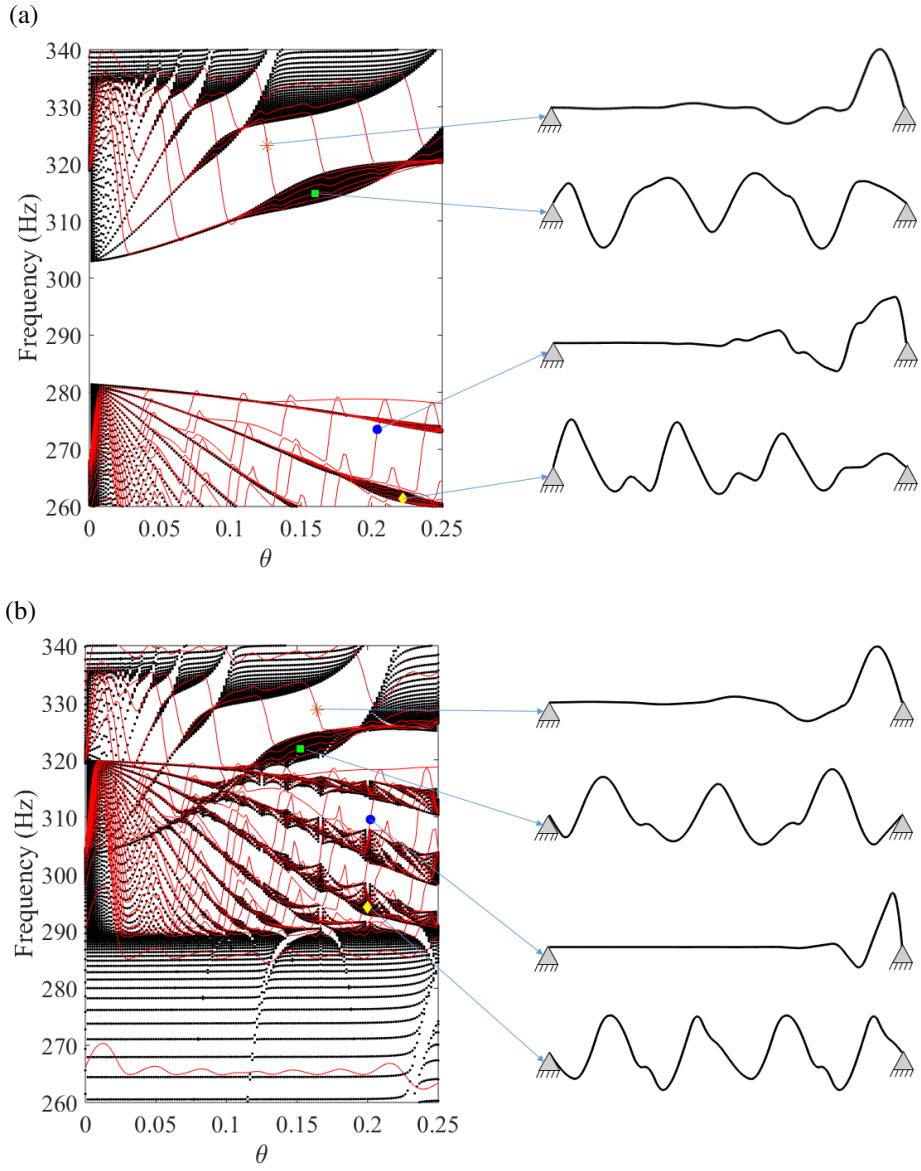

Figure 4.3: Details of the spectra for bimorph beams made of PMN-PT (33% PT) with $\bar{\alpha} = 0.4334$ (a) and of PZT-5J with $\bar{\alpha} = 0.1068$ (b) and the corresponding bulk and edge-localized modes. The black curve represents the deflection of the beam.

that, under the same modulation level, the system with smaller system-level electromechanical coupling exhibits more fractal frequency spectrum (though the bandgaps are narrower in general). In addition, in each plot in Fig. 4.4, three major additional bandgaps above the LR bandgap are marked in white dashed lines and labeled with the slope of the line m. The slope m here is a topological invariant label of the bandgap and gives the number of topological edge modes that span the bandgap in the interval between two subsequent

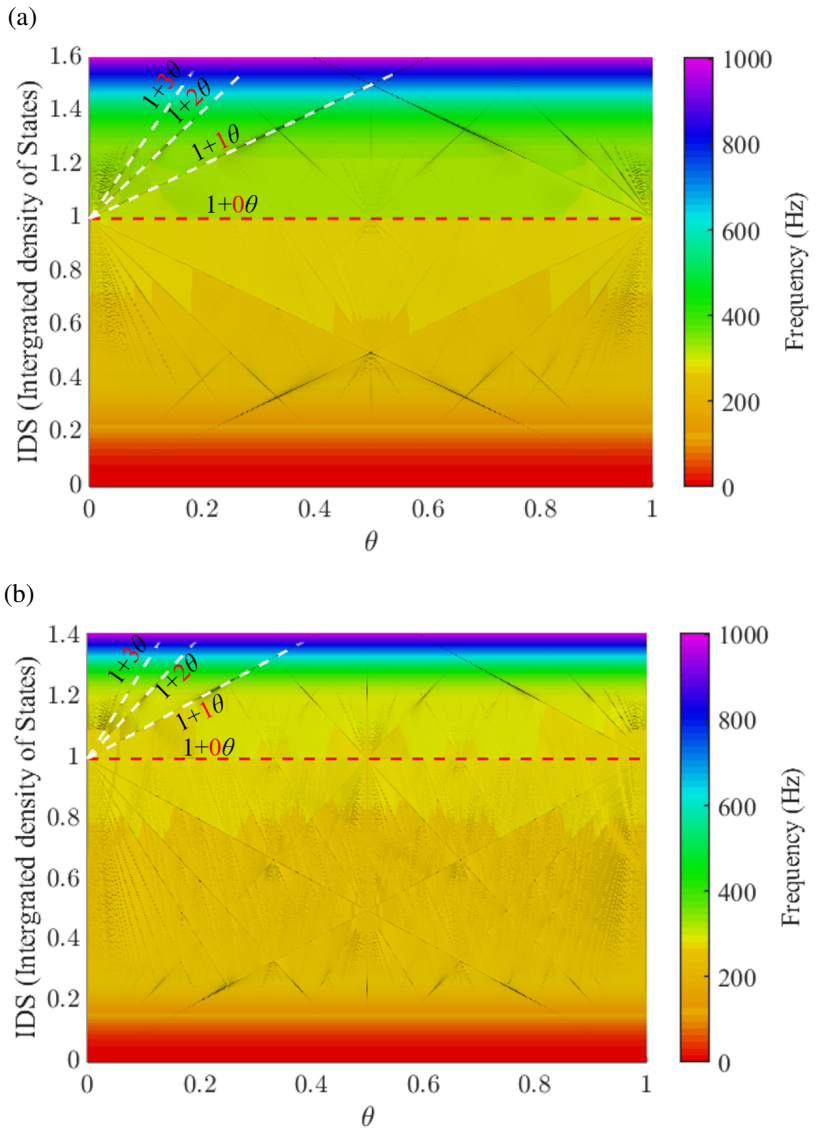

Figure 4.4: IDS as a function of θ exhibits sharp linear jumps at the bandgaps for bimorph beams made of PMN-PT (33% PT) with $\bar{\alpha} = 0.4334$ (a) and of PZT-5J with $\bar{\alpha} = 0.1068$ (b). The colormap indicates frequency Ω. The slope of three of theses lines (highlight by white dashed lines) is equal to $m = 1 - 3$, while for the LR bandgap (red dashed line) is $m = 0$, indicating this band is topologically trivial. Under same modulation level α, system with smaller system-level electromechanical coupling $\bar{\alpha}$ manifests more fractal frequency spectrum with more bandgaps, presenting larger number of sharp linear lines in IDS colormap.

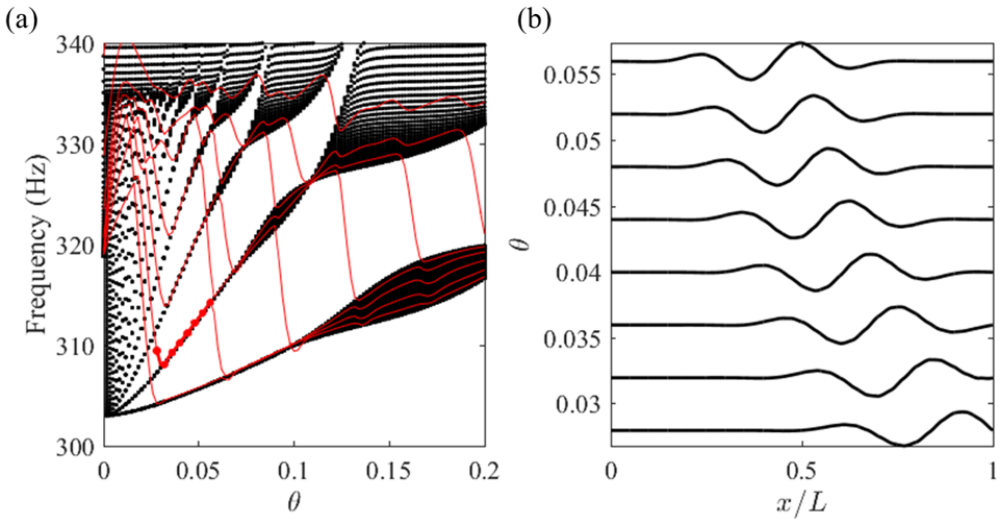

Figure 4.5: Localization transition from edge to interior for electromechanical LR beam with QP inductive shunt circuits (made of PMN-PT with 33% PT, $\alpha = 0.05$). (a) Bulk (black) and finite beam (red) spectra as functions of θ, where selected branch of modes is tracked and marked by thick red lines. (b) The normalized mode shapes are displayed as a function of θ, which correspond to the red dots marked on the selected branch.

commensurate values of θ [63].

4.4 Mode Transitions

The mode transitions previously illustrated on mechanical LR metastructures with QP resonators in Section 3.4 also occur in the electromechanical LR metastructures with QP inductive shunt circuits, as discussed in this section.

4.4.1 Localization Transitions from Edge to Interior

The family of piezoelectric bimorph beams with QP inductive shunt circuits support interior-localized modes. These modes typically start from a topological edge-localized mode, which migrates to the interior of the structure as the mode branch merges with the bulk bands as θ varies. The modes localized at the interior are most likely to be found at small θ values when only one finite beam branch joins the bulk bands. A representative example is considered here using a piezoelectric bimorph beam made of PMN-PT (33%PT) with

modulation level $\alpha = 0.05$. The modes, tracked in Fig. 4.5b as θ varies, are denoted by the red dots marked on the selected branch (red thick line) in the zoomed spectrum in Fig. 4.5a. Interior-localized modes are harder to find in the QP electromechanical metastructures with smaller system-level electromechanical coupling $\bar{\alpha}$ (i.e., bimorph beam made of PZT-5J) when the LR bandgap closes at small θ values. However, it is possible to add NC circuits to the system to increase the effective electromechanical coupling and widen the bandgaps so that interior-localized modes are more likely to form. In addition, even though such interior-localized modes are not classified as topological since they stay inside the bulk band regions and do not span the topologically non-trivial bandgaps, they have interesting soliton-like shape transitions (a localized mode travels with unaltered shape).

4.4.2 Mode Transitions by Phase Modulations

For mode transitions via phase modulations, the inductance value of s-th pair of electrodes in Eq. 4.5 is updated by adding the phase modulation parameter ϕ:

$$L_s = \frac{1}{C_p \omega_0^2 [1 + \alpha \sin(2\pi s\theta + \phi)]^2}. \tag{4.6}$$

For a given θ value, cyclic modulations of the natural frequencies of the shunt circuits are generated as ϕ changes from 0 to 2π. Two illustrative examples with the same modulation level $\alpha = 0.05$ are presented: one for the bimorph beam made of PMN-PT (33%PT) with $\theta = 0.16$ in Fig. 4.6, and another one for the beam made of PZT-5J with $\theta = 0.13$ in Fig. 4.7. For each case, there exists an edge-localized mode at the right boundary ($x = L$) within the topological band around 325 Hz at $\phi = 0$. When the edge mode branch merges the bulk band around $\phi = 0.5\pi$, the mode changes to bulk mode, and then it localizes at the left boundary ($x = 0$) when the branch detaches from the bulk band. The localization disappears when the branch joins the bulk bands gain around $\phi = 1.5\pi$, and eventually it returns to right-localized mode at $\phi = 2\pi$ as a cycle of phase modulation finishes. Such

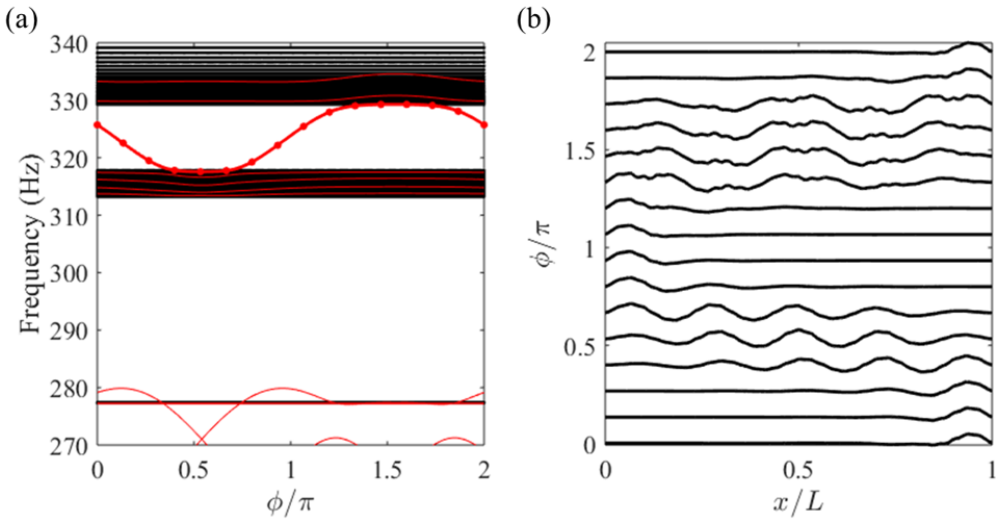

Figure 4.6: Mode transition via phase modulation on electromechanical LR beam with QP inductive shunt circuits (made of PMN-PT with 33% PT, $\alpha = 0.05$, $\theta = 0.16$). (a) Bulk (black) and finite beam (red) spectra as functions of ϕ, where selected branch of modes is tracked and marked by thick red lines. (b) The normalized mode shapes are displayed as a function of ϕ, which correspond to the red dots marked on the selected branch.

transitions can be exploited to produce topological pumping that relies on edge-bulk-edge transitions via adaptive/programmable shunt circuits.

4.5 Numerical Analyses on a Clamped-clamped Piezoelectric Bimorph Beam

The finite system is implemented as a piezoelectric bimorph beam with clamped-clamped boundary conditions, with the excitation applied at $x_f = 645$ mm (middle of the 30-th electrode). The equation of motion for the piezoelectric bimorph beam is modified from Eq. 4.2 to be:

$$D\frac{\partial^4 w(x,t)}{\partial x^4} + m\frac{\partial^2 w(x,t)}{\partial t^2} - \vartheta \sum_s v_s(t)\frac{\mathrm{d}^2}{\mathrm{d}x^2}\Big[H(x-x_s^L) - H(x-x_s^R)\Big] = f(x_f,t). \quad (4.7)$$

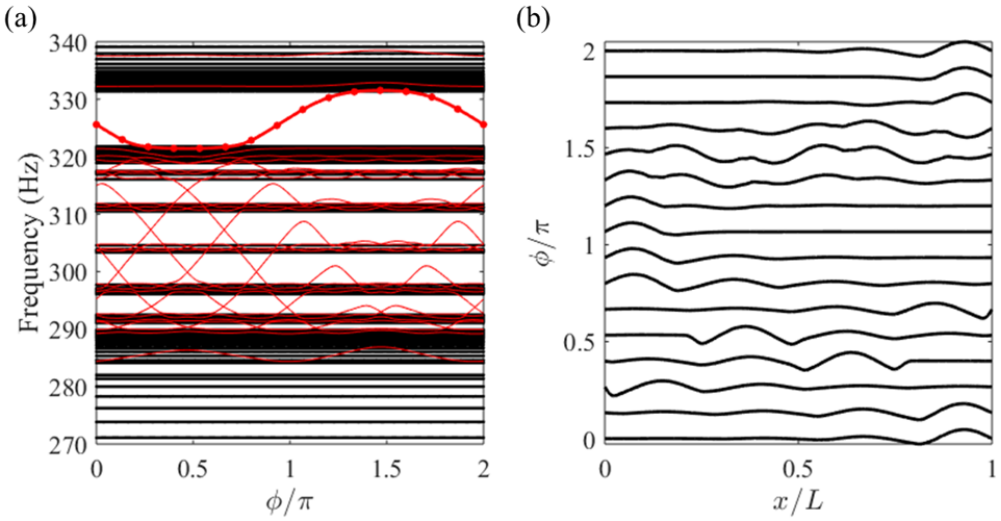

Figure 4.7: Mode transition via phase modulation on electromechanical LR beam with QP inductive shunt circuits (made of PZT-5J, $\alpha = 0.05$, $\theta = 0.13$). (a) Bulk (black) and finite beam (red) spectra as functions of ϕ, where selected branch of modes is tracked and marked by thick red lines. (b) The normalized mode shapes are displayed as a function of ϕ, which correspond to the red dots marked on the selected branch.

Using an assumed-modes type expansion with N modes, the transverse displacement of the bimorph beam can be expanded as:

$$w(x,t) = \sum_{r=1}^{N} \phi_r(x)\eta_r(t), \tag{4.8}$$

where $\eta_r(t)$ are the modal weightings to be obtained. And $\phi_r(x)$ are the mass-normalized mode shapes of the beam obtained for clamped-clamped boundary conditions at short circuit:

$$\begin{aligned}\phi_r(x) = \frac{1}{\sqrt{mL}}\Bigg[&\cosh\left(\frac{\lambda_r x}{L}\right) - \cos\left(\frac{\lambda_r x}{L}\right) \\ &- \left(\frac{\cosh\lambda_r - \cos\lambda_r}{\sinh\lambda_r - \sin\lambda_r}\right)\left(\sinh\left(\frac{\lambda_r x}{L}\right) - \sin\left(\frac{\lambda_r x}{L}\right)\right)\Bigg], \quad r = 1, 2, \cdots, N\end{aligned} \tag{4.9}$$

where λ_r is the r-th positive real solution of the characteristic equation given in:

$$\cos\lambda\cosh\lambda - 1 = 0. \tag{4.10}$$

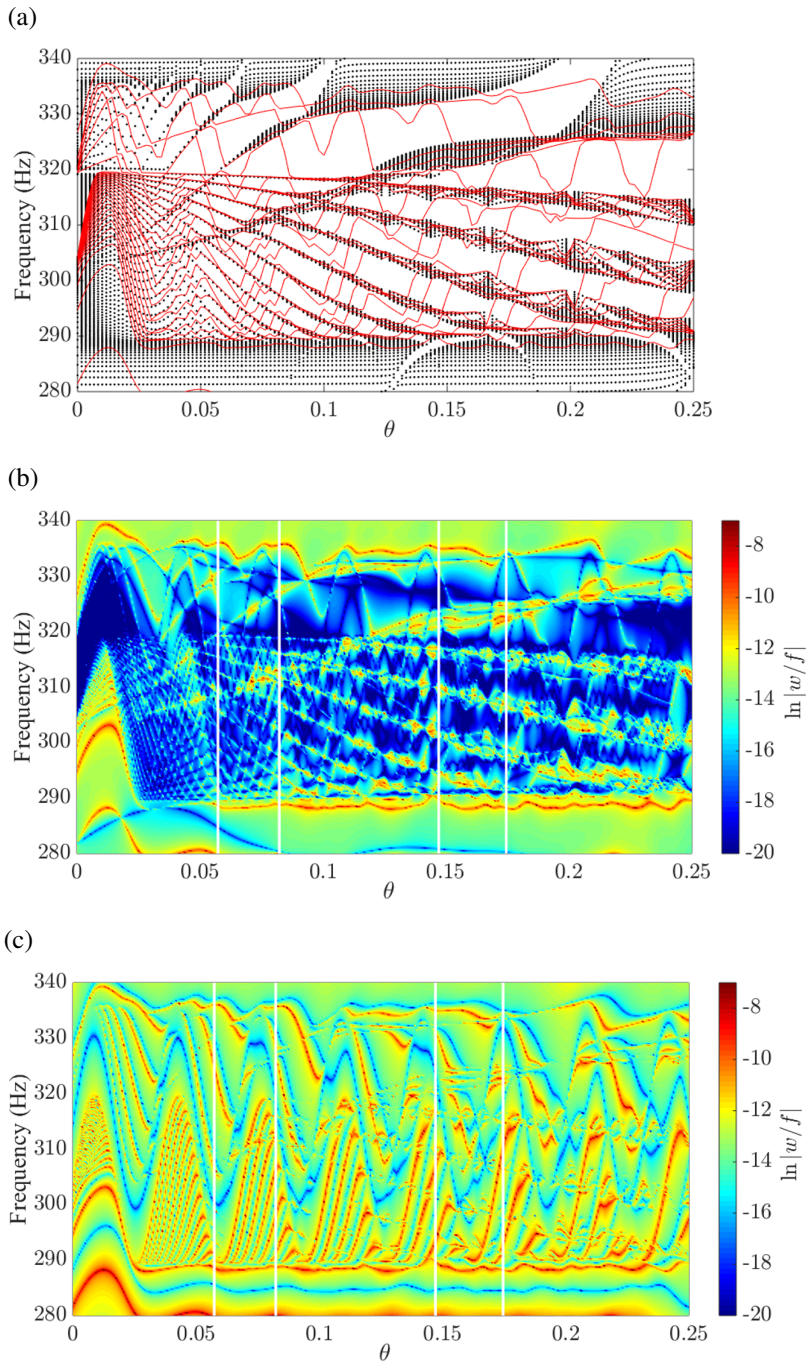

Figure 4.8: (a) Bulk (black) and finite spectra for a clamped-clamped beam with 30 electrode pairs connected to QP inductive shunt circuits (red). (b) Numerical frequency response of the beam spatially averaged between 20-30% of the beam span: the colormap evolving from blue to red corresponds to the log scale of the magnitude. The blue regions highlight the low response ranges corresponding to the bandgaps. (c) Numerical frequency response of the beam spatially averaged between 90-100% of the beam span: the response near the beam end highlights the presence of resonances within the gaps which correspond to edge states. Vertical white lines in (b,c) correspond to the values of $\theta = 0.0599$, $\theta = 0.0823$, $\theta = 0.1471$ and $\theta = 0.1721$ considered in the experiments.

Numerical analyses (Fig. 4.8) are performed to evaluate the presence of the LR bandgap and the additional non-trivial bandgaps, and to guide the selection of θ values in the experiments. Fig. 4.8b plots the frequency response corresponding to the ratio of the beam transverse reflection magnitude to the forcing magnitude as a function of θ, averaged between 20-30$\%$ of the beam length from $x = 0$. The low response regions are shown in blue and highlight the attenuation in the bandgaps. The colormap clearly demonstrates the shift of LR bandgap in the finite beam (correspond to close of the bandgap in the infinite domain) as soon as θ deviates from 0. In addition, the development of the multiple non-trivial bandgaps as θ varies is outlined. On the other hand, Fig. 4.8c, obtained by averaging the response between 90-100$\%$ of the beam length from $x = 0$, highlights the resonances of the finite system.

4.6 Experimental Validation

For the experiments, $\theta = 0.0599$, $\theta = 0.0823$, $\theta = 0.1471$ and $\theta = 0.1721$ are chosen to identify topological bandgaps that are labeled with slopes $m = 1$ and $m = 2$ in Fig. 4.4b. The selected four cases are highlighted in white lines in Fig. 4.8b and Fig. 4.8c for reference. The experimental investigations are described next to validate the existence of topologically non-trivial bandgaps and the occurrence of edge states.

4.6.1 Experimental Setup

The experimental setup displayed in Fig. 4.9 shows the piezoelectric bimorph beam made of a 2024 aluminum central substrate (shim) and the piezoceramic PZT-5J patches. The shim is 660 mm long, 21 mm wide and 0.508 mm thick. Each piezo patch has dimensions 21 mm $\times$ 21 mm $\times$ 0.55 mm. The piezo patches are vacuum bonded to the aluminum shim with epoxy to minimize the thickness of the bonding layer. The space between the adjacent piezo patches is 1 mm. All the piezo patches are bonded with the same poling orientation for parallel connection: the aluminum shim is electrically grounded, and the

(a)

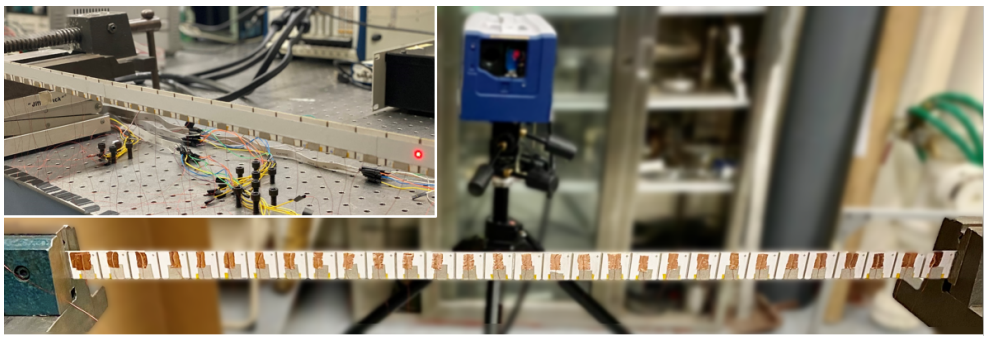

(b)

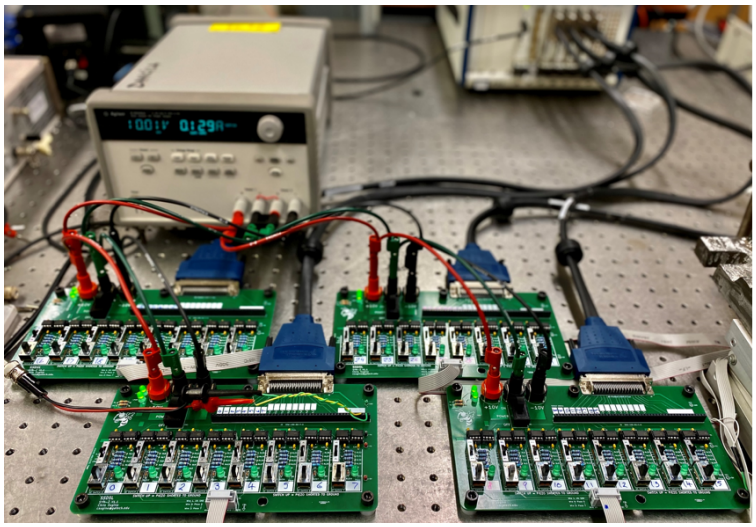

Figure 4.9: Experimental setup for electromechanical QP metastructure: a piezo bimorph beam (clamped on both ends) with 30 pairs of identical piezoceramic PZT-5J patches. The velocity field is measured by a scanning laser Doppler vibrometer (SLDV). (a) Rear view of the beam facing the SLDV with an insertion of close-up of the front view. The 30-th pair of piezo patches (near the green clamp) is used to excite the beam. The remaining 29 pairs are connected to synthetic impedance shunt circuits that are digitally programmed to have quasiperiodic inductance values. (b) Synthetic impedance circuits on printed circuit boards.

opposing electrodes of each pair of patches are short circuited. It is worth noting that, the experimental system is different from the system considered in Section 4.2 since the beam is made of separately bonded pairs of piezoceramic patches instead of two continuous piezoceramic layers. Consequently, it is expected for the system to have a reduced effective electromechanical coupling since there exists stiffness mismatch between the bonded and non-bonded areas of the aluminum shim. The capacitance of each pair of piezo patches is

Table 4.2: Measured capacitance values for the piezoelectric bimorph. Piezo pairs $1-29$ are connected to synthetic impedance circuits, while piezo pair 30 is used for excitation.

Pair Index	Capacitance (nF)	Pair Index	Capacitance (nF)
1	24.83	16	24.91
2	25.96	17	24.56
3	23.16	18	23.98
4	24.56	19	23.70
5	26.20	20	24.46
6	26.14	21	24.07
7	23.00	22	24.49
8	23.83	23	24.48
9	23.95	24	24.36
10	24.36	25	23.59
11	24.82	26	24.30
12	25.24	27	23.80
13	23.98	28	23.16
14	24.79	29	23.23
15	24.79	30	23.30

measured using a capacitance meter and listed in Table. 4.2.

The beam is clamped on both ends with 0.5 mm from the the first and last (30-th) pair of piezo patches to the clamps, respectively. The beam is actuated with the 30-th pair of piezo patches that is located next to the green clamp (first pair from the left in Fig. 4.9a). The remaining 29 pairs of piezoceramic patches are connected to synthetic impedance shunt circuits that are programmed digitally to have quasiperiodic inductance values. The velocity field of the beam is measured using a scanning laser Doppler vibrometer (SLDV) over a grid of 93 points along the beam length, corresponding to a spatial resolution of 7.10 mm.

Synthetic Impedance Shunts

Shunt circuits using synthetic impedance are very flexible in obtaining the desired admittance, which can be realized by a digital transfer function implemented on a controller. The synthetic impedance for piezoelectric shunts was originally introduced by Fleming et at [86]. The synthetic impedance circuit based on the Howland current pump (HCP) [87],

applied by Sugino et al. [19], is utilized here in the experimental setup. The detailed schematic of the synthetic impedance circuit on the printed circuit boards (PCB) for a single pair of electrode is shown in Fig. 4.10. All the operational amplifiers (op-amps) are assumed to be ideal, such that the output current of the circuit is:

$$i(t) = \frac{v_{out\_\mathrm{DSP}}(t)}{R_c}. \tag{4.11}$$

For any desired admittance relationship between the piezoelectric voltage $v_s(t) = v_{p\_\mathrm{in}}(t)$ and the supplied current $i(t)$, a transfer function $F(s)$ that relates the output voltage $v_{out\_\mathrm{DSP}}(t)$ to the piezoelectric voltage $v_{p\_\mathrm{in}}(t)$ is needed:

$$F(s) = \frac{V_{out\_\mathrm{DSP}}(s)}{V_{p\_\mathrm{in}}(s)}, \tag{4.12}$$

where $V_{out\_\mathrm{DSP}}(s)$ and $V_{p\_\mathrm{in}}(s)$ correspond to $v_{out\_\mathrm{DSP}}(t)$ and $v_{p\_\mathrm{in}}(t)$ in Laplace domain respectively. In addition, the effective admittance in Laplace domain is:

$$Y(s) = \frac{I(s)}{V_{p\_\mathrm{in}}(s)} = \frac{F(s)}{R_c}, \tag{4.13}$$

where R_c is a reference resistor. In the experiment, the reference resistor can be switched between different values on the PCB. Equation 4.13 relates the transfer function $F(s)$ to any desired admittance $Y(s)$, or specifically any desired inductance in this study. For the continuous-time transfer function $F(s)$ to be implemented digitally, corresponding discrete filter $F(z)$ needs to be uploaded to the controller. For this experimental setup, the controller utilized a field-programmable gate array (FPGA) with 32 input and output channels operating at 400 kHz. The FPGA is programmed in National Instruments LabVIEW to enable the real-time control of the digital filter transfer function coefficients for any desired inductance according to the QP pattern in Eq. 4.5.

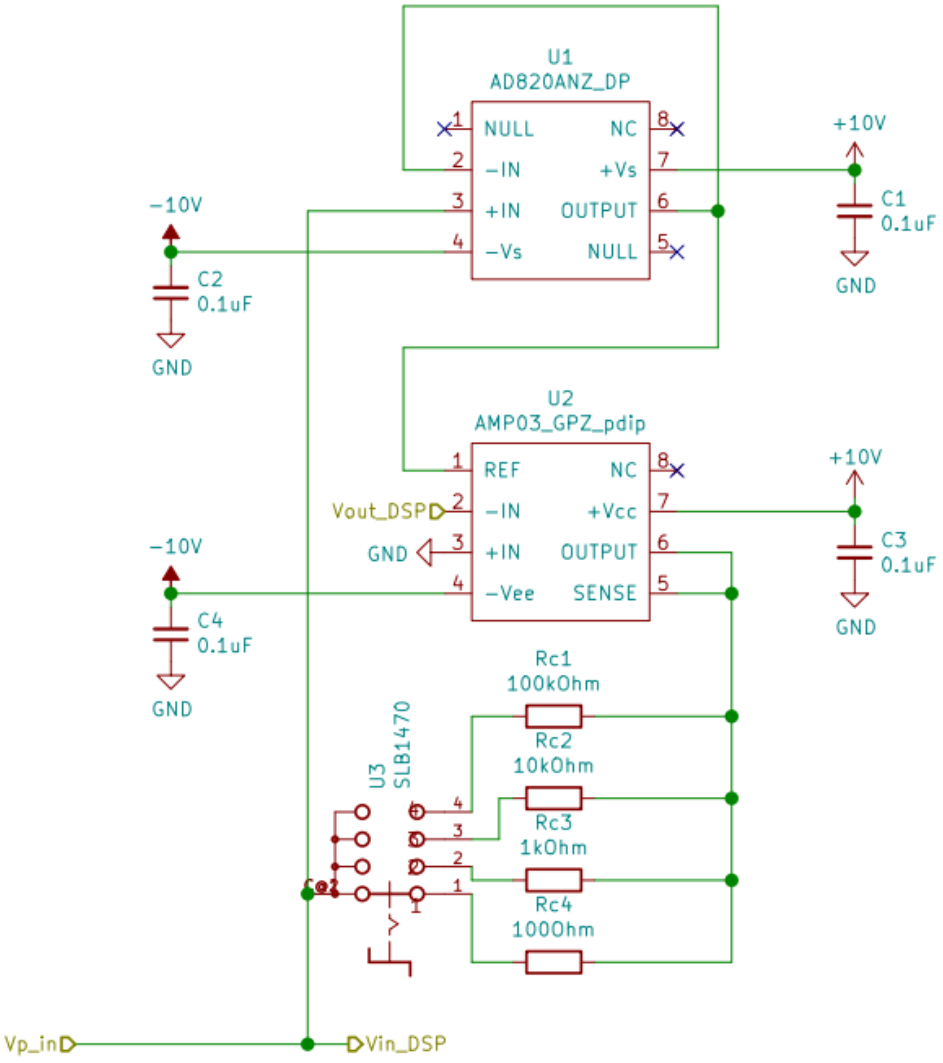

Figure 4.10: Schematic of detailed circuit on the PCB for the synthetic impedance circuit for a single electrode pair. The wire connected to the two electrodes is connected to v_{p_in} in the circuit, and the central substrate is connected to GND. The input to the digital signal processor is measured between v_{in_DSP} and GND, while the analog output is connected between v_{out_DSP} and GND.

4.6.2 Experimental Results

Figure 4.11 shows the experimental frequency response averaged between 20% and 30% of the beam span from $x = 0$, i.e., away from the excitation location, for $\theta = 0.0599$, $\theta = 0.0823$, $\theta = 0.1471$, and $\theta = 0.1721$. The topological bandgaps with slope $m = 1$ and $m = 2$ (labeled in the IDS colormap in Fig. 4.4b) are identified in the selected cases. The center frequency of each topological bandgap varies as the QP patter parameter θ changes. Overall, the frequency location and frequency width of these bands agree with the theoretical predictions shown as green ($m = 1$) and blue ($m = 2$) shaded areas.

Furthermore, the presence of the edge-localized modes is observed for both $\theta = 0.0599$ and $\theta = 0.1721$ in the topological bandgaps $m = 2$ and $m = 1$, respectively. Experimental frequency response of the beam and measured spatial distributions of selected mode shapes are shown in Fig. 4.12b-d for $\theta = 0.0599$ and in Fig. 4.13b-d for $\theta = 0.1721$. The averaged frequency response near the end of the beam (i.e., between 90% and 100% of the beam span from $x = 0$) shows the existence of the localized modes which correspond to the response peaks with in the topological bandgaps highlighted in Figs. 4.12c and 4.13c. As expected from the numerical simulations, the measured modes (blue square) for each case that appear in the topological bandgaps are localized at the right boundary (close to $x = L$), confirmed by the corresponding deflection shapes plotted in blue and labeled 'II' in Figs. 4.12d and 4.13d. For comparison, for each θ value, two bulk modes labeled 'I' and 'III' at frequencies before and after the topological bandgap, respectively, are presented to demonstrate their global deflection shapes.

Numerical simulations predict the edge states to decrease exponentially, however the localized modes measured in the experiments are weakly evanescent. The discrepancies can be caused by the following reasons. First, the overall effective electromechanical coupling of the actual beam is smaller than the ideal beam considered in the simulations. Instead of the continuous piezoceramic layers with segmented electrodes being bonded perfectly to the substrate (negligible bonding thickness), the discrete piezoceramic patches are bonded

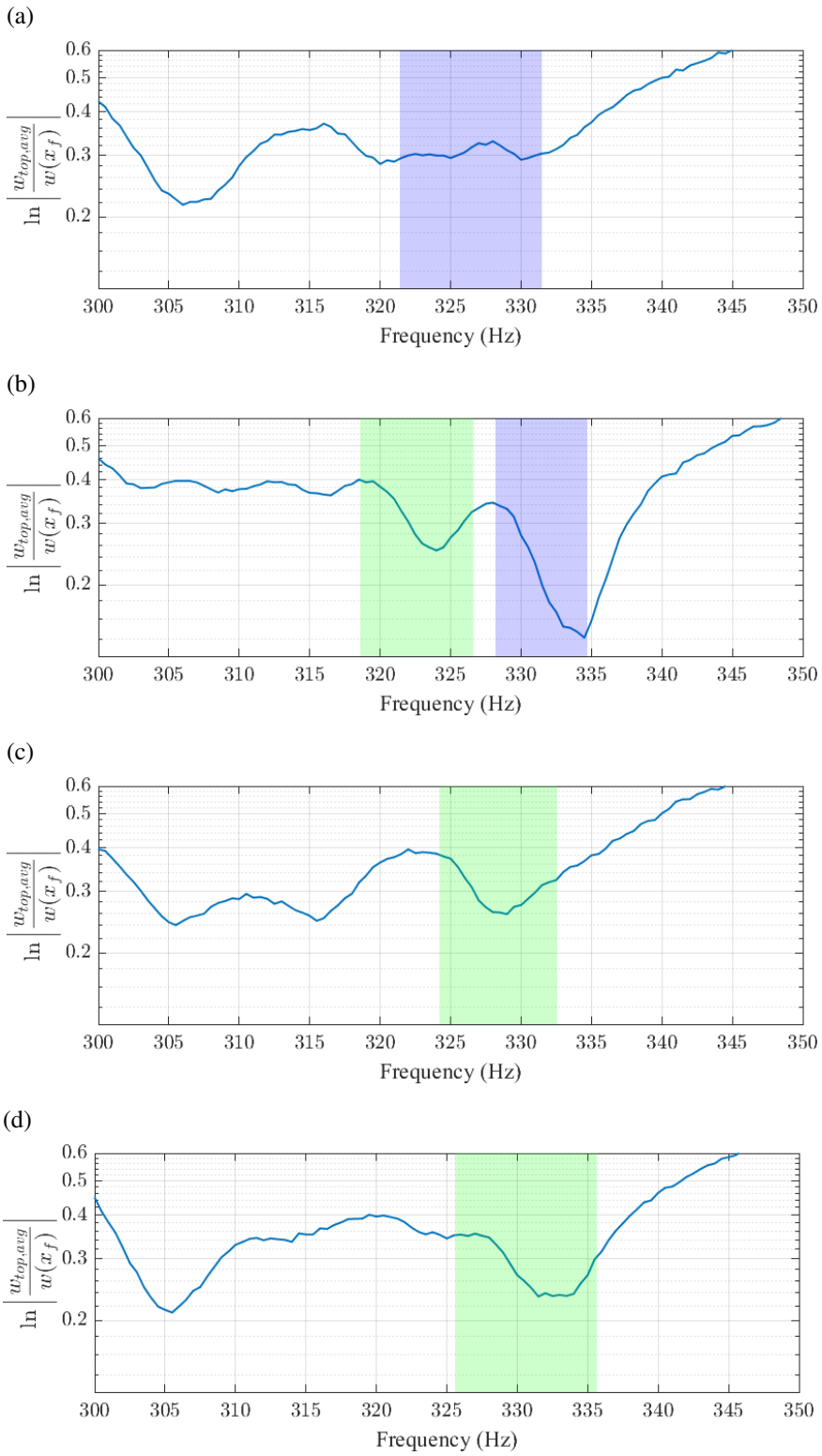

Figure 4.11: Experimental results of the beam frequency response (spatially averaged between 20% and 30% of beam span) for selected θ values: (a) $\theta = 0.0599$, (b) $\theta = 0.0823$, (c) $\theta = 0.1471$, and (d) $\theta = 0.1721$. Green and blue shaded regions highlight the topologically non-trivial bandgaps labeled with $m = 1$ and $m = 2$ in the IDS plot in Fig. 4.4b respectively.

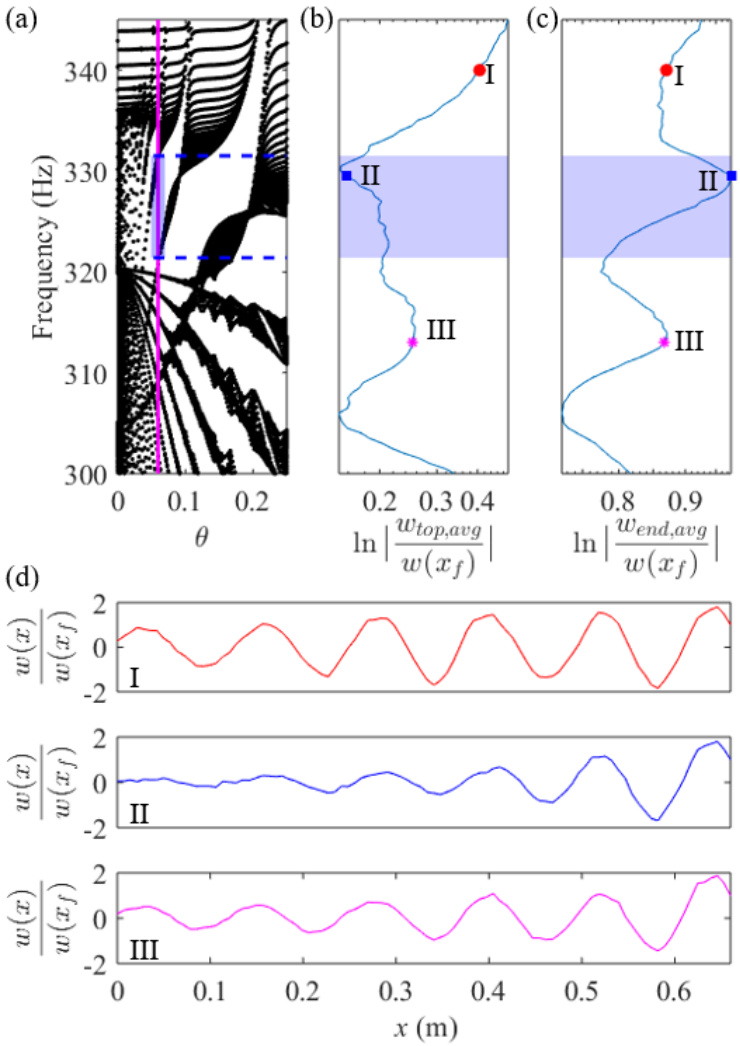

Figure 4.12: (a) Detail of numerical bulk spectrum with vertical magenta lines corresponding to $\theta = 0.0599$. The blue dashed lines show the theoretical boundaries of the non-trivial topological bandgap with slope $m = 2$ as labeled in Fig. 4.4b. (b-d) Experimental results for $\theta = 0.0599$. Magnitude of beam frequency response spatially averaged between 20% and 30% (b), 90% and 100% (c) of beam span. Blue shaded areas highlight the theoretical topological bandgap $m = 2$. (d) Measured deflection shapes of the beam. Modes 'I' and 'III' are bulk modes at frequencies before and after the topological bandgap $m = 2$, respectively. The corresponding frequencies are marked by the red circle and magenta asterisk in (b,c). The mode labeled as 'II' in (d) is edge-localized, and its frequency falls in the topologically non-trivial gap, and it is marked by blue square in (c).

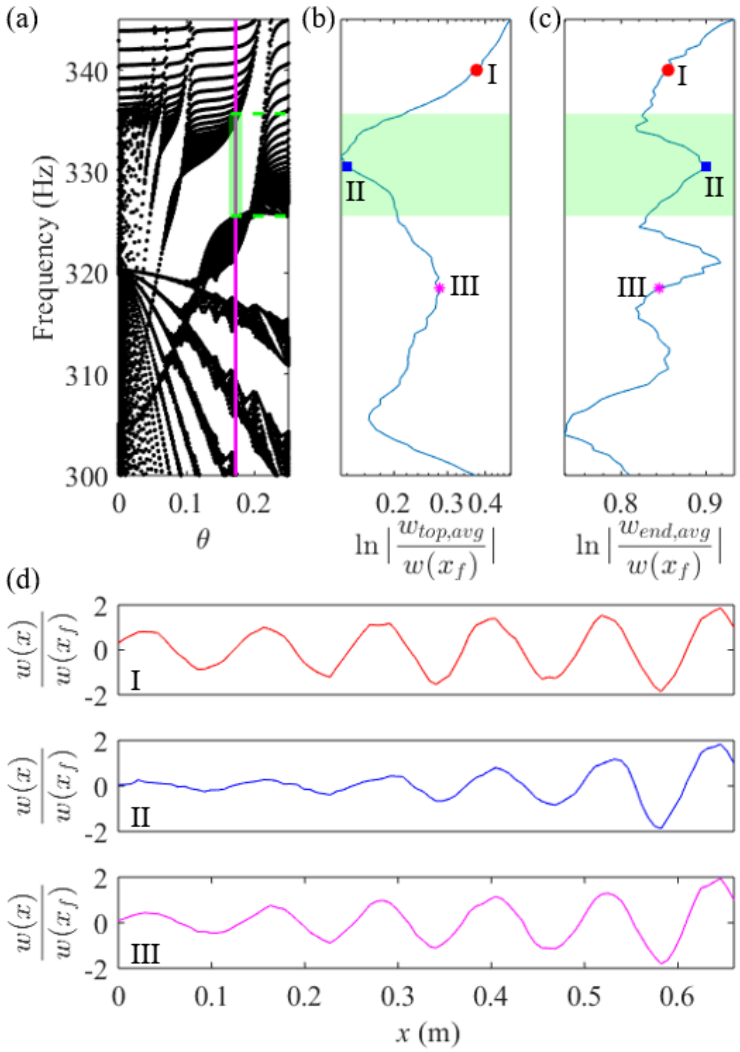

Figure 4.13: (a) Detail of numerical bulk spectrum with vertical magenta lines corresponding to $\theta = 0.1721$. The green dashed lines show the theoretical boundaries of the non-trivial topological bandgap with slope $m = 1$ as labeled in Fig. 4.4b. (b-d) Experimental results for $\theta = 0.1721$. Magnitude of beam frequency response spatially averaged between 20% and 30% (b), 90% and 100% (c) of beam span. Green shaded areas highlight the theoretical topological bandgap $m = 1$. (d) Measured deflection shapes of the beam. Modes 'I' and 'III' are bulk modes at frequencies before and after the topological bandgap $m = 1$, respectively. The corresponding frequencies are marked by the red circle and magenta asterisk in (b,c). The mode labeled as 'II' in (d) is edge-localized, and its frequency falls in the topologically non-trivial gap, and it is marked by blue square in (c).

to the aluminum shim with slightly varying bonding thickness, leading to different capacitance values. Secondly, mechanical components such as the the bonding layers, non-ideal clamps, and the copper tape and wires soldered on the piezo patches add damping to the whole system. Thirdly, damping can come from electrical components such as the non-ideal op-amps and resistors used in the experiments. In addition, the last (30-th) pair of piezo patches is used to excite the beam and not connected to an inductive shunt circuit, differing from the beam utilizing all 30 pairs of electrodes with QP inductive shunt circuits in simulations.

4.7 Conclusions

This chapter investigates electromechanical locally resonant metastructures in the form of piezoelectric bimorph beams with quasiperiodic inductive shunt circuits. By varying the parameter θ defining the natural frequencies of the resonant shunt circuits, topologically non-trivial bandgaps are created besides the typical electromechanical locally resonant bandgap. Some of the topological edge-localized modes can evolve to interior-localized modes in the finite structure as θ varies. In addition, by introducing phase modulation ϕ to the quasiperiodic pattern generation, the localized mode at one boundary can be shifted to the other boundary through edge-bulk-edge transitions for a given θ. Finally, experimental validations on the existence of topological bandgaps and associated edge-localized modes are performed using a piezoelectric bimorph beam with 30 pairs of separately bonded piezoceramic patches, along with fabricated synthetic impedance circuits that are digitally controlled to provide quasiperiodic inductance values.

CHAPTER 5
TEMPORAL TOPOLOGICAL PUMPING IN AN ELECTROMECHANICAL METASTRUCTURE

5.1 Introduction

The mode transitions in mechanical and electromechanical locally resonant metastructures were demonstrated in Chapter 3 and Chapter 4, respectively. However, the investigations of mode transitions have been limited to numerical analyses. In this chapter, the investigation focuses on the experimental demonstration of mode transitions through phase modulation. More specifically, this chapter studies temporal pumping of elastic waves in an electromechanical waveguide with stiffness modulation. The dispersion properties of the bands and non-trivial edges states are evaluated numerically. The experimental demonstration is conducted on an aluminum beam covered by an array of piezoelectric patches connected to negative capacitance shunt circuits with digitally controllable resistances, which enables the spatial and temporal control of the beam's stiffness. A smooth temporal variation of the modulation phase transfers edge states from one boundary of the metastructure to the other in a controllable manner.

5.2 Spatio-temporal Modulation in a Piezoelectric Bimorph Beam with Negative Capacitance Shunt Circuits

The system is considered to be a piezoelectric bimorph beam, which is made of a central substrate (shim) and an array of piezoceramic patches bonded in pairs on both sides of the shim and shunted through negative capacitance (NC) circuits as shown in Fig. 5.1 [88]. The NC shunts modify the equivalent bending stiffness D according to the following modula-

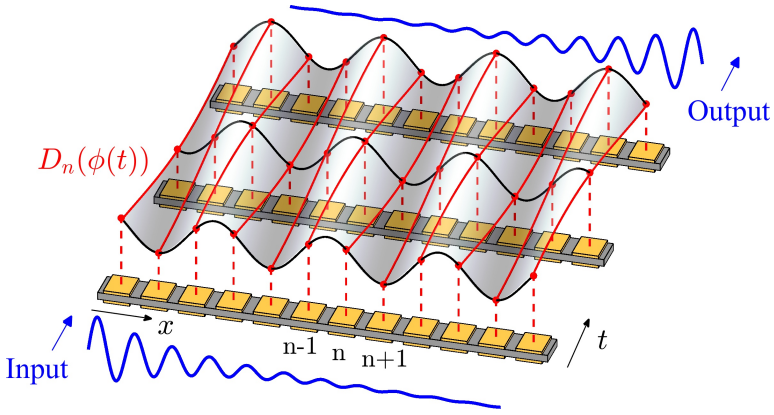

Figure 5.1: Concept of temporal pumping implemented in a piezoelectric bimorph beam. The equivalent stiffness $D_n(\phi)$ at the location of the n-th pair of piezoelectric patches (red lines) is obtained by sampling the surface $D(x,\phi) = D_0[1+\alpha\cos(2\pi\theta x+\phi)]$ at $x_n = n$ [70]. The spatial stiffness modulation with slowly varying temporal phase $\phi(t)$ induces the transition of the left-localized edge state (input) into a right-localized state (output).

tion:

$$D_n(\phi) = D_0[1+\alpha\cos(2\pi n\theta+\phi)], \tag{5.1}$$

where D_n is the contribution to the bending stiffness at the location of the n-th pair of piezo patches (Fig. 5.1). The parameter θ controls the periodicity of the structure: rational values of θ produce periodic domains, while irrational θ values result in quasiperiodic or incommensurate domains. For a given θ, the spatial stiffness modulation can produce edge states localized at one of the boundaries of the finite beam depending on the assigned value of the modulation phase ϕ [70]. An adiabatic temporal modulation of the phase $\phi(t)$ can drive a left-localized edge state (input) across the beam producing a right-localized state (output), thus implementing topological pumping.

Wave motion along the bimorph beam is predicted by employing Euler–Bernoulli beam theory [89], which describes the transverse harmonic motion at $w(x,\omega)$ of the waveguide through the following governing equation:

$$[D(x)w_{,xx}]_{,xx} = \omega^2 m(x)w(x,\omega), \tag{5.2}$$

where $[]_{,x}$ denotes a derivative with respect to x, and m is the linear mass density of the beam. Because of the presence of the patches, stiffness and inertia properties are periodic functions of x, and can be expressed as:

$$D(x) = D_b + \sum_n D_n H(x - nx_p, l_p), \tag{5.3a}$$

$$m(x) = m_b + \sum_n m_p H(x - nx_p, l_p), \tag{5.3b}$$

where D_n is given in Eq. 5.1, D_b, m_b respectively denote the bending stiffness and linear mass density of the central substrate, and m_p is the increase in linear mass density at the locations of the patches. In addition, $H(\cdot)$ is a unit step function centered at location nx_p and of length l_p.

For the following numerical analyses, a modulation with $\theta = 1/3$ in Eq. 5.1 is considered, resulting in a periodic beam, whose period $L_c = 72$ mm comprises 3 piezoelectric elements of length $l_p = 22$ mm, that are 2 mm apart. The variable resistance NC shunts produce a stiffness modulation that is quantified by a value of $\alpha = 0.172$. All these values are in accordance with the experimental setup described later in Section 5.4, where details about the system geometrical and physical parameters are described.

5.3 Numerical Analyses

In this section, the study on both the dispersion properties and edge states of the stiffness-modulated piezoelectric bimorph beam is conducted.

5.3.1 Dispersion Properties

The dispersion properties $\omega(\kappa, \phi)$ of the stiffness-modulated bimorph beam are evaluated by employing a finite element discretization of Eq. 5.2 and the application of Bloch conditions on a unit cell [90], i.e., $w(\omega, x + L_c) = w(\omega, x)e^{-i\kappa L_c}$, where κ is the wavenumber. The resulting eigenvalue problem can be written in terms of reduced mass and stiffness

matrices $\boldsymbol{M}_r(\mu)$, $\boldsymbol{K}_r(\phi,\mu)$ [90]:

$$\boldsymbol{K}_r(\phi,\mu)\,\boldsymbol{w} = \omega^2 \boldsymbol{M}_r(\mu)\,\boldsymbol{w}, \tag{5.4}$$

where $\mu = \kappa L_c$ is the normalized wavenumber and $\boldsymbol{w}$ is the displacement vector. Figure 5.2 displays a representative result of solving the eigenvalue problem as a function of μ for $\phi = 0$, where the first five dispersion bands are shown.

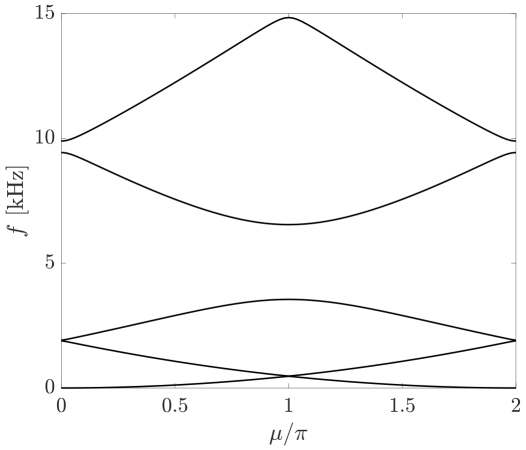

Figure 5.2: Dispersion bands (first five bands) of the modulated bimorph beam for $\phi = 0$.

The consideration of the virtual parameter ϕ augments the dispersion bands to be defined over a two-dimensional torus $[\mu, \phi] \in [0, 2\pi]$, where the Chern number becomes the relevant topological invariant [91, 70, 71]. The dispersion is then computed within the $(\mu, \phi) \in T^2 = [0, 2\pi] \times [0, 2\pi]$ domain and displayed in Fig. 5.3. The analysis of the band's topology relies on the evaluation of the associated Chern numbers, which is expressed as:

$$C = \frac{1}{2\pi i} \int_D \nabla \times (\boldsymbol{w}^* \cdot \nabla \boldsymbol{w})\, dD, \tag{5.5}$$

where $D = T^2$, $\nabla = (\partial/\partial\mu)\,\boldsymbol{e}_\mu + (\partial/\partial\phi)\,\boldsymbol{e}_\phi$ and $()^*$ denotes a complex conjugate. The Chern number C is practically determined following the procedure discussed in [92], yielding $C_1 = 1$, $C_2 = -2$, and $C_3 = 1$ for the first three bands of Fig. 5.3a. Such bands are separated by narrow bandgaps (red shaded volumes), for which gap labels are obtained by

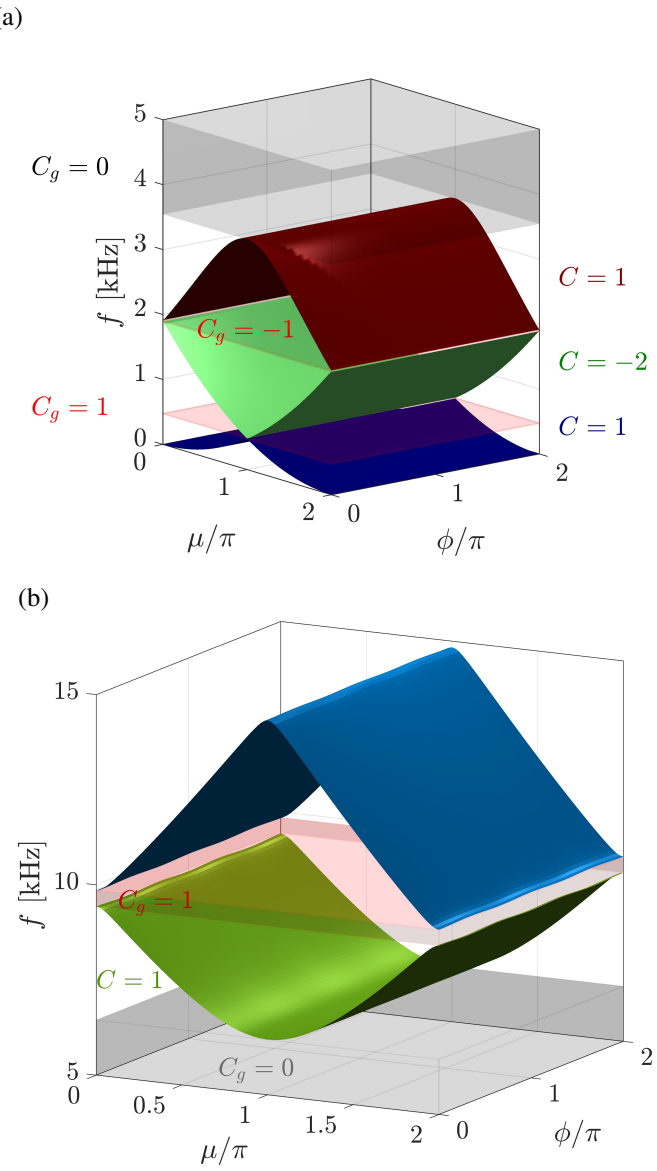

Figure 5.3: Dispersion surfaces as a function of μ and ϕ with information on Chern numbers and gap labels. (a) Close-up on the frequency range of the first three bands ($0-5$ kHz). (b) Close-up on the frequency range of the fourth and fifth bands ($5-15$ kHz). Red shaded volumes highlight the non-trivial gaps, while the trivial gap is highlighted in gray shaded volume.

the algebraic sum of the Chern number of the bands below it, i.e., $C_g^{(r)} = \sum_{n=1}^{r} C_n$ for the gap r. As a result, the first two gaps have $C_g^{(1)} = 1$ and $C_g^{(2)} = -1$, respectively. Although these gaps are non-trivial, they are very narrow and of little practical relevance, which motivates the exploration of the fourth gap separating the fourth and fifth bands. To be noticed, the larger gap (third gap) in the band structure is topologically trivial with

$C_g^{(3)} = 0$ (shaded gray volume in Figs. 5.3a,b). Figure 5.3b depicts two dispersion surfaces for fourth and fifth bands as a function of ϕ and $\mu = \kappa L_c$, which are separated by a gap (fourth gap of the structure) of center frequency close to 9.7 kHz. Evaluation of the Chern number results in $C_4 = 1$ for the fourth band. The non-zero label $C_g^{(4)} = 1$ of the gap in Fig. 5.3b indicates its ability to support an edge state spanning the gap in a finite structure [70, 71].

5.3.2 Topological Edge States

To investigate the existence of topological edge modes spanning the non-trivial gap, the eigenfrequencies of a finite beam are computed. To this end, the finite element discretization is employed to a finite structure to obtain the following eigenvalue problem:

$$\boldsymbol{K}(\phi)\,\boldsymbol{w} = \omega^2 \boldsymbol{M}\boldsymbol{w}, \tag{5.6}$$

where $\boldsymbol{K}(\phi)$ denotes the stiffness matrix that varies with ϕ due to the modulation of the patches, while $\boldsymbol{M}$ is the mass matrix. Eigenfrequencies of a finite beam of length $L = 57.6$ cm, comprising 8 unit cells for a total of 24 pair of patches are computed. For simplicity, simply supported boundary conditions are considered for the calculation, while a more accurate model is introduced later to fit the experimental data. Figure 5.4a displays the variation of the eigenfrequencies as a function of ϕ (black lines), superimposed to the bulk bands represented by the shaded gray areas. The additional mode spanning the non-trivial gap is an edge state, where dashed (solid) lines are used for values of ϕ corresponding to left (right) localized modes. The three representative modes marked in Fig. 5.4a are displayed in Fig. 5.4b to illustrate a transition of the edge state from right-localized (I), to bulk (II), and then to left-localized (III) for increasing ϕ values. Such transition is hereafter employed to induce edge-to-edge pumping through a smooth modulation of ϕ in time.

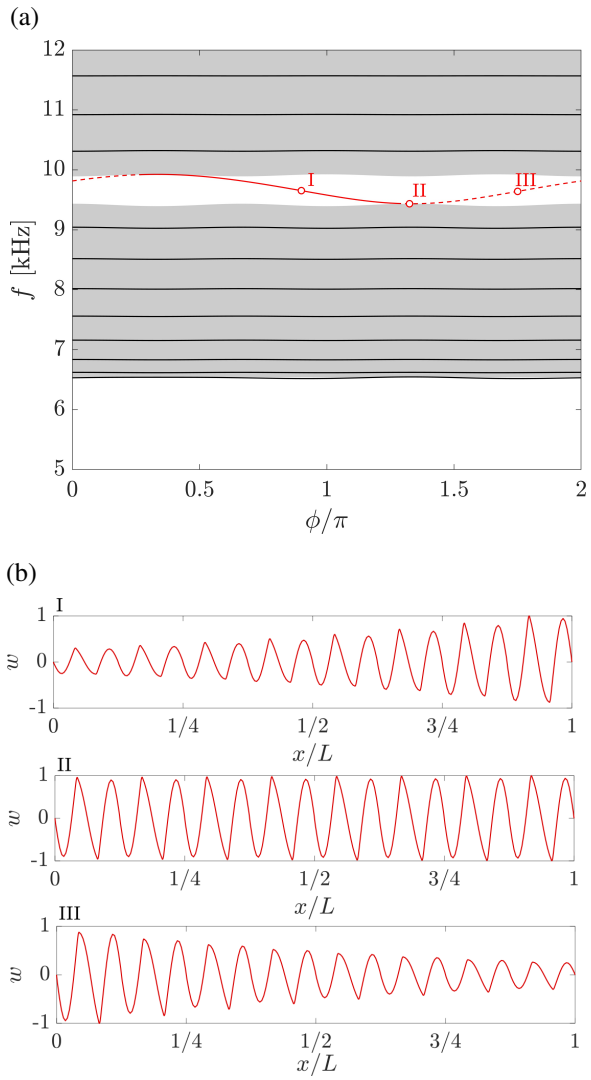

Figure 5.4: Edge states for a beam with equivalent stiffness modulation $D_n(\phi) = D_0[1 + \alpha\cos(2\pi\theta n + \phi)]$. (a) Eigenfrequencies for a finite beam as a function of ϕ (black lines) superimposed to the bulk bands (shaded gray regions), where an edge state (red line) spans the non-trivial gap with $C_g = 1$. (b) States corresponding to the points marked in (b) showing examples of right-localized mode (I), bulk mode (II) and left-localized mode (III).

5.4 Experimental Validation

Experimental investigations have two goals: first is to characterize the beam spectrum as a function of modulation phase ϕ and find the corresponding edge states; second is to induce topological pumping by imposing a smooth temporal variation of ϕ.

(a)

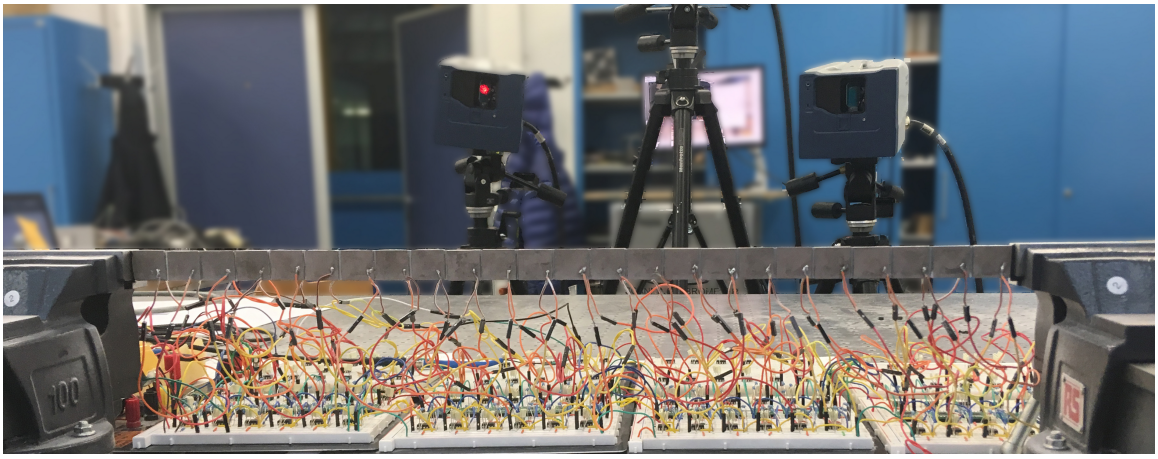

(b)

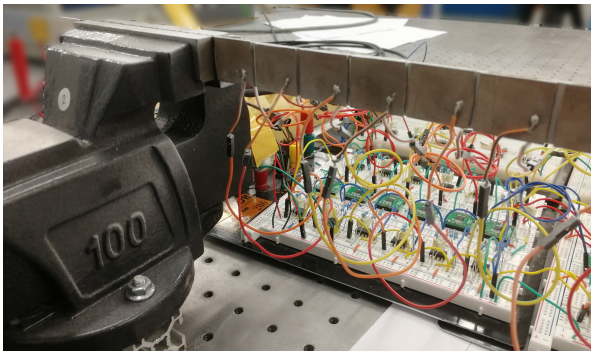

(c)

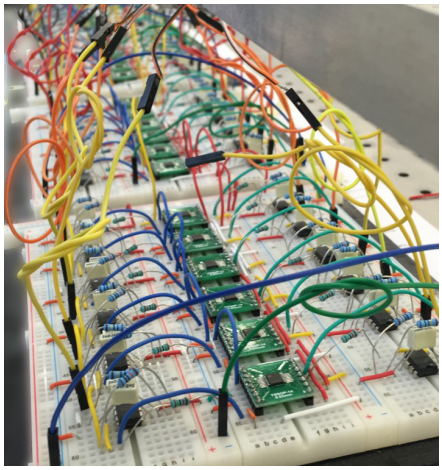

Figure 5.5: Experimental setup of the spatio-temporal modulated electromechanical system. (a) Rear view of the beam facing the 3D SLDV. (b) Zoomed view of the left clamp. (c) Close-up of the NC circuits.

5.4.1 Experimental Setup

Figure 5.5 displays the experimental setup. The electromechanical system as a piezoelectric bimorph beam illustrated in Fig. 5.5a is made of a plain aluminum beam of thickness $H = 1$ mm partially covered by an array of piezoelectric patches of dimensions $l_p \times h_p \times b = 22 \times 1 \times 20$ mm, spaced by a passive layer of length $l_s = 2$ mm, for a total of $N = 24$ pairs. Each patch is mechanically bonded and electrically grounded to the substrate though a conductive epoxy CW2400, whereby the electrode in contact with the beam is characterized by zero potential. The external electrode is connected to a NC circuit, which

is able to induce a stiffness modulation in the layered structure via feedback control. A detailed view of the electrical circuit is shown in Fig. 5.5c. The electromechanical system is equipped with two clamps in correspondence of the left and right boundaries of the beam and mounted on an optical table to minimize the influence of noise coming from ambient vibrations. Each clamp is electrically separated from the beam through a plastic tape in order to avoid undesired current loops between the electrical ground of the laboratory and the reference potential of the system, which is electrically connected to the piezo electrode in contact with the substrate. During the experiments, an input signal is imposed at either the left or right boundary by exciting one of the patches close to the corresponding clamp. The electrical input signal is provided through a KEYSIGHT 33500B waveform generator and a HVT-500N piezo amplifier. The out-of-plane velocity field is measured through a 3D scanner laser Doppler vibrometer (SLDV). Two different forcing signals are considered: (a) a broadband noise excitation filtered within $3 - 15$ kHz, and (b) a mono-harmonic excitation centered at 9.45 kHz.

Negative Capacitance Circuits

The schematic of the circuit is shown in Fig. 5.6a, which illustrates that individual NC shunt is made of an operation amplifier (OPA445), a digital resistor R_1 (AD5207), two passive resistors R_2, R_0, and a capacitor C. In this case, the shunted Young's modulus of the patch is expressed as:

$$E_p^{SU} = \frac{C_N - C_p^T}{C_N - C_p^S}, \tag{5.7}$$

where $C_N = C/r$, $r = R_1/R_2$, and $C_p^{T,S}$ denotes the capacitance of the piezoelectric patch under stress (T) and strain (S) free conditions. The expression in Eq. 5.7 describes a frequency-independent value for the Young's modulus, only valid for a sufficiently high bias resistance R_0 [88]. It is sufficiently accurate for the scope of this work and the value of R_1 is exploited as a tunable knob to achieve the desired stiffness modulation. Variable resistors are employed for this purpose, which are digitally controlled in real-time through

Table 5.1: Parameters for the negative capacitance circuits

Symbol	Description	Value	Unit
R_1	Variable resistance	$0 - 7.4$	kΩ
R_2	$-$	13.7	kΩ
R_0	Bias resistance	100	kΩ
C	NC capacitance	4.4	nF
C_p	Piezo patch capacitance	7	nF
d_{31}	Piezo strain coefficient	-1740	pm/V
k_{31}	Piezo coupling coefficient	0.351	$-$

a LabView Compact-RIO equipped with NI9402 high-speed modules which are synchronized with the measurement system and the excitation. The relationship between E_p^{SU} and R_1 values is illustrated in Fig. 5.6b, computed through Eq. 5.7 considering the discrete set of values available for R_1. The relevant circuits parameters are summarized in Table 5.1.

Under these conditions, the Young's modulus of the patch can be controlled spanning a range within $E_p^{SU} \in [E_{p,MIN}^{SU}, E_{p,MAX}^{SU}]$, which reflects on an equivalent Young's modulus at the region of the piezoelectric patch that accounts for the passive and the active layers:

$$E_{eq} = \frac{E_b I_b + 2E_p^{SU} I_p}{I_b + 2I_p}, \tag{5.8}$$

where

$$I_b = \frac{bH^3}{12}, \quad I_p = \frac{bh_p^3}{12} + bh_p \left(\frac{H}{2} + \frac{h_p}{2}\right)^2, \tag{5.9}$$

while $E_b = 70$ Gpa is the Young's modulus of the base beam, I_p and I_b are the cross-sectional moment of inertia at the location of the patches and of the base beam, respectively. Similarly, the equivalent density at the location of the patch is $\rho_{eq} = (\rho_b A_b + 2\rho_p A_p)/(A_b + 2A_p)$, where $\rho_b = 2700$ kg/m^3 and $\rho_p = 7900$ kg/m^3 respectively denote the mass density of the base beam (aluminum) and of the patch, while A_b and A_p are the associated cross-sectional areas. The linear mass density $m = \rho(x)A(x)$ of the beam as expressed in Eq. 5.3b is given by $m_b = \rho_b A_b$ as the base level, with an increase of

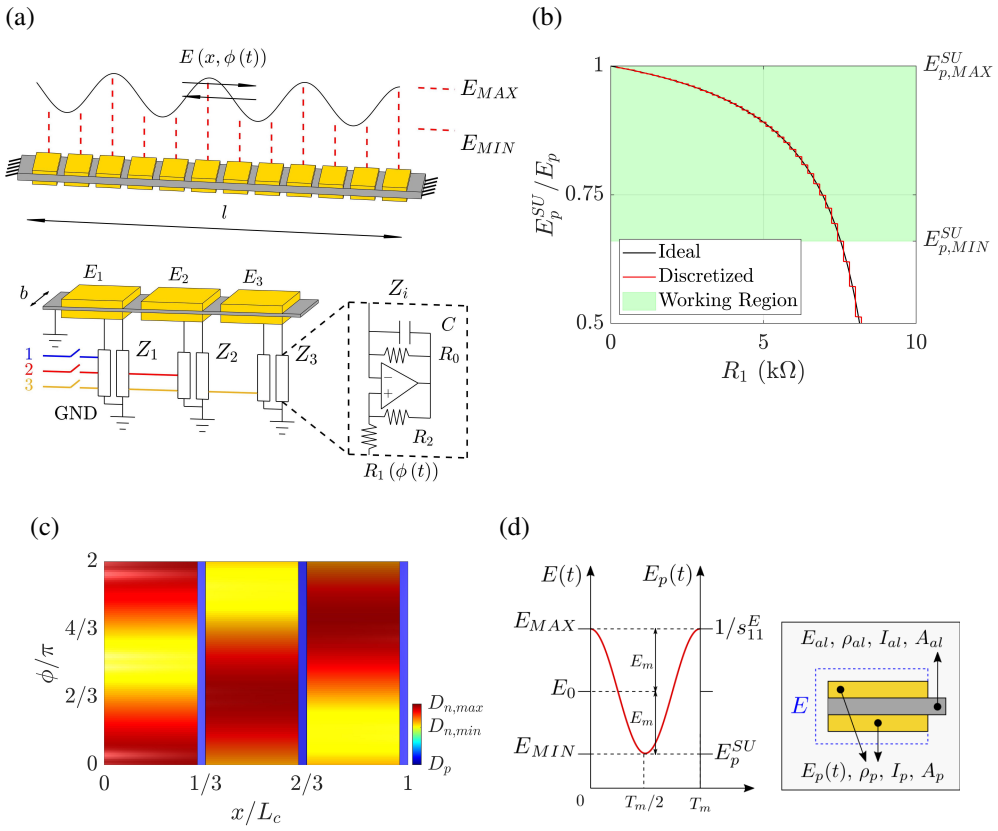

Figure 5.6: (a) Schematic of the experimental electromechanical system. Spatial-temporal modulation is provided through piezoelectric patches shunted to NC circuits. The stiffness value of each sub-element is suitably varied according to a projection from a sinusoidal function. The lower panel illustrates the unit cell and schematics of the NC shunts. Three consecutive NC circuits are controlled through phase shifted modulation signals 1,2, and 3, represented in blue, red and yellow, respectively. (b) Relationship between digital resistance R_1 of the circuit and shunted Young's modulus of the patch E_p^{SU}: ideal (black) and discretized (red) values, while the shaded green region represents the working region. (c) Representation of unit cell stiffness as a function of x and ϕ. (d) Schematic of the achieved temporal modulation on the layered structure and corresponding physical and geometrical parameters.

$m_p = \rho_{eq}\left(A_b + 2A_p\right) - m_b$ at the location of the patches.

A spatial and temporal modulation of the beam's stiffness is achieved by varying the effective Young's modulus of the sandwiched beam via controlling the resistor R_1 in each NC circuit. In particular, at the location of patch n, the Young's modulus is determined following the modulation presented Eq. 5.1, i.e., $E_n = E_0\left[1 + \alpha\cos\left(2\pi\theta n + \phi\right)\right]$. The parameters of the physical system allow for a modulation of amplitude $\alpha = E_m/E_0 =$

0.172, with $E_0 = (E_{MAX} + E_{MIN})/2 = 51.2$ GPa and $E_m = (E_{MAX} - E_{MIN})/2 = 8.8$ Gpa, while a choice of $\theta = 1/3$ implies in periodic unit with three patches (Fig. 5.6a). It is worth mentioning that the amount of stiffness modulation is limited by the stability of NC circuits. The resulting stiffness $D(x)$ is modulated according to Eq. 5.1, with $D_b = E_b I_b$ denoting the bending stiffness of the substrate, and $D_n = E_n (I_b + 2I_p) - D_b$ is the increase in stiffness at the location of the patches. Figure 5.6c displays the variation of the stiffness $D(x, \phi)$ in the unit cell within the domains $\phi \in [0, 2\pi]$ and $x \in [0, L_c]$, with constant stiffness D_p for the passive layers separating the patches (represented in blue). To achieve topological pumping, the phase ϕ is varied in time by temporal variations of the resistance R_1. Figure 5.6d conceptually illustrates the temporal variation of Young's modulus at the location of one of the patches, where the total period T_m determines the speed of phase variation, and can be tuned to induce temporal pumping with different speeds.

5.4.2 Experimental Results

To characterize the beam spectrum as a function of ϕ, the beam is actuated under a band-limited noise excitation in the 3-15 kHz frequency range at one end by one of the patches next to the clamp. The signal is continuously applied for the duration of the test ($T = 2.2$ s), while the phase ϕ varies in the interval $[0, 2\pi]$. The experiment is designed to reproduce the steady-state behavior of the beam under a quasi-static variation of ϕ, which allows for the characterization of the spectral dependence with ϕ in a single experiment. The resulting input and output signals are post-processed to estimate the frequency response of the beam as a function of the phase ϕ. To this end, the signals are multiplied by a rectangular window of length $T_s = 0.22$ s, centered at an instant t_0, and the frequency response of the beam for $\phi = \phi(t_0)$, i.e., $W(x, \phi(t_0), \omega)$, is obtained by employing an H1 frequency estimator [93]. The center of the window t_0 is smoothly translated in time, while the L_2 norm is taken along the spatial x coordinate. This produces estimations of the frequency response as a function of $\phi(t_0)$, i.e., $W(\phi, \omega)$, reported as contour plots in Figs. 5.7a and b, which correspond to

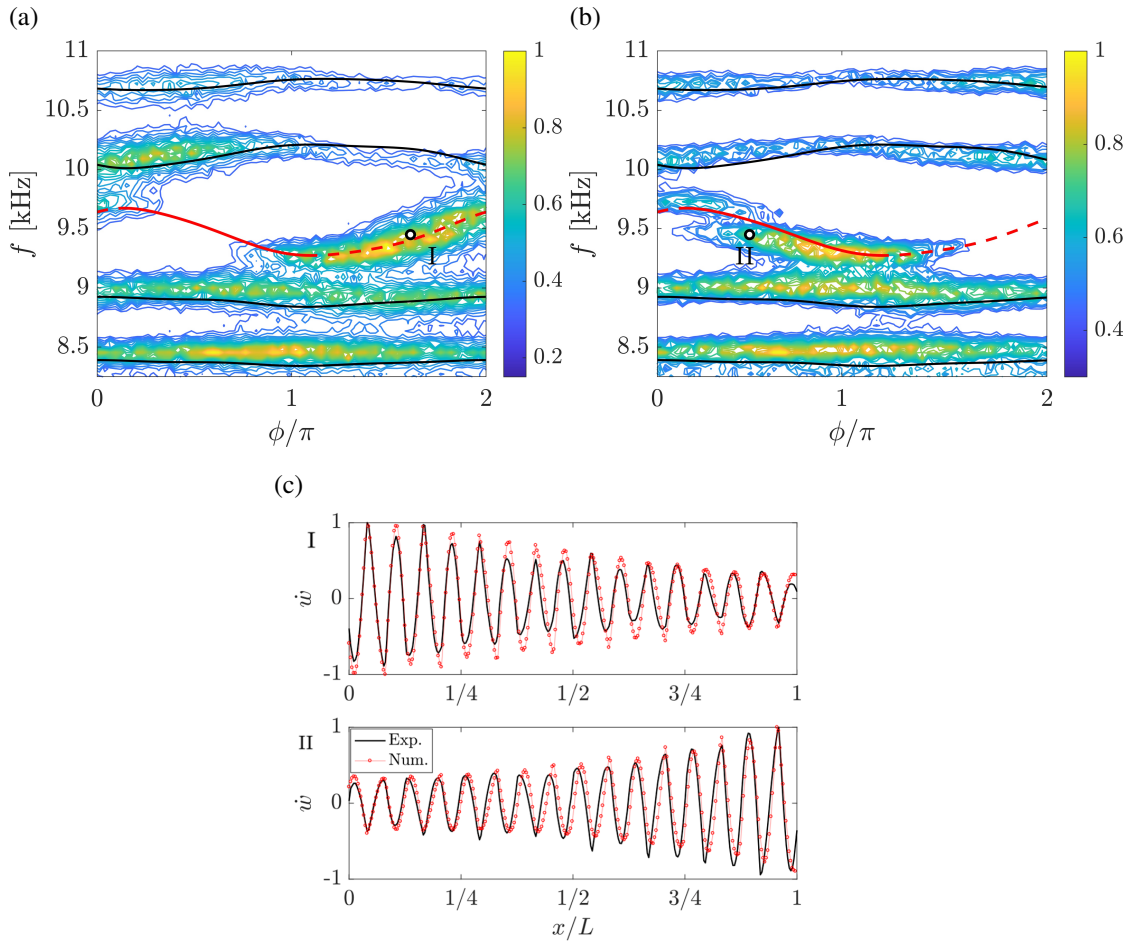

Figure 5.7: Experimental spectral characterization of modulated electromechanical beam. (a,b) Measured frequency response as a function of ϕ (contours) for excitation at the left (a) and right (b) boundary, superimposed to the eigenfrequencies of bulk (black) and edge (red) modes. The left excitation identifies mostly the left-localized portion of the branch of the edge state (dashed lines), while results the right excitation identifies the right-localized portion (solid line). (c) Representative experimental response for left (I) and right (II) localized modes, corresponding to points marked in (a) and (b), respectively. Black and red lines represent experimental and numerical data.

two experiments where the beam is excited at the left and right boundary, respectively.

Black and red lines superimposed to the experimental contours correspond to the eigenfrequencies of the bulk and edge modes predicted numerically. In the experiments, left excitation (Fig. 5.7a) reproduces mostly the left-localized branch of the edge state (dashed lines), while the right excitation experiment (Fig. 5.7b) captures primarily the right-localized branch (solid line). Experimentally measured left-localized and right-localized modes

corresponding to the points marked as 'I' and 'II' Figs. 5.7a,b are shown in Fig. 5.7c and compared to the numerical velocity profile. The experimental results show a good agreement with numerical spectrum, which is obtained according to the procedure described in Section 5.3.2 with modified boundary conditions to better match the practical boundaries. A linear $k_{w,l} = 2.5 \cdot 10^7$ N/m, $k_{w,r} = 1 \cdot 10^7$ N/m and rotational $k_{\theta,l} = 1 \cdot 10^3$N/rad, $k_{\theta,r} = 1 \cdot 10^5$N/rad springs are added to the boundaries. Additional passive regions of length $l_1 = 2$ mm and $l_2 = 1$ are respectively added to the left and right boundaries, since they are present in experiments to avoid undesired connections.

Upon characterization of the spectrum and corresponding edge states, a smooth temporal variation of ϕ is imposed to induce topological pumping. The left-localized mode defined for $\phi_1 = 1.6\pi$ (mode I in Figs. 5.7a,c) is targeted by applying a harmonic excitation of frequency 9.45kHz to the left boundary. The excitation signal is maintained for an interval of 12 ms, which is found sufficient to induce the steady-state motion of the left-localized mode and to avoid any contribution of neighboring bulk modes. After steady-state conditions are reached, the excitation is smoothly reduced to zero and the modulation phase is varied from $\phi_1 = 1.6\pi$ to $\phi_2 = 0.4\pi$ to induce edge-to-edge transitions. This modulation of the phase causes the transition to the right-localized mode (mode II in Figs. 5.7b,c).

For a better visualization of the transient response after the excitation signal goes to zero (after $t = 12$ ms), the experimental results are compensated for dissipation by applying the following procedure. First, the response of the un-modulated waveguide (with ϕ constant in time) displayed in Fig. 5.8a is used to estimate the damping coefficient of the edge state. The time history at any point along the beam exhibits an exponential decay envelope of the form $e^{-\zeta t}$, allowing for an estimation of $\zeta = 451.25$ s^{-1}. The transient time history is then multiplied by $e^{\zeta t}$ to approximate the response of the the system should dissipation be minimized, as illustrated in Fig. 5.8b.

The same procedure is then applied to the damped pump displayed in Fig. 5.9a, resulting from a phase modulation $\phi(t)$. Although energy is transferred from the left boundary

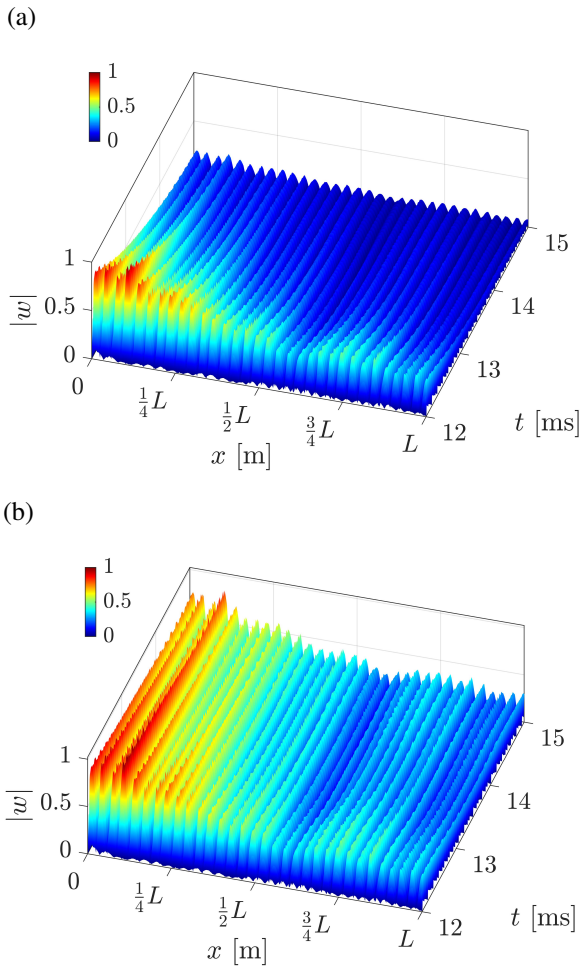

Figure 5.8: Velocity fields for ϕ constant in time. (a) Original results presenting dissipation. (b) Processed results for compensating dissipation obtained by multiplying the velocity field by $e^{\zeta t}$ in order to estimate the behavior of the system in minimal dissipation conditions.

to the right boundary, the dissipation of energy makes the visualization of the pump troublesome. By multiplying the time history by $e^{\zeta t}$ with the coefficient ζ previously obtained, a better visualization of the pump is obtained as displayed in Fig. 5.9b. Furthermore, the velocity field is normalized by the maximum velocity value measured at the beginning of the pumping process. The whole processing procedure does not alter the spatial distribution of the velocity field $\dot{w}$ at any given time instant, but allows for a better visualization of the pump and approximates the behavior of the system should dissipation be minimized. To be noticed, the physical mitigation of dissipation may play an important role in future studies aiming at exploring the full limits of topological pumping, both fast and slow, and

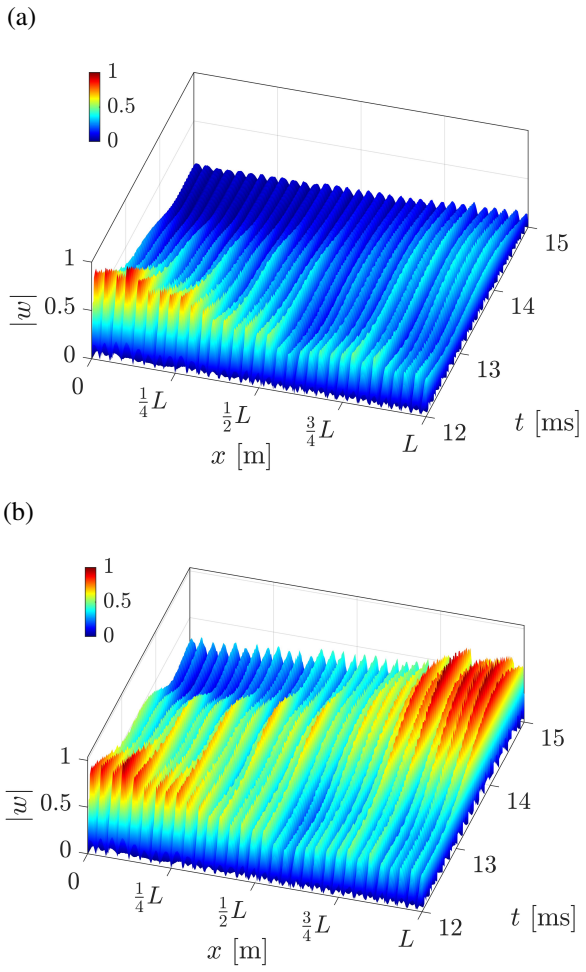

Figure 5.9: Velocity fields for ϕ modulated in time. (a) Original results presenting dissipation. (b) Processed results for compensating dissipation obtained by multiplying the velocity field by $e^{\zeta t}$ in order to estimate the behavior of the system in minimal dissipation conditions. Transient time history illustrates a transition from a left-localized mode to a right-localized mode, induced by a linear temporal phase variation from $\phi_1 = 1.6\pi \rightarrow \phi_2 = 0.4\pi$ starting at $t = 12$ ms, with a duration of 2 ms.

can potentially be achieved by introducing a negative loss factor through suitable active circuits [74].

To this end, Fig. 5.9b displays the magnitude of the experimentally recorded transverse motion of the beam from $t = 12$ ms onwards, i.e., after steady state conditions are reached. During the displayed time interval, the linear variation of the phase from $\phi_1 = 1.6\pi \rightarrow \phi_2 = 0.4\pi$ induces the expected transition from a left-localized edge state to a right-localized state. The topological pump displayed in Fig. 5.9b is characterized by

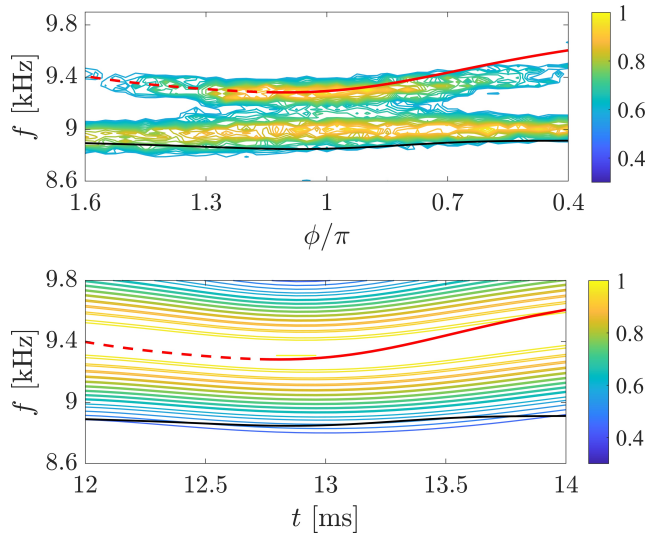

Figure 5.10: Spectral content of the broad-band excitation in quasi-static conditions (top) compared to spectrogram of the temporal pump (bottom), illustrating the adiabatic evolution along the branch of the edge state occurring in the pump with negligible influence of the neighboring bulk mode.

an adiabatic [79] transition along the branch of the edge state, as illustrated by the spectral content in Fig. 5.10. In the upper panel, the spectra in Figs. 5.7a,b are averaged to provide a single spectral characterization of the waveguide, and to highlight the presence of an edge state and of a bulk mode. In addition, a spectrogram is also computed for the transient topological pump to elucidate its adiabatic nature [70]. Since the transient pump occurs as a free response, no frequency response evaluations are required, making the computation of the spectrogram simpler when compared to the procedure described for the spectral characterization of the beam. In this case, the spectrogram is computed through a Fourier Transform (FT) of the windowed displacement time history $w\left(t_0, x, t\right) = G(t) w\left(x, t\right)$. Here, $G(t) = e^{-(t-t_0)^2/2c^2}$ represents a Gaussian function centered at $t = t_0$, where c is a parameter that controls the width of the function. Taking the Fourier Transform in time of $w\left(t_0, x, t\right)$ yields $w\left(t_0, x, \omega\right)$, which estimates the frequency content for the phase at the instant t_0, i.e., $\phi(t_0)$. The dependence on x is eliminated by taking the root-mean-square (RMS) value, while translating of the window center t_0 along the duration of the pump leads to the spectrogram $\left|w\left(\omega, \phi(t)\right)\right|$ displayed in the bottom panel Fig. 5.10. The results

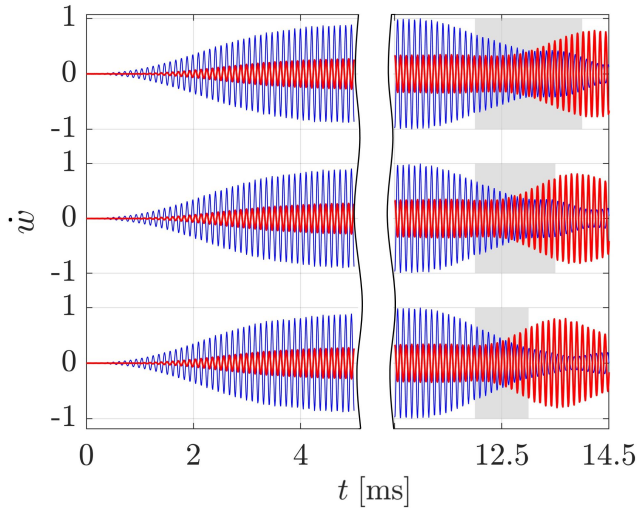

Figure 5.11: Signals at left (blue) and right (red) boundaries of the beam for temporal pumps induced within different modulation windows (shaded gray regions). In the initial 12 ms, steady state vibrations of the left-localized mode are induced (with duration halved for better visualization), while different phase modulation durations (top: 2 ms, middle: 1.5 ms and bottom: 1 ms) delay the arrival of the signal at the right end of the beam.

illustrate how energy remains concentrated around the edge state branch, with negligible contribution to the neighboring bulk modes (black line) as expected in an adiabatic state evolution [79].

Finally, it is experimentally shown that the temporal pump realized with controllable phase modulation speeds can be of potential interest for the manipulation and transport of information across the waveguide. Figure 5.11 displays the velocity time history for a point at the left (blue) and right boundary (red) of the beam. The three plots correspond to edge-to-edge transitions driven by different modulation speeds. Under the aforementioned testing conditions, the same input signal is employed, whereby during the first 12 ms a standing left-localized edge state is induced. At $t = 12$ ms, the linear temporal phase modulation $\phi(t)$ starts, ranging from $\phi_1 = 1.6\pi$ to $\phi_2 = 0.4\pi$ during an interval of 1 ms (bottom), 1.5 ms (middle) and 2 ms (top). The time duration of the phase modulation is highlighted by shaded gray areas to illustrate how the arrival time of the signal to the right end of the beam (in red) is controlled by the rate of phase modulation. This ability to control this arrival time independently from the underlying properties of the medium (the piezo

bimorph beam in this case) suggests opportunities for the designs of digitally controllable electromechanical delay lines based on topological pumping. While the employed experimental setup is subject to variability in its electrical and mechanical parts, the agreement between simulation and experimental results signal a reasonable degree of robustness to defects and imperfections.

5.5 Conclusions

This chapter investigates topological pumping in an electromechanical metastructure under stiffness modulation. For fixed parameter θ, the spatial stiffness modulation can produce non-trivial edge-localized states. A smooth temporal variation of the modulation phase ϕ drives the transfer of edge states from one boundary of the waveguide to the other in a controllable manner. This characteristic behavior for a topological pump of elastic waves is demonstrated for the first time in a continuous waveguide experimentally. Experiments are performed on a piezoelectric bimorph beam shunted to negative capacitance circuits with controllable modulation capabilities. Such modulations are employed for the topological pumping of edge states according to different modulation rates. This suggests the possibility to implement transfer of information in waveguides at speeds that are uniquely defined by the induced phase modulation, and independently of the physical parameters of the host structure. These results highlight potential applications to devices relying on robust signal transport, with tunable arrival times and phase delays, and open potential pathways for manipulating elastic waves using electromechanical waveguides.

CHAPTER 6
CONCLUSIONS, CONTRIBUTIONS AND FUTURE WORK

6.1 Summary and Conclusions

This dissertation investigates the dynamics and topology of both mechanical and electromechanical locally resonant metastructures leveraging nonlinearity and aperiodicity, as well as other interesting topological phenomena in electromechanical systems utilizing controllable shunt circuits. The study expands the concepts of linear and periodic metamaterials and metastructures, which have been widely studied, and demonstrates potentials of utilizing bistable attachments or quasiperiodic arrangement of the resonators to enhance vibration attenuation frequency bandwidth, control the vibration localization, and enable the transfer of the localized modes in finite structures.

6.1.1 Mechanical Locally Resonant Metastructures with Bistable Attachments

Based on a lumped parameter nonlinear model and a distributed parameter nonlinear model, dynamics of locally resonant metamaterial-based finite structures via bistable attachments is investigated numerically. It is demonstrated that amplitude-dependent bandwidth enhancement exists in this class of nonlinear metastructures, providing much wider attenuation bandwidth than the linear counterparts whose bandgap is known to be limited by the added mass ratio. Bistable attachments exhibit linear intrawell, nonlinear intrawell and nonlinear interwell oscillations under low, moderate and high intensity excitation, respectively. The overall nonlinear metastructure exhibits a linear locally resonant bandgap under low amplitude excitation and nonlinear attenuation due to wideband chaotic vibrations of the bistable attachments. Numerical predictions of the attachments' escape from the potential well by varying the forcing frequency and amplitude indicate that a threshold excitation

amplitude exists for all the attachments undergoing intrawell oscillations for all excitation frequencies. The design of the potential well of bistable attachments can be critical to fully utilize the interval oscillations of the attachments for wideband vibration attenuation.

Experimental validations are presented for a base-excited cantilever beam hosting seven bistable magnetoelastic beam attachments of the unit cells. The transition from linear locally resonant bandgap to nonlinear attenuation is observed, and the amplitude-dependent bandwidth enhancement is validated. The experimental results agree well with the numerical simulations obtained using the distributed parameter model.

6.1.2 Mechanical Locally Resonant Metastructures with Quasiperiodic Resonators

Both the dynamic behavior and dispersion topology of a family of mechanical locally resonant metamaterials and the resulting finite metastructures hosting quasiperiodic distributions of resonators are investigated. The topological properties of vibrational spectrum as a function of the quasiperiodic parameter θ, and their relation to the existence of localized modes are evaluated. The concept is employed in an elastic continuous system and demonstrated on a beam with an array of mechanical resonators.

First, the locations of the resonators are varied based on the quasiperiodic pattern generation procure. The bulk frequency spectrum as a function of θ exhibits a pattern that is reminiscent the Hofstadter butterfly. It is demonstrated that quasiperiodic placement of resonators introduces additional bandgaps that are topologically non-trivial and host protected, edge-localized modes in finite structures. Locally resonant bandgap remains unaltered for all θ values, however it is proved to be topologically trivial and does not hold topological edge-states. These additional bandgaps complement the well-known resonant gap, which is limited by the natural frequency of the resonators and added inertia. Experimental validations are performed on a cantilever beam hosting 30 resonators, and the observation of the additional bandgaps and edge-localized modes agrees well with the numerical predictions.

Secondly, the natural frequencies of the resonators are varied quasiperiodically. It is

shown that the bulk spectrum for metamaterials with resonators of quasiperiodic natural frequencies is similar to the one obtained for metamaterials with quasiperiodically located resonators when the modulation level is small. The locally resonant bandgap remains unaltered as θ varies, and separates two spectral regions with additional bandgaps whose center frequencies depend on θ. When the modulation level increases, the locally resonant bandgap becomes narrower or even closes for some θ values; and the bulk frequency spectrum becomes more fractal due to the overlapping of the additional bandgaps.

Further investigations illustrate interesting transitions of the localization from the boundary to the interior of the finite structure as a function of θ. And the localized mode at one boundary can be driven to the other boundary through phase modulation by introducing additional phase parameter in the quasiperiodic pattern generation.

6.1.3 Electromechanical Locally Resonant Metastructures with Quasiperiodic Inductive Shunt Circuits

Dynamics and topology of quasiperiodic electromechanical locally resonant metastructures are investigated on a piezoelectric bimorph beam in transverse motion with segmented electrodes connecting to quasiperiodic inductive shunt circuits. The bulk frequency spectrum as a function of quasiperiodic parameter θ defining the natural frequencies of the shunt circuits is fractal: additional topologically non-trivial bandgaps are created beside the typical electromechanical locally resonant bandgap. Spectra of bimorph beams made of different piezoelectric materials are compared and it is observed that the structure with smaller system-level electromechanical coupling exhibits more fractal spectrum under the same modulation level, even though all the generated bandgaps are smaller.

It is also observed numerically that some of the topological edge sates can evolve to interior-localized modes in the finite structure as θ varies, typically at θ values close to 0 or 1. In addition, by introducing phase modulation ϕ to the quasiperiodic arrangement, the localized mode at one boundary can be shifted to the other boundary through edge-bulk-

edge transitions for a given θ.

Finally, experimental validations are performed on a beam with 30 pairs of piezoceramic patches that are connect to digitally programmable synthetic impedance shunt circuits to provide the quasiperiodic inductance values. Topological bandgaps and associated edge-localized modes for several θ cases are observed and the results show good agreement with the numerical studies.

6.1.4 Temporal Topological Pumping in an Electromechanical Metastructure

Temporal pumping of elastic waves in an electromechanical waveguide with stiffness modulations is experimentally demonstrated on a piezoelectric bimorph beam with an array of piezoceramic patches shunted through negative capacitance circuits. Digitally controllable resistances in the negative capacitance shunt circuits enable the modulation on the Young's modulus of the beam. With a fixed θ value defining the periodicity or quasi-periodicity of the structure, topologically non-trivial edge states can be produced due to the spatial stiffness modulation. In the experiment, a smooth temporal variation of the modulation ϕ drives the transfer of edge states from the left boundary to the right boundary. It is observed that the phase modulation via negative capacitance circuits with controllable modulation capabilities can pump the edge states at different rates. This sheds light on the possibility of implementing transfer of information in waveguides at speeds that are uniquely defined by the induced phase modulation, and independently of the physical parameters of the host structure.

6.2 Contributions

The following summarizes the major contributions of this dissertation to the state-of-the-art:

- Demonstration of amplitude-dependent bandwidth enhancement in nonlinear locally resonant metastructures through a simplified lumped parameter nonlinear model of

mass-spring chain with bistable attachments (Chapter 2);

- Derivation of a distributed parameter nonlinear model for mechanical locally resonant metastructure with bistable attachment, which is applicable to predict the rich dynamics of the nonlinear metastructure (Chapter 2);

- Experimental validation of the predicted transition from linear locally resonant bandgap to nonlinear attenuation and the enhanced bandwidth on a cantilever beam with seven magnetoelastic bistable beam attachments (Chapter 2);

- Investigation of the effects of identical resonators that are located quasiperiodically on the metastructures and the estimation of the topological invariants characterizing non-trivial gaps and the onset of associated edge states (Chapter 3);

- Investigation of the effects of uniformly-placed mechanical resonators with varying natural frequencies based on the quasiperiodic pattern generation and the estimation of the topological invariants characterizing non-trivial gaps and the onset of associated edge states (Chapter 3);

- Experimental validation on the occurrence of additional topologically non-trivial bandgaps besides the locally resonant bandgap and edge-localized modes using an aluminum cantilever beam with an array of mechanical resonators (Chapter 3);

- Investigation of the dynamics of electromechanical locally resonant metastructures with quasiperiodic inductive shunt circuits and the topological properties of the additional bandgaps, together with the topologically protected edge states (Chapter 4);

- Experimental demonstration of the existence of additional topologically non-trivial bandgaps and edge-localized modes on a piezoelectric bimorph beam with digitally programmable synthetic impedance circuits (Chapter 4);

- Experimental demonstration of adiabatic temporal pumping of elastic waves for the first time in a continuous waveguide using a piezoelectric bimorph beam with digitally controllable negative capacitance circuits. (Chapter 5).

6.3 Future Work

The work on nonlinear locally resonant metastructures with bistable attachments has shown the wideband interval oscillations of the attachments for vibration attenuation. At the same time, the energy from the aperiodic/chaotic motions of the attachments are of interest to be harvested over a broad frequency range. Future work could consider adding piezoelectric energy harvesters to the mechanical bistable attachments to realize multi-functional metastructures.

In addition, the concept of nonlinear mechanical locally metastructures can be extended to nonlinear electromechanical locally resonant metastructures, leveraging piezoelectric unit cells with nonlinear circuits in the future work. The flexibility of the circuits can be used to realize adjustable potential wells of bistable attachments, which have been shown to be critical to fully utilize the interval oscillations of the attachments for wideband vibration attenuation.

The work on both the mechanical and electromechanical locally resonant metastructures with quasiperiodic resonators has shown the localization transition from the edge to the interior of the finite structure numerically. The localized mode travels with unaltered shape as a soliton-like transition. Future work can aim to observe such interesting phenomenon experimentally, which should be feasible on electromechanical metastructures with programmable synthetic impedance circuits. However, the existing experimental platform needs to be modified or improved to increase the electromechanical coupling, and to mitigate damping. For example, negative capacitance circuits with extra care to ensure the stability of the shunt circuits can be added to improve the electromechanical coupling.

The investigations on both bistable and quasiperiodic locally resonant metastructures

in this work so far have been limited to one-dimensional configurations (beams). Future work can aim to generalize those results to two-dimensional configurations (plates), which are more commonly used in real-life structures. Especially, the deterministic perturbations of periodic patterns of the resonators would be defined by the quasiperiodic projection from a sphere instead of a circle. Alternatively, the second dimension in the plate can be used as the additional synthetic dimension of a one-dimensional quasiperiodic system (i.e., quasiperiodic locally resonant beam) in the context of utilizing synthetic dimensions to explore higher dimensional topological effects in lower dimensional systems.

For ultra-wide vibration attenuation, a more complex locally resonant metastructure with bistable attachments that are arranged quasiperiodically can be considered in the future work. Though, besides improved distributed parameter nonlinear model, extensive parameter studies may be required for analyzing amplitude-dependent dynamics and topology of the structure.

REFERENCES

[1] M. M. Sigalas and E. N. Economou, "Elastic and acoustic wave band structure," *Journal of Sound Vibration*, vol. 158, pp. 377–382, 1992.

[2] M. S. Kushwaha, P. Halevi, L. Dobrzynski, and B. Djafari-Rouhani, "Acoustic band structure of periodic elastic composites," *Physical review letters*, vol. 71, no. 13, p. 2022, 1993.

[3] Z. Liu, X. Zhang, Y. Mao, Y. Zhu, Z. Yang, C. T. Chan, and P. Sheng, "Locally resonant sonic materials," *Science*, vol. 289, no. 5485, pp. 1734–1736, 2000.

[4] M. B. Assouar, M. Senesi, M. Oudich, M. Ruzzene, and Z. Hou, "Broadband plate-type acoustic metamaterial for low-frequency sound attenuation," *Applied Physics Letters*, vol. 101, no. 17, p. 173 505, 2012.

[5] C. Sugino, Y. Xia, S. Leadenham, M. Ruzzene, and A. Erturk, "A general theory for bandgap estimation in locally resonant metastructures," *Journal of Sound and Vibration*, vol. 406, pp. 104–123, 2017.

[6] D. Yu, Y. Liu, H. Zhao, G. Wang, and J. Qiu, "Flexural vibration band gaps in euler-bernoulli beams with locally resonant structures with two degrees of freedom," *Physical Review B*, vol. 73, no. 6, p. 064 301, 2006.

[7] H. Sun, X. Du, and P. F. Pai, "Theory of metamaterial beams for broadband vibration absorption," *Journal of Intelligent Material Systems and Structures*, vol. 21, no. 11, pp. 1085–1101, 2010.

[8] M. Oudich, M. Senesi, M. B. Assouar, M. Ruzenne, J.-H. Sun, B. Vincent, Z. Hou, and T.-T. Wu, "Experimental evidence of locally resonant sonic band gap in two-dimensional phononic stubbed plates," *Physical Review B*, vol. 84, no. 16, p. 165 136, 2011.

[9] R Zhu, X. Liu, G. Hu, C. Sun, and G. Huang, "A chiral elastic metamaterial beam for broadband vibration suppression," *Journal of Sound and Vibration*, vol. 333, no. 10, pp. 2759–2773, 2014.

[10] C. Sugino, S. Leadenham, M. Ruzzene, and A. Erturk, "On the mechanism of bandgap formation in locally resonant finite elastic metamaterials," *Journal of Applied Physics*, vol. 120, no. 13, p. 134 501, 2016.

[11] H Al Ba'ba'a, M Nouh, and T Singh, "Formation of local resonance band gaps in finite acoustic metamaterials: A closed-form transfer function model," *Journal of Sound and Vibration*, vol. 410, pp. 429–446, 2017.

[12] F Casadei, M Ruzzene, L. Dozio, and K. Cunefare, "Broadband vibration control through periodic arrays of resonant shunts: Experimental investigation on plates," *Smart materials and structures*, vol. 19, no. 1, p. 015 002, 2009.

[13] G. Wang, S. Chen, and J. Wen, "Low-frequency locally resonant band gaps induced by arrays of resonant shunts with antoniou's circuit: Experimental investigation on beams," *Smart Materials and Structures*, vol. 20, no. 1, p. 015 026, 2010.

[14] L. Airoldi and M. Ruzzene, "Design of tunable acoustic metamaterials through periodic arrays of resonant shunted piezos," *New Journal of Physics*, vol. 13, no. 11, p. 113 010, 2011.

[15] M Senesi and M Ruzzene, "Piezoelectric superlattices as multi-field internally resonating metamaterials," *AIP Advances*, vol. 1, no. 4, p. 041 504, 2011.

[16] Y. Jin, B. Bonello, and Y. Pan, "Acoustic metamaterials with piezoelectric resonant structures," *Journal of Physics D: Applied Physics*, vol. 47, no. 24, p. 245 301, 2014.

[17] A. E. Bergamini, M. Zündel, E. A. Flores Parra, T. Delpero, M. Ruzzene, and P. Ermanni, "Hybrid dispersive media with controllable wave propagation: A new take on smart materials," *Journal of Applied Physics*, vol. 118, no. 15, p. 154 310, 2015.

[18] C Sugino, S Leadenham, M Ruzzene, and A Erturk, "An investigation of electroelastic bandgap formation in locally resonant piezoelectric metastructures," *Smart Materials and Structures*, vol. 26, no. 5, p. 055 029, 2017.

[19] C. Sugino, M. Ruzzene, and A. Erturk, "Digitally programmable resonant elastic metamaterials," *Physical Review Applied*, vol. 13, no. 6, p. 061 001, 2020.

[20] M. F. Daqaq, R. Masana, A. Erturk, and D. D. Quinn, "On the role of nonlinearities in vibratory energy harvesting: A critical review and discussion," *Applied Mechanics Reviews*, vol. 66, no. 4, p. 040 801, 2014.

[21] A. Erturk, J Hoffmann, and D. Inman, "A piezomagnetoelastic structure for broadband vibration energy harvesting," *Applied Physics Letters*, vol. 94, no. 25, p. 254 102, 2009.

[22] F. Cottone, H. Vocca, and L Gammaitoni, "Nonlinear energy harvesting," *Physical Review Letters*, vol. 102, no. 8, p. 080 601, 2009.

[23] S. C. Stanton, C. C. McGehee, and B. P. Mann, "Nonlinear dynamics for broadband energy harvesting: Investigation of a bistable piezoelectric inertial generator," *Physica D: Nonlinear Phenomena*, vol. 239, no. 10, pp. 640–653, 2010.

[24] R. L. Harne and K. Wang, "A review of the recent research on vibration energy harvesting via bistable systems," *Smart materials and structures*, vol. 22, no. 2, p. 023 001, 2013.

[25] A. Arrieta, P Hagedorn, A. Erturk, and D. Inman, "A piezoelectric bistable plate for nonlinear broadband energy harvesting," *Applied Physics Letters*, vol. 97, no. 10, p. 104 102, 2010.

[26] O. V. Gendelman, "Bifurcations of nonlinear normal modes of linear oscillator with strongly nonlinear damped attachment," *Nonlinear Dynamics*, vol. 37, no. 2, pp. 115–128, 2004.

[27] Y Starosvetsky and O. Gendelman, "Vibration absorption in systems with a nonlinear energy sink: Nonlinear damping," *Journal of Sound and Vibration*, vol. 324, no. 3-5, pp. 916–939, 2009.

[28] ——, "Attractors of harmonically forced linear oscillator with attached nonlinear energy sink. ii: Optimization of a nonlinear vibration absorber," *Nonlinear Dynamics*, vol. 51, no. 1-2, p. 47, 2008.

[29] M. Parseh, M. Dardel, and M. H. Ghasemi, "Performance comparison of nonlinear energy sink and linear tuned mass damper in steady-state dynamics of a linear beam," *Nonlinear Dynamics*, vol. 81, no. 4, pp. 1981–2002, 2015.

[30] M Kani, S. Khadem, M. Pashaei, and M Dardel, "Vibration control of a nonlinear beam with a nonlinear energy sink," *Nonlinear Dynamics*, vol. 83, no. 1-2, pp. 1–22, 2016.

[31] T. M. Silva, M. A. Clementino, C. De Marqui Jr, and A. Erturk, "An experimentally validated piezoelectric nonlinear energy sink for wideband vibration attenuation," *Journal of Sound and Vibration*, vol. 437, pp. 68–78, 2018.

[32] K. Yang, R. Harne, K. Wang, and H. Huang, "Investigation of a bistable dual-stage vibration isolator under harmonic excitation," *Smart Materials and Structures*, vol. 23, no. 4, p. 045 033, 2014.

[33] L. Manevitch, G Sigalov, F Romeo, L. Bergman, and A Vakakis, "Dynamics of a linear oscillator coupled to a bistable light attachment: Analytical study," *Journal of Applied Mechanics*, vol. 81, no. 4, p. 041 011, 2014.

[34] F. Romeo, G. Sigalov, L. A. Bergman, and A. F. Vakakis, "Dynamics of a linear oscillator coupled to a bistable light attachment: Numerical study," *Journal of Computational and Nonlinear Dynamics*, vol. 10, no. 1, p. 011 007, 2015.

[35] D. R. Johnson, R. Harne, and K. Wang, "A disturbance cancellation perspective on vibration control using a bistable snap-through attachment," *Journal of Vibration and Acoustics*, vol. 136, no. 3, p. 031 006, 2014.

[36] A. Banerjee, R. Das, and E. P. Calius, "Waves in structured mediums or metamaterials: A review," *Archives of Computational Methods in Engineering*, vol. 26, no. 4, pp. 1029–1058, 2019.

[37] B. S. Lazarov and J. S. Jensen, "Low-frequency band gaps in chains with attached non-linear oscillators," *International Journal of Non-Linear Mechanics*, vol. 42, no. 10, pp. 1186–1193, 2007.

[38] A. Banerjee, E. P. Calius, and R. Das, "The effects of cubic stiffness nonlinearity on the attenuation bandwidth of 1d elasto-dynamic metamaterials," in *ASME 2016 International Mechanical Engineering Congress and Exposition*, American Society of Mechanical Engineers Digital Collection, 2016.

[39] A. Casalotti, S. El-Borgi, and W. Lacarbonara, "Metamaterial beam with embedded nonlinear vibration absorbers," *International Journal of Non-Linear Mechanics*, vol. 98, pp. 32–42, 2018.

[40] N. Nadkarni, C. Daraio, and D. M. Kochmann, "Dynamics of periodic mechanical structures containing bistable elastic elements: From elastic to solitary wave propagation," *Physical Review E*, vol. 90, no. 2, p. 023 204, 2014.

[41] N. Nadkarni, A. F. Arrieta, C. Chong, D. M. Kochmann, and C. Daraio, "Unidirectional transition waves in bistable lattices," *Physical Review Letters*, vol. 116, no. 24, p. 244 501, 2016.

[42] M. Hwang and A. F. Arrieta, "Solitary waves in bistable lattices with stiffness grading: Augmenting propagation control," *Physical Review E*, vol. 98, no. 4, p. 042 205, 2018.

[43] D. Cardella, P. Celli, and S. Gonella, "Manipulating waves by distilling frequencies: A tunable shunt-enabled rainbow trap," *Smart Materials and Structures*, vol. 25, no. 8, p. 085 017, 2016.

[44] P. Celli, B. Yousefzadeh, C. Daraio, and S. Gonella, "Bandgap widening by disorder in rainbow metamaterials," *Applied Physics Letters*, vol. 114, no. 9, p. 091 903, 2019.

[45] C. Hodges, "Confinement of vibration by structural irregularity," *Journal of Sound and Vibration*, vol. 82, no. 3, pp. 411–424, 1982.

[46] C. Hodges and J. Woodhouse, "Vibration isolation from irregularity in a nearly periodic structure: Theory and measurements," *The Journal of the Acoustical Society of America*, vol. 74, no. 3, pp. 894–905, 1983.

[47] D. M. Photiadis and B. H. Houston, "Anderson localization of vibration on a framed cylindrical shell," *The Journal of the Acoustical Society of America*, vol. 106, no. 3, pp. 1377–1391, 1999.

[48] C. Pierre and E. Dowell, "Localization of vibrations by structural irregularity," *Journal of Sound and Vibration*, vol. 114, no. 3, pp. 549–564, 1987.

[49] M. Z. Hasan and C. L. Kane, "Colloquium: Topological insulators," *Reviews of modern physics*, vol. 82, no. 4, p. 3045, 2010.

[50] L. Lu, J. D. Joannopoulos, and M. Soljačić, "Topological photonics," *Nature photonics*, vol. 8, no. 11, p. 821, 2014.

[51] G. Ma, M. Xiao, and C. Chan, "Topological phases in acoustic and mechanical systems," *Nature Reviews Physics*, vol. 1, no. 4, pp. 281–294, 2019.

[52] Y. Kraus, Y Lahini, Z Ringel, M Verbin, and O Zilberberg, "Topological states and adiabatic pumping in quasicrystals," *Physical Review Letters*, vol. 109, no. 10, p. 106 402, 2012.

[53] Y. Kraus and O Zilberberg, "Quasiperiodicity and topology transcend dimensions," *Nature Physics*, vol. 12, no. 7, pp. 624–626, 2016.

[54] K. Madsen, E. Bergholtz, and P. Brouwer, "Topological equivalence of crystal and quasicrystal band structures," *Physical Review B*, vol. 88, no. 12, p. 125 118, 2013.

[55] T. Ozawa, H. M. Price, N. Goldman, O. Zilberberg, and I. Carusotto, "Synthetic dimensions in integrated photonics: From optical isolation to four-dimensional quantum hall physics," *Physical Review A*, vol. 93, no. 4, p. 043 827, 2016.

[56] D.-T. Tran, A. Dauphin, N. Goldman, and P. Gaspard, "Topological hofstadter insulators in a two-dimensional quasicrystal," *Physical Review B*, vol. 91, no. 8, p. 085 125, 2015.

[57] E. Prodan, "Virtual topological insulators with real quantized physics," *Physical Review B*, vol. 91, no. 24, p. 245 104, 2015.

[58] L. Morini and M. Gei, "Waves in one-dimensional quasicrystalline structures: Dynamical trace mapping, scaling and self-similarity of the spectrum," *Journal of the Mechanics and Physics of Solids*, vol. 119, pp. 83–103, 2018.

[59] M. Gei, "Wave propagation in quasiperiodic structures: Stop/pass band distribution and prestress effects," *International Journal of Solids and Structures*, vol. 47, no. 22-23, pp. 3067–3075, 2010.

[60] D. J. Apigo, K. Qian, C. Prodan, and E. Prodan, "Topological edge modes by smart patterning," *Physical Review Materials*, vol. 2, no. 12, p. 124 203, 2018.

[61] D. J. Apigo, W. Cheng, K. F. Dobiszewski, E. Prodan, and C. Prodan, "Observation of topological edge modes in a quasiperiodic acoustic waveguide," *Physical Review Letters*, vol. 122, no. 9, p. 095 501, 2019.

[62] X. Ni, K. Chen, M. Weiner, D. J. Apigo, C. Prodan, A. Alù, E. Prodan, and A. B. Khanikaev, "Observation of hofstadter butterfly and topological edge states in reconfigurable quasi-periodic acoustic crystals," *Communications Physics*, vol. 2, no. 1, p. 55, 2019.

[63] R. K. Pal, M. I. Rosa, and M. Ruzzene, "Topological bands and localized vibration modes in quasiperiodic beams," *arXiv preprint arXiv:1906.00151*, 2019.

[64] D. R. Hofstadter, "Energy levels and wave functions of bloch electrons in rational and irrational magnetic fields," *Physical Review B*, vol. 14, no. 6, p. 2239, 1976.

[65] X.-L. Qi, T. L. Hughes, and S.-C. Zhang, "Topological field theory of time-reversal invariant insulators," *Physical Review B*, vol. 78, no. 19, p. 195 424, 2008.

[66] C. H. Lee, Y. Wang, Y. Chen, and X. Zhang, "Electromagnetic response of quantum hall systems in dimensions five and six and beyond," *Physical Review B*, vol. 98, no. 9, p. 094 434, 2018.

[67] M. Verbin, O. Zilberberg, Y. Lahini, Y. E. Kraus, and Y. Silberberg, "Topological pumping over a photonic fibonacci quasicrystal," *Physical Review B*, vol. 91, no. 6, p. 064 201, 2015.

[68] O. Zilberberg, S. Huang, J. Guglielmon, M. Wang, K. P. Chen, Y. E. Kraus, and M. C. Rechtsman, "Photonic topological boundary pumping as a probe of 4d quantum hall physics," *Nature*, vol. 553, no. 7686, p. 59, 2018.

[69] M. Lohse, C. Schweizer, H. M. Price, O. Zilberberg, and I. Bloch, "Exploring 4d quantum hall physics with a 2d topological charge pump," *Nature*, vol. 553, no. 7686, p. 55, 2018.

[70] M. I. Rosa, R. K. Pal, J. R. Arruda, and M. Ruzzene, "Edge states and topological pumping in spatially modulated elastic lattices," *Physical review letters*, vol. 123, no. 3, p. 034 301, 2019.

[71] E. Riva, M. I. Rosa, and M. Ruzzene, "Edge states and topological pumping in stiffness-modulated elastic plates," *Physical Review B*, vol. 101, no. 9, p. 094 307, 2020.

[72] S. Nakajima, T. Tomita, S. Taie, T. Ichinose, H. Ozawa, L. Wang, M. Troyer, and Y. Takahashi, "Topological thouless pumping of ultracold fermions," *Nature Physics*, vol. 12, no. 4, p. 296, 2016.

[73] M. Lohse, C. Schweizer, O. Zilberberg, M. Aidelsburger, and I. Bloch, "A thouless quantum pump with ultracold bosonic atoms in an optical superlattice," *Nature Physics*, vol. 12, no. 4, p. 350, 2016.

[74] I. H. Grinberg, M. Lin, C. Harris, W. A. Benalcazar, C. W. Peterson, T. L. Hughes, and G. Bahl, "Robust temporal pumping in a magneto-mechanical topological insulator," *Nature communications*, vol. 11, no. 1, pp. 1–9, 2020.

[75] H Chen, L. Yao, H Nassar, and G. Huang, "Mechanical quantum hall effect in time-modulated elastic materials," *Physical Review Applied*, vol. 11, no. 4, p. 044 029, 2019.

[76] I Brouzos, I Kiorpelidis, F. Diakonos, and G Theocharis, "Non-adiabatic time-optimal edge mode transfer on mechanical topological chain," *arXiv preprint arXiv: 1911.03375*, 2019.

[77] S. Longhi, "Topological pumping of edge states via adiabatic passage," *Physical Review B*, vol. 99, no. 15, p. 155 150, 2019.

[78] E. Riva, V. Casieri, F. Resta, and F. Braghin, "Adiabatic pumping via avoided crossings in stiffness modulated quasiperiodic beams," *arXiv preprint arXiv:2003.11525*, 2020.

[79] H Nassar, H Chen, A. Norris, and G. Huang, "Quantization of band tilting in modulated phononic crystals," *Physical Review B*, vol. 97, no. 1, p. 014 305, 2018.

[80] S. C. Stanton, B. A. Owens, and B. P. Mann, "Harmonic balance analysis of the bistable piezoelectric inertial generator," *Journal of Sound and Vibration*, vol. 331, no. 15, pp. 3617–3627, 2012.

[81] S Leadenham and A Erturk, "Nonlinear m-shaped broadband piezoelectric energy harvester for very low base accelerations: Primary and secondary resonances," *Smart Materials and Structures*, vol. 24, no. 5, p. 055 021, 2015.

[82] L. N. Virgin, R. H. Plaut, and C.-C. Cheng, "Prediction of escape from a potential well under harmonic excitation," *International Journal of Non-linear Mechanics*, vol. 27, no. 3, pp. 357–365, 1992.

[83] Q. He and M. F. Daqaq, "Influence of potential function asymmetries on the performance of nonlinear energy harvesters under white noise," *Journal of Sound and Vibration*, vol. 333, no. 15, pp. 3479–3489, 2014.

[84] W. Wang, J. Cao, C. R. Bowen, D. J. Inman, and J. Lin, "Performance enhancement of nonlinear asymmetric bistable energy harvesting from harmonic, random and human motion excitations," *Applied Physics Letters*, vol. 112, no. 21, p. 213 903, 2018.

[85] T. Dauxois and M. Peyrard, *Physics of solitons*. Cambridge University Press, 2006.

[86] A. Fleming, S Behrens, and S. Moheimani, "Synthetic impedance for implementation of piezoelectric shunt-damping circuits," *Electronics Letters*, vol. 36, no. 18, pp. 1525–1526, 2000.

[87] J Nečásek, J Vaclavik, and P Marton, "Digital synthetic impedance for application in vibration damping," *Review of Scientific Instruments*, vol. 87, no. 2, p. 024 704, 2016.

[88] J. Marconi, E. Riva, M. Di Ronco, G. Cazzulani, F. Braghin, and M. Ruzzene, "Experimental observation of nonreciprocal band gaps in a space-time-modulated beam using a shunted piezoelectric array," *Physical Review Applied*, vol. 13, no. 3, p. 031 001, 2020.

[89] K. F. Graff, *Wave motion in elastic solids*. Courier Corporation, 2012.

[90] M. I. Hussein, M. J. Leamy, and M. Ruzzene, "Dynamics of phononic materials and structures: Historical origins, recent progress, and future outlook," *Applied Mechanics Reviews*, vol. 66, no. 4, 2014.

[91] Y. Hatsugai, "Chern number and edge states in the integer quantum hall effect," *Physical review letters*, vol. 71, no. 22, p. 3697, 1993.

[92] T. Fukui, Y. Hatsugai, and H. Suzuki, "Chern numbers in discretized brillouin zone: Efficient method of computing (spin) hall conductances," *Journal of the Physical Society of Japan*, vol. 74, no. 6, pp. 1674–1677, 2005.

[93] K. Worden, *Nonlinearity in structural dynamics: detection, identification and modelling*. CRC Press, 2019.